Experimental Investigation of the Reflection of Thermal Sodium Atoms from a Moving Evanescent Grating

by

Bruce Stenlake

A thesis submitted for the degree of Doctor of Philosophy of the Australian National University

March 1997

Statement of Authorship

The contents of this thesis, except where indicated by references, are entirely my own work.

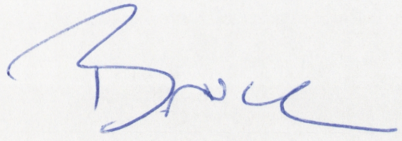

Bruce Stenlake

March 1997

Dedication

I dedicate this thesis to my mother and my father. They made me who I am , and have supported and encouraged me in every endeavour. This thesis would never have been completed without them.

Thank you for your love and guidance. I love you.

Abstract

This thesis reports an investigation of the interaction of a thermal sodium beam with a variety of near-resonant evanescent field configurations which was performed between March 1990 and September 1993. The evanescent fields were tuned above the sodium D2 transition, in order to repel atoms at glancing incident angles through the gradient force. Three evanescent field configurations, corresponding to various optic elements, were employed.

The first configuration was a travelling evanescent field, from which reflection of the beam was observed at glancing angles up to 4.5mrad. This configuration corresponds to a mirror for atoms.

The second configuration was a standing evanescent wave generated by retroreflecting the travelling evanescent wave. The resulting evanescent wave consisted of closely spaced reflective regions separated by non-reflecting nodes of the standing wave. This configuration corresponds to a mirror grating with periodicity $\lambda/2$. The atomic beam was reflected from the evanescent field. No diffraction was observed, however.

The final configuration was a moving standing evanescent grating, generated by interference between two counterpropagating laser beams. The relative velocity between the atoms and the grating could be continuously varied by adjusting the frequency of one laser. Coherent exchange of photons between the two fields in the moving evanescent grating was observed. This exchange exhibited velocity dependent resonant behaviour corresponding to doppleron resonances. The results are explained in terms of a dressed-state model for diffraction of atoms from such a grating. A parameter search was performed in an attempt to observe the diffraction of the thermal sodium beam, with null results. However, deflections which were dependent on grating velocity are reported.

Acknowledgements

This thesis is the culmination of a great deal of work and support from many people in my life. I would like to thank them here.

Thank you Nicole, Logan and Natasha for teaching me the meaning of love and happiness.

I would like to gratefully acknowledge the invaluable assistance of Brett Brown in the design and construction of much of the experimental apparatus.

Thanks also to many of the University technical support, especially Ian McRae, Craig McLeod and Mike Pennington.

For support during the last few years, I am indebted especially to Neil Manson and Peter Hannaford.

Finally, I would like to thank Ken Baldwin for his assistance with this thesis, and for not giving up on me.

Table of Contents

Chapter 1

Introduction

This chapter describes the purpose and scope of this thesis, and provides a brief background to the work.

1.1 Purpose

This thesis is written in partial fulfilment of the requirements of the PhD course at the Australian National University. It is intended to summarise the significant achievements made during the course and to present the original research performed.

1.2 Scope

This thesis is a summary of experimental research which was conducted between March 1990 and September 1993. It is limited to that work which is directly relevant to the major results described, and does not constitute an exhaustive list of research work performed.

The research resulted in two journal papers. The work presented in this thesis is summarised in Stenlake et al (1994). A description of some of the additional research work performed during the PhD course is contained in the paper by Li et al (1993). These papers are attached to this thesis in Appendix A.

This document assumes a knowledge of laser physics at graduate student level, and will avoid low level descriptions of basic concepts. It is intended as a guide through the concepts and decisions behind the work, and provides references to where rigorous developments may be found.

1.3 Overview

This document describes the development of a complex piece of experimental apparatus, the use of that apparatus in finding evidence supporting atomic diffraction theories, and a historical account of those theories.

Chapter 1 provides an introduction to this thesis. It summarises the purpose and scope of the document, provides an overview of the document and provides a background to the work.

Chapter 2 develops the theory of atomic diffraction from a conceptual viewpoint. The essential concepts are built one upon another to a level sufficient to allow an appreciation of this work.

Chapter 3 describes the experimental apparatus. The apparatus is divided into subsystems, with separate sections describing the atomic beam source, the atomic diffraction grating, the vacuum system, the optical system and the detection system. Within these sections, justifications for design decisions are provided, as well as recommendations for improving the system. Chapter 3 concludes with a list of procedures necessary for the operation of the apparatus.

Chapter 4 describes the results of the experiments performed, and highlights the significance of these results. The results reported include an analysis of the observed atomic reflection, an analysis of the interaction between the atomic beam and the moving diffraction grating and a complete parameter space search for diffracted atoms. A series of results demonstrating frequency dependent deflections of the atomic beam are also provided to highlight the possibilities for further work in this area.

Chapter 5 is a summary of the major achievements produced in this PhD project and their significance. In addition, the importance of the results of this project to future work in this field is described.

1.4 Background

The background to this work, culminating in the previous attempts to observe atom diffraction in this laboratory, is well summarised in Baldwin et al (1990).

The manipulation of atoms by lasers is a field which has expanded rapidly since the first atomic beam was focussed using laser light by Bjorkholm et al (1978). Much of the development in the field has been in laser cooling and trapping, including the cooling of helium atoms below the photon recoil limit (Aspect et al, 1988).

These techniques can produce atomic systems with very large de Broglie wavelengths which may be manipulated using conventional 'optical' devices made from matter. Such devices have been developed for atoms at thermal temperatures both for reflection (Anderson et al, 1986) and diffraction (Keith et al, 1988). These devices are very susceptible to surface contamination, and can only produce very small changes in the thermal atomic beam angles (some tens of microradians in the case of the transmission diffraction grating). Larger angles than this are required to produce a workable atomic beamsplitter with well separated beams. This is an essential component for practical matter interferometers.

Analogues of conventional optical devices have also been developed for neutral atomic beams using laser fields as the active element, completing the complementary picture of the dual wave/particle nature of light and matter. The same group that demonstrated the matter grating have also observed diffraction of a sodium beam at normal incidence to an optical standing wave *in vacuo*. Both Kapitza-Dirac (Gould et al, 1986) and Bragg (Martin et al, 1988) scattering have been demonstrated using tightly focused and

unfocused laser geometries, respectively. Again, the deflection angles for these systems are small (of the order of tens of microradians).

An alternative scheme using evanescent laser fields to produce neutral atomic beam optics was developed following a proposal by Cook and Hill (1982). A mirror for atoms was proposed using an evanescent light field to reflect an atomic beam, and was demonstrated for the first time by Balykin et al (1987,1988,1989,1989a). The evanescent field was generated using a c.w. dye laser , positively detuned in frequency from a sodium resonance line and totally internally reflected in a quartz block. The sodium beam was incident at grazing angle to the quartz/vacuum interface and was deflected by the evanescent field as a result of the gradient force. This scheme was also used to select atoms in a particular quantum state (Balykin et al, 1988), and has been proposed for the trapping of atoms in a cavity to produce atomic degeneracies comparable with the photon analogue in laser cavities (Balykin et al, 1989, 1989a).

The reflection of neutral atoms was also observed by Kasevich et al (1990) in an experiment where the atomic mirror was used as a trampoline for trapped atoms. Cooled atoms were suspended in an atom trap above an evanescent mirror. When the trap was turned off, the group of atoms fell under gravity, were reflected from the evanescent mirror, and were detected in the trapping laser beams when they had regained their former height.

At around this time, Hajnal and Opat (1989) proposed a combination of the concepts of the evanescent mirror for atoms and the diffraction grating, that is, an evanescent diffraction grating. By retroreflecting the laser beam which is used to generate the evanescent wave, a standing evanescent field is generated. This would produce a series of closely spaced atomic mirrors, separated by non-reflecting regions at the nodes of the standing wave. This is the optical analogy of the diffraction mirror grating.

In an attempt to observe diffraction from an evanescent grating, experiments were performed at the Australian National University (Hajnal et al, 1989; Baldwin et al,

1990). These experiments confirmed the results of Balykin (1988) in the observation of a reflected atomic beam from a travelling evanescent wave. In addition, the standing evanescent wave (evanescent grating) was shown to reflect sodium atoms for a greater range of laser frequencies. This behaviour was in qualitative agreement with theory.

Limitations in the original apparatus precluded observation of the predicted diffracted beams. It was recommended that improvements to both the sensitivity and the velocity resolution of the detection system be made in order to observe atomic diffraction. This thesis describes the project which followed.

During the course of this project, Deutschmann et al (1993) further developed the theory of atomic diffraction by presenting their quasipotential model. In their model, the transition from the incoming deBroglie wave to the diffracted waves takes place via the splitting and recombination of dressed state deBroglie waves at avoided crossings of quasipotentials. In essence, the quasipotential model is a description of the dynamical effects within the evanescent field which produce diffraction for a two-level atom. The quasipotential model is used extensively in this thesis to explain observed phenomena.

1.5 Aim

There were three aims of this project. The project followed the work by Hajnal et al (1989), which was a search for atomic diffraction. Initially, the aims of the project were:

- *to construct an improved experimental apparatus to enable diffraction to be measured from the evanescent grating*

- *to demonstrate diffraction of neutral sodium atoms from a standing evanescent field grating*

After the achievement of the first aim, experimental observations and conceptual breakthroughs led to the most significant aim of the project. This was

- *to investigate the interaction of neutral sodium atoms with a moving evanescent field grating*

In achieving this final aim, the significant contribution of this project was realised.

1.6 Advances

The project described in this document followed directly from the work of Hajnal et al (1989).

The detection apparatus was improved in the following ways. Atomic velocity resolution was improved from 25% to better than 2%. Detection sensitivity was improved by using multiple detection of single atoms. Angular resolution was improved from 1mrad to 0.16mrad.

In addition, the atomic beam source was completely redesigned and rebuilt to produce a reliable, constant flux of sodium atoms. The atomic beam source was contained in a separate vacuum chamber to reduce the volume of background sodium vapour in the detection region. These improvements are detailed in chapter 3.

An important conceptual advance was also introduced to the experiment during this project. The standing evanescent wave was generated using two lasers of differing frequency to produce a moving evanescent grating. This innovation allowed the evanescent grating to move at a velocity nearer to that of the atomic beam, thus reducing the Doppler shift due to the motion of the atoms. This increased the interaction strength between the atoms and the evanescent grating, enhancing the conditions required for diffraction. A new theory (Deutschmann et al, 1993) was adapted and used to explain the phenomena observed while investigating the moving

evanescent grating. Both the conceptual advance and the resulting explanations are presented in chapter 4 of this thesis.

Chapter 2

Theoretical Considerations

This chapter describes the concepts required for an understanding of the project. A historical introduction into the theory is developed, beginning with forces on atoms and concluding with the dressed state, quasipotential model. The project described in this thesis was primarily experimental. Consequently, a limited theoretical development will be presented in this chapter.

The discussion is divided into four sections. The first section discusses the forces which an atom may experience in a near-resonant light field. A more rigorous discussion for this background theory is presented by Cohen-Tannoudji (1991) and Adams et al (1994). The second section introduces the concept of the atomic mirror, first presented by Cook and Hill (1982). The use of a standing evanescent wave to generate a diffraction grating for atoms, proposed by Hajnal and Opat (1989), is discussed in the third section. To describe the processes occurring inside the standing evanescent wave, the quasipotential model developed by Deutschmann et al (1993) is reviewed in the final section.

2.1 Near-Resonant Light Forces on Atoms

This project utilises an evanescent wave to reflect neutral sodium atoms using the gradient force. There are a number of ways to derive this force, of which the simplest may be the semi-classical approach due to Dowling et al (1996) and Cook (1979).

Let the interaction potential term, V(**R**), between the electromagnetic field and the atom be, in the dipole approximation,

$$V(\mathbf{R}) = -\mathbf{d} \cdot \mathbf{E}(\mathbf{R}) \qquad (2.1)$$

where **R** is the position operator for the atomic centre of mass and **d** is the atomic dipole-moment operator. Ehrenfest's theorem allows one to write the expectation value of the force on the atom

$$\mathbf{F} = < \nabla (\mathbf{d} . \mathbf{E}) > \tag{2.2}$$

where the gradient operator is taken with respect to **R**. **d** does not depend on **R** since it is only a function of the atomic electron relative co-ordinate operator. Therefore, equation 2.2 may be rewritten as

$$\mathbf{F} = \left\langle (\mathbf{d}.\hat{\mathbf{e}}) \nabla \mathrm{E} \right\rangle \tag{2.3}$$

where $\hat{\mathbf{e}}$ is a unit polarisation vector (which is also assumed to be independent of **R**) and E is the field amplitude. Assuming that the dimensions of the atomic wave packet are small compared to the characteristic lengths over which E varies (such as the optical wavelength), equation 2.3 may be approximated by

$$\mathbf{F} = \left\langle \mathbf{d}.\hat{\mathbf{e}} \right\rangle \nabla \mathrm{E} \tag{2.4}$$

and R may be treated as a classical variable.

The expectation value appearing in equation 2.4 involves the atomic dipole **d** induced by the field, and as such depends on **R**. It can be calculated in a straightforward way from the optical Bloch equations under a number of assumptions. If only two levels, $|1\rangle$ and $|2\rangle$ are involved in the process, the matrix element $\langle 1|\mathbf{d} . \hat{\mathbf{e}}|2\rangle \equiv \mu$ may be taken to be real, and the expectation value

$$\left\langle \mathbf{d}.\hat{\mathbf{e}} \right\rangle = \mu (\rho_{12} + \rho_{21}) \tag{2.5}$$

where ρ_{12} and ρ_{21} are atomic density-matrix elements.

If $\omega_0 \equiv (E_2 - E_1)/\hbar$ is the natural frequency of the $|1\rangle \rightarrow |2\rangle$ transition, then in the absence of interaction, we have $\rho_{12} \alpha e^{i\omega_0 t}$ and $\rho_{21} \alpha e^{-i\omega_0 t}$. Similarly, assuming the field E(t,**R**) is monochromatic with frequency ω, it can be written as the sum of two rapidly varying complex exponentials,

$$\mathrm{E}(t,\mathbf{R}) = \frac{1}{2} \mathrm{E}(\mathbf{R}) \left\{ e^{-i\omega t + i\theta} + e^{i\omega t - i\theta} \right\} \tag{2.6}$$

where E(**R**) is the real amplitude and the phase factor θ may be a function of **R**. For example, for a standing wave θ=0, while for a running wave θ = **k** . **R** (where **k** is the wave vector of the electromagnetic field). The rotating wave approximation may be invoked when the $\omega - \omega_0 << \omega_0$. The rotating wave approximation neglects terms which correspond to two-photon transitions (that is, correspond to a transition to the upper state and photon emission, or else a transition to the lower state and absorption of a photon). Making the rotating wave approximation in equation 2.6 (by neglecting the terms which oscillate at or near twice the optical frequency) yields

$$\mathbf{F} = \frac{1}{2}\mu\rho_{12}\left(\nabla E + i E \nabla\theta\right)e^{-i\omega t + i\theta} + \text{c.c.} \qquad (2.7)$$

The optical Bloch equations for a two-level atom at the point R, with the interaction of equation 2.1 and the field of equation 2.6, may now be found. For an atom at rest, and in a time frame longer than $1/\gamma$ (where γ is the decay rate of the upper level), the following steady-state solution may be substituted into equation 2.7:

$$\rho_{12} = \frac{\Omega}{\gamma^2 + 4\Delta^2 + 2\Omega^2}\left(2\Delta + i\gamma\right)e^{i\omega t - i\theta} \qquad (2.8)$$

where $\Delta = \omega - \omega_0$ is the laser detuning, and $\Omega(\mathbf{R}) = \mu E(\mathbf{R}) / \hbar$ is the (position-dependent) on-resonance atomic Rabi frequency. Note that the unit for Δ here is s^{-1}, and in Chapters 3 and 4 the unit for detuning is $\Delta/2\pi$ in Hz.

Note that the inclusion of the Doppler effect due to a moving atom in the theoretical development would lead to a more complex picture (Adams et al, 1994). The inclusion of the Doppler effect at this stage is not necessary for development of the two forces discussed in this section, and may be included in the final stages of the derivation. Substituting equation 2.8 into equation 2.7 yields the force

$$\mathbf{F} = \frac{\hbar}{\gamma^2 + 4\Delta^2 + 2\Omega^2}\left\{-\Delta\nabla\Omega^2 + \gamma\Omega^2\nabla\theta\right\} \qquad (2.9)$$

Equation (2.9) is the addition of two terms. The first term in the expression is the dipole or gradient force, which acts in the direction of the gradient of the field intensity. That is, towards high intensity regions for negative (red) detunings and towards low intensity regions for positive (blue) detuning. The second term is the light pressure

force. For a travelling plane wave where $\theta = \mathbf{k} \cdot \mathbf{R}$, the force is in the direction of the wave vector **k**. In this context, it is also called the spontaneous force since it is proportional to the spontaneous emission rate γ (Gordon et al, 1980).

These two fundamental forces of the optical field on a neutral atom, the light pressure force and the gradient force, are depicted in figure 2.1 for a near-resonant, positively detuned, Gaussian laser beam. The following discussions of these two forces are intended to provide a conceptual understanding of the forces.

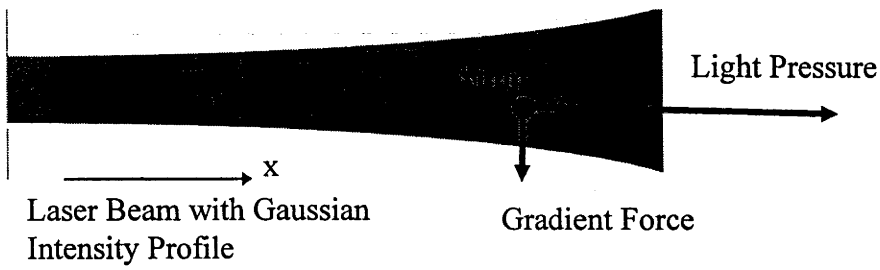

Figure 2.1 : A near resonant laser beam will impose two forces upon an atom. Photon pressure acts in the direction of the beam, and the gradient force will direct atoms to regions of high or low intensity.

2.1.1 Light Pressure Force

The most intuitive force upon the atom is that of light pressure. When the atom absorbs a photon, the process may be considered an inelastic collision in which the atom gains the momentum of the photon ($\hbar k$). The subsequent spontaneous emission of a photon will be in a random direction. After many absorptions and spontaneous emissions, the net momentum change due to absorptions is in the direction of the light beam, while the net momentum change due to spontaneous emissions is zero. The atom is 'pushed' by the 'pressure' of impacting photons. This process may only be regarded as a classical force in a time frame much longer than the excited state lifetime of the atom (Balykin and Letokhov, 1995).

The magnitude of the force is the product of the momentum of the photons, $\hbar k$, the linewidth of the upper state, γ, and the population of the excited state. The light pressure force is thus described (Balykin and Letokhov, 1995; Ashkin, 1970) by

$$\mathbf{F}_{lp} = (\hbar k).\gamma.\left(\frac{\Omega^2}{\gamma^2 + 4\Delta^2 + 2\Omega^2}\right) \tag{2.10}$$

where $\Delta = \omega - \omega_0 - kv_x$ is the effective laser detuning which is now Doppler shifted due to the atomic motion in the x direction. By making Ω very large in equation (2.10), it can be seen that as the laser intensity increases, the maximum possible force on an atom is

$$F_{lp,max} = \hbar k \gamma / 2 \tag{2.11}$$

The light pressure force therefore has two limitations. The direction of the force is always in the direction of the photons. Also, the magnitude of the light pressure force is limited by the spontaneous emission rate, γ, of the excited state.

2.1.2 Gradient Force

A potentially more powerful force which may be used to manipulate atoms is the so-called gradient force (sometimes called the dipole force). The gradient force may be described in a many ways (Adams et al, 1994; Balykin and Letokhov, 1995; Dalibard and Cohen-Tannoudji,1985).

From equation 2.9, the gradient force may be expressed for an atom moving in the x-direction as

$$F_{gr} = -\hbar \Delta \nabla \Omega^2 / (4 \Delta^2 + \gamma^2 + 2 \Omega^2) \tag{2.12}$$

where Ω is the on-resonance Rabi frequency of the light field and Δ is the Doppler shifted detuning.

Equivalently, the average gradient force is described (Adams et al, 1994; Cook and Hill, 1982) as the gradient of a pseudo-potential

$$F_{gr}(\mathbf{R}) = - \nabla U(\mathbf{R}) \tag{2.13}$$

where

$$U(\mathbf{R}) = \frac{\hbar\Delta}{2} \ln\left[1+\frac{2\Omega^2(\mathbf{R})}{4\Delta^2+\gamma^2}\right] \qquad (2.14)$$

Substituting equation 2.14 into 2.13 and solving yields the gradient force, described by equation 2.12.

The discussion here is limited to an interpretation of the dipole force similar to that given by Dalibard and Cohen-Tannoudji (1985). In the limit of very strong fields ($\Omega >> \gamma$) and large detunings ($\Delta >> \Omega,\gamma$), the gradient force equals the gradient of the dressed-state energies, weighted by the relative populations of the dressed states at a given point in the field. This model is particularly useful in visualising the quasipotential model (Deutschmann et al, 1993) in later sections.

The gradient force potential may be simplified using the above approximations to

$$U(\mathbf{R}) = \frac{\hbar\Delta}{2} \ln\left[1+\frac{2\Omega^2(\mathbf{R})}{4\Delta^2+\gamma^2}\right]$$

$$\cong \hbar\Delta \frac{\Omega^2(\mathbf{R})}{4\Delta^2+\gamma^2} \qquad \text{for } \Delta >> \Omega$$

$$\cong \frac{\hbar\Omega^2(\mathbf{R})}{4\Delta} \qquad \text{for } \Delta >> \gamma \qquad (2.15)$$

The following description is intended to provide a conceptual understanding of the gradient potential in the form used in equation 2.15.

The AC Stark Shift

Consider a situation where a two-level atom interacts with a laser tuned close to but above resonance. In this situation there is a ladder of dressed states of the system (Cohen-Tannoudji, 1977), separated into closely spaced pairs. A pair of dressed states, $|g,n\rangle$ and $|e,n-1\rangle$, in a field where n is the total photon number are depicted in figure 2.2.

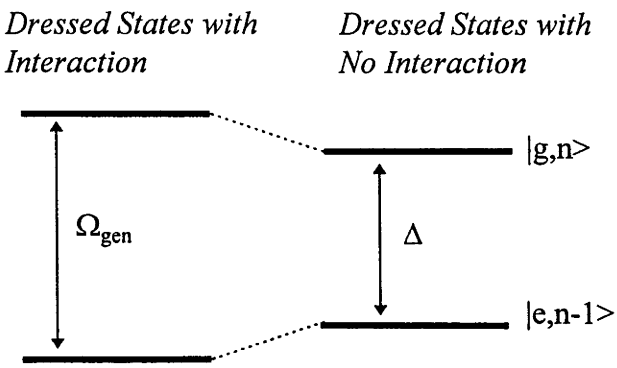

Figure 2.2 : The dressed state energy levels repel one another as the laser intensity increases. The shift in the ground state energy constitutes the potential which generates the gradient force.

Figure 2.2 presents two pairs of dressed states. The pair on the right, separated by an energy $\hbar\Delta$, are the dressed states in the limit of no interaction between the atom and the laser field (with detuning Δ). The pair of dressed states on the left of figure 2.2, separated by an energy $\hbar\Omega_{gen}$, are the dressed states appropriately shifted by an interaction with a laser field with a generalised Rabi frequency $\Omega_{gen} = [\Omega^2 + \Delta^2]^{1/2}$.

The dressed states without interaction are also referred to as asymptotic states, as they correspond to the interacting dressed states in the limit of low intensity. As the laser intensity increases, the coupling between the two states increases, and the dressed states with interaction become mixed, combining the character of the two asymptotic states |g,n> and |e,n-1>. For simplicity, the dressed states with interaction retain the label |g,n> or |e,n-1> of the asymptotic state to which they reduce in the limit of low laser intensity.

The separation between the interacting dressed states is equal to the generalised Rabi frequency, Ω_{gen}. When there is no interaction ($\Omega = 0$), $\Omega_{gen} = \Delta$, as shown in figure 2.2. As the laser intensity increases, the Ω_{gen} increases and the dressed states move apart. The states are said to repel one another as coupling increases.

This shift of the dressed state energy levels, E_S, is the AC Stark shift. The magnitude of the shift (Wei et al, 1995) is half the difference between the interacting dressed state separation and the asymptotic dressed state separation.

$$
\begin{aligned}
E_S / \hbar &= (\Omega_{gen} - \Delta)/2 \\
&= ([\Omega^2 + \Delta^2]^{1/2} - \Delta) /2 \\
&= (\Delta[1 + (\Omega^2 / \Delta^2)]^{1/2} - \Delta) /2 \\
&= ([1 + (\Omega^2 / \Delta^2)]^{1/2} - 1) \Delta/2 \\
&\cong ([1 + (\Omega^2 / 2\Delta^2)] - 1) \Delta/2 \qquad \text{for } \Delta >> \Omega \\
&= \Omega^2 / 4\Delta \qquad (2.16)
\end{aligned}
$$

Thus, as the coupling increases, the dressed states repel one another and shift in energy by $\Omega^2 / 4\Delta$. Comparison of this result with equation 2.15 demonstrates that, under these assumptions, the gradient force equals the gradient of the dressed-state energies.

The Gradient Force

The gradient force arises from the differences in the potential experienced by an atom in an inhomogeneous light field. It may be expressed as the gradient of the dressed state energies.

Suppose a group of atoms lies within a near-resonant light field whose intensity is spatially varying. Suppose further that this light field is strong ($\Omega >> \gamma$), monochromatic and is tuned sufficiently above resonance so that very few atoms are excited ($\Delta >> \Omega$). The gradient force is then the gradient of the 'ground state' ($|g,n>$) interacting dressed state energy described in figure 2.2.

For regions of higher light intensity, the coupling between the dressed states increases and they repel one another as in figure 2.2. The ground dressed-state energy therefore increases. The atom will therefore be repelled from regions of high intensity.

Similarly, regions of low field intensity lead to a reduced coupling of the dressed state energy levels. The $|g,n>$ potential will be at lower energy for low field regions, and the atoms will be attracted to these regions.

Note that if an atom makes a transition to the $|e,n-1>$ dressed state, then the atom will be attracted to the high intensity regions, since the $|e,n-1>$ dressed state is shifted to lower energy for increased coupling.

Note also that if the field were detuned below resonance, then the $|g,n>$ state would have lower energy than the $|e,n-1>$ state. In this case, the $|g,n>$ state would shift

towards lower energy for higher field strength, and the resultant gradient force would attract atoms in the |g,n> state to high field strength regions.

From equation 2.12, the gradient force is proportional to $\nabla \Omega^2$ (the gradient of the AC Stark shift). Ω is proportional to the electric field strength E, and the intensity of the optical field is proportional to E^2. Therefore, the gradient force is proportional to the gradient of the intensity of the optical field.

Another important aspect of the gradient force is that the direction of the force is dependent upon detuning Δ. If the detuning is reversed, then the direction of the gradient force is also reversed. Consequently, there is no gradient force experienced if the detuning is zero. From another viewpoint, for $\Omega >> \gamma$ and $\Delta=0$, the atom will be saturated, the population of upper and lower states will be equal and the average gradient force will be zero.

Finally, the gradient force is not limited by the excited state lifetime, and is only limited by the strength of the gradient of the field.

2.2 The Atomic Mirror

In 1982, Cook and Hill suggested that totally internally reflecting a near-resonant laser beam in a dielectric medium would generate an evanescent wave with a very steep intensity gradient for manipulation of atoms. If an evanescent wave was generated using a positively detuned plane wave, the resulting field would repel incident atoms. Cook and Hill (1982) stated that for typically achievable laser intensities (200mW at 589.0nm), sodium atoms with velocities up to 110 cm/s could be reflected.

The maximum reflected velocity is governed by the intensity of the evanescent field at the dielectric interface. The advantage of using an evanescent field is that the steep gradient produces a compact mirror.

By turning this field to grazing incidence with a thermal sodium beam (with atomic velocity of around $800ms^{-1}$), the atoms could be reflected by a few milliradians. Thus it was proposed that an atomic mirror could be constructed.

The evanescent wave described by Cook and Hill (1982) is generated by totally internally reflecting a plane electromagnetic wave of frequency ω in a medium of refractive index n. The evanescent wave travels in the +x direction and its field strength

is exponentially decaying in the y direction (the dielectric surface is perpendicular to the y direction). The electric field of the transmitted evanescent wave may be described by the equation

$$\mathbf{E}(\mathbf{x}, t) = \hat{\varepsilon}\, E \exp(-qy) \cos(\omega t - Qx) \tag{2.17}$$

where $\hat{\varepsilon}$ is the unit polarisation vector. E is the wave amplitude at y=0 (the dielectric interface) and is greater than the electric field in the laser, E_L, due to the enhancement of the electric field of the evanescent wave by the dielectric. Applying the Fresnel laws (Jackson, 1975) for transmission at the dielectric interface gives the expression (Kaiser et al, 1994)

$$E^2 = E_L^2 \left\{ \frac{4n^2 \cos^2\theta}{(n-1)^2 \left[(n^2+1)\sin^2\theta - 1 \right]} \right\} \tag{2.18}$$

where θ is the angle of incidence of the plane wave on the dielectric surface. The decay constant, q, of the evanescent wave is

$$q = \omega \left(n^2 \sin^2\theta - 1\right)^{1/2} / c \tag{2.19}$$

where c is the speed of light in vacuum. The wave vector of the evanescent wave, Q, is given by

$$Q = \omega\, n \sin\theta / c \tag{2.20}$$

The evanescent wave propagates parallel to the dieletric surface and is substantial only within a few wavelengths of the surface (from equation 2.17).

An atom in the evanescent wave will experience light forces from the field. There is a gradient force in the y direction, and a small light pressure force in the x direction. The light pressure force provides less than one photon momentum per atom for $\Delta >> \Omega$, a necessary experimental condition (see section 2.3.2 for details). If the evanescent field is tuned above resonance, $\Delta > 0$, where $\Delta = \omega - \omega_0 - kv_x$ is the Doppler shifted detuning, then the gradient force in the y direction will repel atoms from the dielectric surface, and may reflect atoms. The gradient force from equation 2.12 is approximated (Cook & Hill, 1982) by

$$F_{gr}(y) = 2\, q\, \hbar\, \Delta\, \Omega^2(y) / (4\,\Delta^2 + \gamma^2 + 2\,\Omega^2(y)) \qquad (2.21)$$

where $\Omega(y)$ is the on-resonance Rabi frequency of the evanescent field.

An atom of mass m initially moving toward the evanescent field with velocity v_y perpendicular to the dielectric interface has a kinetic energy, T_y, in the y direction, where

$$T_y = 0.5\, m\, v_y^2 \qquad (2.22)$$

The condition for reflection to occur, therefore, is that the perpendicular kinetic energy of the atom is less than the optical potential U(y) described in equation 2.14 at y=0. Thus, reflection occurs if

$$T_y < U(0) \qquad (2.23)$$

This gradient force potential for an atomic mirror is illustrated in figure 2.3. There are a number of features in the figure which should be noted.

First, there are two potentials illustrated as in figure 2.3. The incident atom will initially be in the |g,n> state, and its motion will be governed by that potential.

Second, note that the |e,n-1> potential is at lower energy than the |g,n> potential. This is due to the laser being detuned above resonance, so that each photon has more energy than the energy separation of the atomic states, as discussed in section 2.1. The energy separation between the two potentials in the far field is equal to $\hbar\Delta$.

Finally, note that if the atom does absorb a photon, the system will make a transition to the |e,n-1> state and the atom will be attracted to the dielectric surface. This was a primary loss mechanism in the experiment which was avoided by detuning sufficiently far from resonance to reduce the probability of absorption (and also reducing the magnitude of the light pressure force).

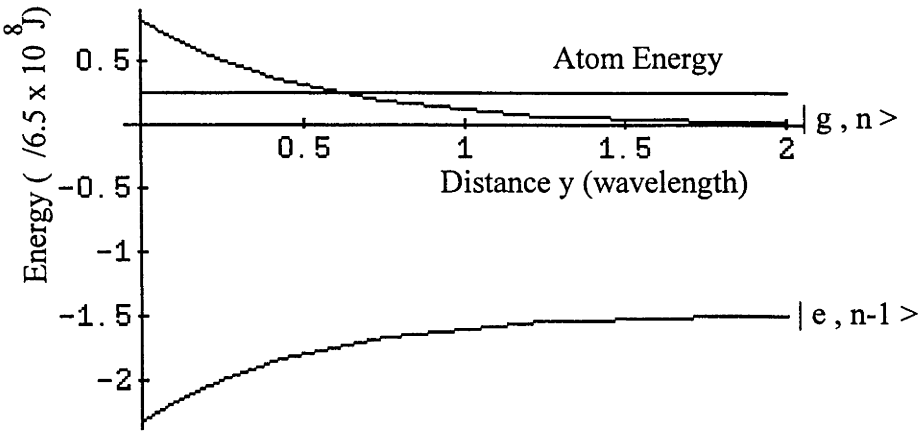

Figure 2.3: The intensity of the evanescent field diminishes exponentially with distance from the surface. The corresponding Stark shift also diminishes with distance from the surface. The dressed state |g,n> forms a repulsive potential hill from which the atom is reflected.

The data used to produce figure 2.3 was typical of the experimental conditions used for the reflection experiments (described in section 4.1). The kinetic energy of the atom in a direction normal to the dielectric surface, T_y, is shown in the figure and labelled Atom Energy. This energy corresponds to a thermal sodium atom ($900ms^{-1}$) incident upon the atomic mirror at a glancing angle of 2.7mrad. The refractive index of the quartz block dielectric was n=1.458, and the incidence angle of the laser was $\theta=45^{\circ}$. The detuning, Δ, was chosen to be 5GHz above resonance.

The evanescent field intensity was $240W/cm^2$. This intensity is normally expressed in terms of the saturation parameter $G = I / I_s$. The saturation parameter in the evanescent field was therefore $G = 3.8 \times 10^4$ for the sodium D2 transition ($I_S = 6.3mW/cm^2$). The saturation parameter may be expressed in terms of the on-resonance Rabi frequency and the transition linewidth by

$$G = 2\Omega^2 / \gamma^2 \qquad (2.24)$$

Using the saturation parameter, the gradient force may be re-expressed as the gradient of the pseudo-potential

$$U(\mathbf{R}) = \frac{\hbar\Delta}{2} \ln\left[1 + \frac{G(\mathbf{R})}{4\Delta^2/\gamma^2 + 1}\right] \qquad (2.25)$$

2.3 Reflection Simulations

With the aim of achieving the diffraction of sodium atoms, an experiment was planned. A number of preliminary calculations were performed to determine the most favourable parameter space for experimentation. The parameters investigated were laser intensity and frequency in order to determine the mirror reflectivity and the probability of photon absorption in the reflection process.

Mirror Reflectivity vs Laser Detuning

Various papers (Cook and Hill, 1982; Kasevich et al, 1990) quote the maximum possible velocity for atoms which allows reflection for a given evanescent field. An understanding of the response of this maximum reflected velocity to laser detuning was required. For this reason, calculations were performed to determine the maximum reflected velocity, v_y^{max}, as laser detuning, Δ, was varied. The calculations are based on the equation (Cook and Hill, 1982)

$$v_y^{max} = [\, (\hbar\Delta/m) \ln \{1 + (G(0)) / (4\Delta^2/\gamma^2 + 1)\} \,]^{1/2} \qquad (2.26)$$

where G(0) is the saturation parameter at the most intense region of the evanescent wave (at the dielectric interface). Equation 2.26 may be derived by substituting equations 2.22 and 2.25 into equation 2.23. The results were compared with values quoted by Cook and Hill (1982) and Kasevich et al (1990) to verify their validity.

The results of this calculation are shown in Figure 2.4. At low detunings ($\Delta \sim \gamma$), the response of v_y^{max} is dominated by the ($\hbar\Delta/m$) term in equation 2.26. In this case, the maximum reflected velocity decreases as the detuning is decreased. As discussed in section 2.1, the force is zero at $\Delta=0$. At high detuning ($\Delta >> \Omega,\gamma$), the response of v_y^{max} is dominated by the ln{..} term in equation 2.26. In this case, as Δ increases, the ln{..} term goes to zero. The maximum reflected velocity therefore decreases as the detuning is increased.

Between small and large detunings, v_y^{max} thus reaches a maximum. The value of the detuning at this maximum is determined by the competing terms in equation 2.26. Since the ln{..} term is dependent upon G, the peak of v_y^{max} is also dependent upon G, as shown in figure 2.4.

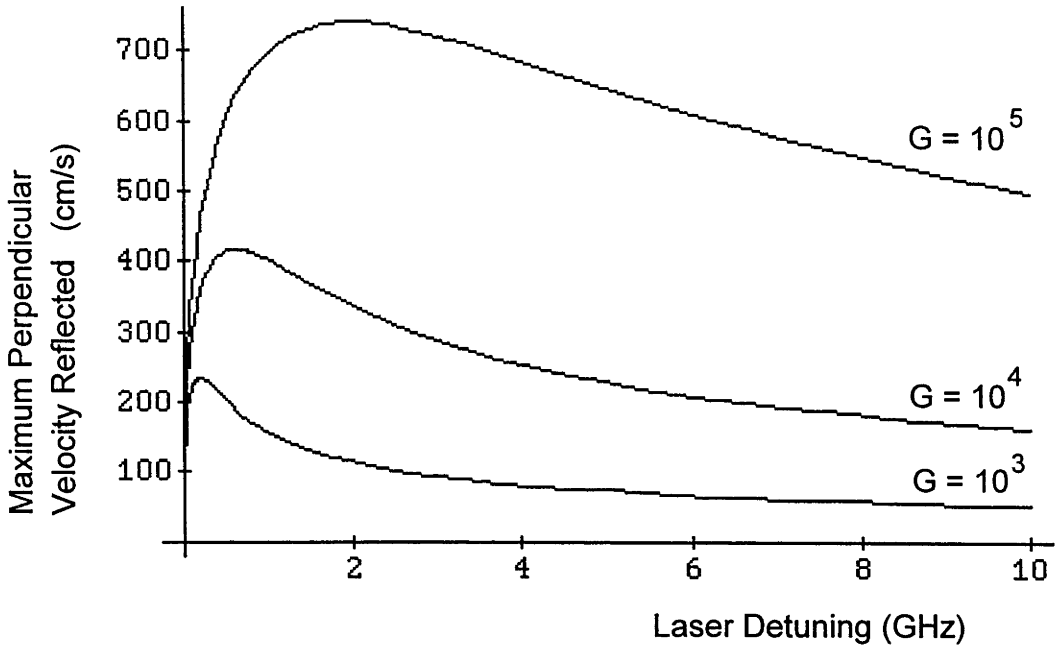

Figure 2.4 : The maximum normal velocity, v_y^{max}, of a sodium atom which may be reflected by an evanescent wave is dependent upon laser detuning, Δ, and saturation parameter, G, as shown.

The laser power which can be reliably reproduced in this laboratory, focussed down to a spot the size of our atomic mirror (350μm), gives a value of the saturation parameter for the sodium D2 line of around $G=3.8\times10^4$. Thus, we may expect to reflect atoms with a normal velocity of greater than 2.5 m/s over a large range of detunings (up to 10GHz).

Probability of Spontaneous Decay during Reflection

The coherence of the reflection process is of vital importance when it is extended to the diffraction grating case. In the first instance, it is important to determine the coherence of the reflection process.

During reflection, the atom will be in the |g,n> interacting dressed state. The |g,n> interacting dressed state is a mixture of the |g,n> and |e,n-1> asymptotic dressed states. There is therefore the possibility that the atom will undergo spontaneous emission during the reflection process. Spontaneous emission would destroy the coherence of the atom, making diffraction unachievable. Spontaneous emission events would also have disastrous consequences on the proposed applications of atom diffraction such as beam splitting for interferometry techniques.

It is therefore necessary to determine the likelihood of a coherent interaction between the atom and the atomic mirror. That is, it is necessary to predict the likelihood of spontaneous emission from the atom as it is reflected from the evanescent field.

Calculation of the number of spontaneous emissions expected during reflection, N, were performed using the analytical solution provided by Wallis (1993). The solution also appears Appendix B and in Savage (1995) and is

$$N = \gamma m v_y / \Delta \hbar q \qquad (2.27)$$

Note that N is independent of laser intensity, as the velocity v_y governs the maximum evanescent field intensity which the atom is energetically capable of achieving.

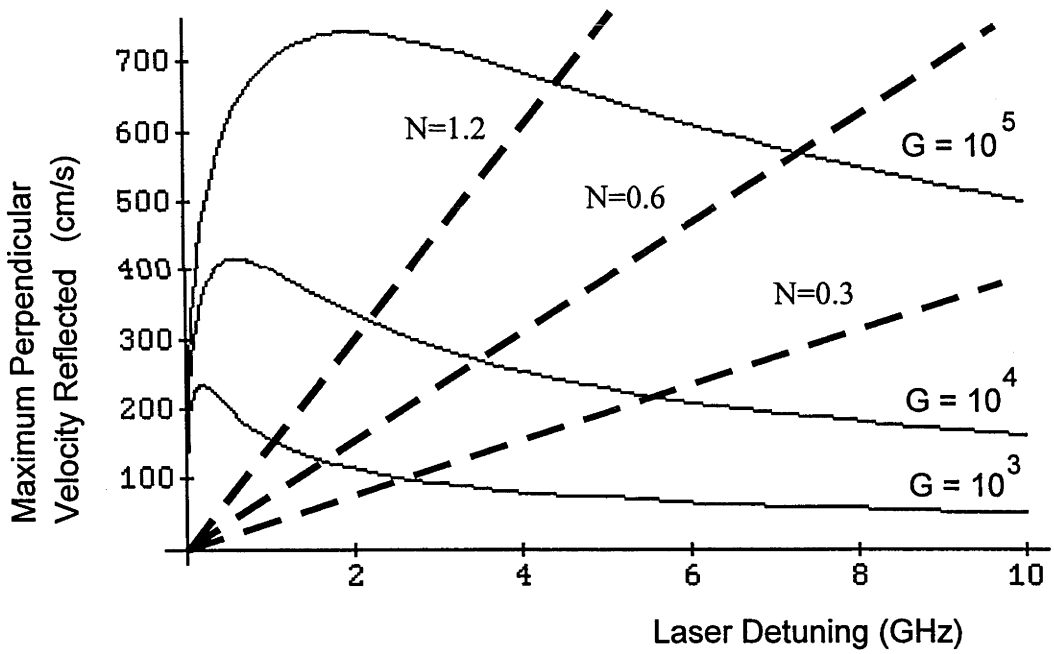

Figure 2.5 : (Dashed) Plot of probable number of spontaneous emissions, N, during reflection vs laser detuning, Δ, and incident atomic velocity, v_y^{max}. (Plain) As in figure 2.4, plot of maximum reflected velocity vs laser detuning as a function of saturation parameter (G).

The results of these calculations are illustrated in Figure 2.5. Note that the saturation parameters for maximum reflected velocity are identical to those in Figure 2.4. The dashed, bold lines are loci of points corresponding to the probable numbers of spontaneous emissions, N. The probable number of spontaneous emissions expected during reflection in the parameter regime of interest must ideally be less than one.

Figure 2.5 was used to determine the parameter regime in which any coherent process is likely to occur in an atomic mirror. There is a trade off between normal reflected velocity and coherence, and it was found that a viable regime exists in which experiments could be performed. A loss of 30% of atoms to spontaneous emission was considered acceptable, and the maximum reliable laser intensity achievable in the laboratory corresponded to $G=3.8\times10^4$ (see chapter 3 for derivation). The viable regime corresponds to a normal velocity of around 2 m/s and a laser detuning of 6GHz. These guidelines were used to determine the parameter space used in the initial experiments.

Note that while searching for diffraction, the configuration was not only an atomic mirror, but a standing, evanescent wave. The interaction between the two travelling waves and the moving atom led to a more complicated model, and made prediction of the probability of spontaneous emission events more difficult. Deutschmann et al (1993) later produced a model which stated that for diffraction to occur, the atom must spend a significant time in an 'excited' state. That model is described in section 2.5.

2.4 Atom Diffraction

In 1989, Hajnal and Opat suggested that diffraction of neutral atoms would be possible using an adaption of the evanescent atomic mirror. By simply retroreflecting the laser which generates the evanescent wave back into the dielectric medium, a standing evanescent wave would be produced. Atoms would then be incident upon a regularly spaced reflective surface, or a mirror grating. It was suggested that for grazing incidence atoms, the apparent grating spacing could be made to be of the order of the deBroglie waves and that diffraction may occur.

The diffraction may also be regarded as a result of multiphoton interactions as the atom absorbs photons from the evanescent wave travelling in one direction and coherently emits photons into the evanescent wave travelling in the opposite direction. Conservation of energy and momentum laws then yield discrete output directions, or diffraction orders, for the atomic beam (Baldwin et al, 1988, 1990). These output channels may have an angular separation of several milliradians. This process is illustrated in figure 2.6.

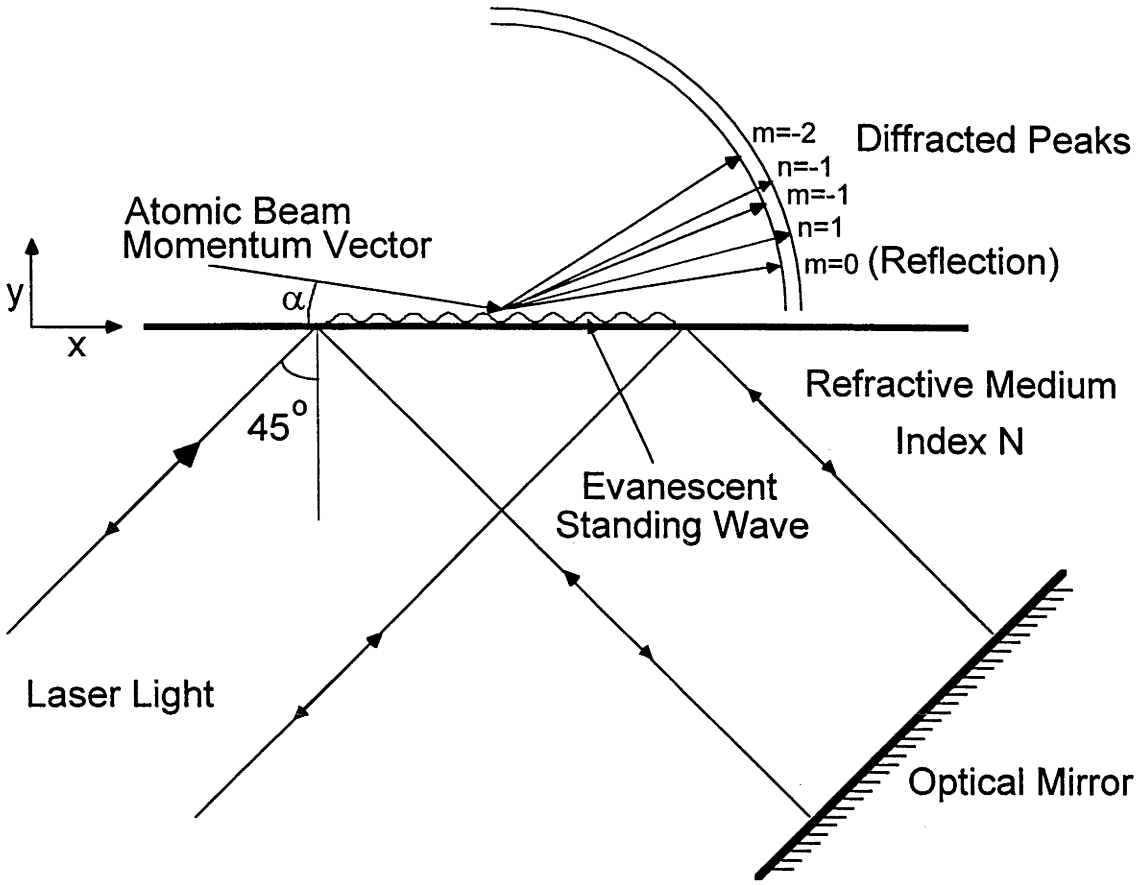

Figure 2.6 : The evanescent grating yields many output channels, or diffraction orders, for a single input channel. Coherent photon exchange between the two fields govern the output channel. Taken from Hajnal et al (1989).

In the figure, the laser light is retroreflected to generate a standing evanescent wave. The atomic beam is incident upon the evanescent grating at a glancing angle α. The (conserved) total kinetic energy of the deflected atoms is represented by the two concentric arcs on the right of the figure. The solid arc is the locus of kinetic energy of deflected atoms equal to the kinetic energy of the incident atoms. The arrows labelled m=0, -1, -2 indicate the discrete output channels in which the atoms may leave the evanescent field.

The m=0 channel corresponds to specular reflection. Where there is no net absorption or emission of photons from either beam, atoms will exit from the interaction region with no momentum change in the x direction in the m=0 channel.

Consider the m=-1 channel. Suppose an atom absorbs a photon from the evanescent wave travelling in the -x direction, and coherently emits a photon into the evanescent wave travelling in the +x direction. After the interaction, the atom will have the same kinetic energy as a specularly reflected atom. The magnitude of the momentum must therefore be the same for the input and output channels. Therefore

$$|p_f| = (p_{x,f}^2 + p_{y,f}^2)^{1/2} = |p_0| = (p_{x,0}^2 + p_{y,0}^2)^{1/2} \tag{2.28}$$

where p_0 and p_f are the atomic momenta before and after the interaction, respectively. The subscripts x and y denote the component in the corresponding direction. After the interaction, the photon exchange will leave the atom with an additional two photon momenta ($2\hbar k$) in the -x direction. That is,

$$p_{x,f} = p_{x,0} - 2\hbar k \tag{2.29}$$

where $p_{x,0}$ and $p_{x,f}$ are the atom momenta in the x direction before and after the interaction, respectively.

Combining the equations (2.28) and (2.29) yields the atomic momentum in the y direction after the interaction

$$\begin{aligned} p_{y,f} &= [\, p_f^2 - p_{x,f}^2 \,]^{1/2} \\ &= [\, p_0^2 - (p_{x,0} - 2\hbar k)^2 \,]^{1/2} \\ &= [\, p_{x,0}^2 + p_{y,0}^2 - (p_{x,0}^2 - 4\hbar k\, p_{x,0} + (2\hbar k)^2] \,]^{1/2} \\ &\cong [\, p_{y,0}^2 + 4\hbar k p_{x,0} \,]^{1/2} \end{aligned} \tag{2.30}$$

where the term $(2\hbar k)^2$ is neglected since, for a 589.0nm wavelength photon, $\hbar k$ corresponds to the momentum of a sodium atom travelling at 3cm/s. This must be compared to $p_{x,0}$, which is the momentum of a sodium atom travelling at around $1000 ms^{-1}$.

Note that the term $4\hbar k p_{x,0}$ in equation 2.30 may be relatively large for grazing incidence angles. For example, the output channel marked m=-1 in figure 2.6 is deflected by an additional 7mrad from the specular reflection channel for a sodium atomic beam of velocity $1000 ms^{-1}$ at an incidence angle of 2mrad.

In general, for the output channels marked m in figure 2.6, the momentum of the diffracted atoms in the y direction is

$$p_{y,f}(n) = [\, p_{y,0}^{2} - 4\, m\, \hbar k p_{x,0} \,]^{1/2} \qquad (2.31)$$

where -m is the number of photon pairs exchanged between the two fields.

The energy and momentum conditions will therefore only be satisfied if the atom leaves the evanescent field at these kinematically determined deflection angles. The discrete deflection angles correspond to integral pairs of photon exchanges between the two fields. This process is the equivalent of the diffraction of an atomic deBroglie wave incident upon the standing wave grating with periodicity $\lambda/2$.

Figure 2.6 also includes channels marked with the label n=1, n=-1 etc. These channels correspond to the case where an odd number of photon interactions occur, and the atoms are excited when they emerge from the atomic mirror (neglecting spontaneous emission). Atoms in these output channels have increased kinetic energy given by the laser detuning. The magnitude of the output momentum is given by the dotted arc in figure 2.6.

However, these kinematic considerations of the input and output boundary condition do not consider the dynamics of the diffraction process. In practice, these atoms which are predicted to emerge from the atomic mirror in the excited state will be attracted to the intense evanescent field. At some time, these atoms may spontaneously emit a photon and revert to a repulsive potential. Alternatively, these atoms may strike the dielectric medium, effectively removing them from any experimental observation.

This theory (Hajnal and Opat, 1989) was the basis upon which the search for atomic diffraction began (Hajnal et al,1989a). The theory was limited, in that it did not consider the dynamics of the interactions within the evanescent grating, and it made only limited predictions of the populations of the diffraction orders. The theory did not provide a prediction of the optimum conditions (laser detuning, polarisation, relative intensities of laser beams) for the search for diffraction. Nevertheless, the diffraction of neutral atoms from an evanescent grating was predicted, and this provided the motivation for the present work.

2.5 Quasipotential Model

Deutschmann et al (1993) proposed a model describing the diffraction process which allowed a greater level of insight into atomic diffraction. Their solution, called the quasipotential model, is described in this section.

The quasipotential model rigorously couples the model used for the gradient force in preceding sections with the diffraction model presented in section 2.4. In essence, it is a description of the dynamical effects within the evanescent field which produce diffraction for a two-level atom.

In their model (Deutschmann et al, 1993), the transition from the incoming de Broglie wave to the diffracted waves is viewed as a redistribution of energy from internal motion and parallel (x) motion into the perpendicular (y) motion. This redistribution takes place via the splitting and recombination of dressed state de Broglie waves at avoided crossings of quasipotentials.

Quasipotentials

The quasipotentials are the potentials discussed in section 2.2 which produce reflection of the atomic beam. In the situation where there are two counterpropagating evanescent waves, the dressed state picture becomes more complicated. Photon exchange between the two fields produces closely separated dressed states. The ladder of dressed states within an evanescent grating are presented in figure 2.7.

Figure 2.7 presents the dressed states with and without interaction for the two-level atom in the standing evanescent grating. There are two optical fields, denoted by n and m. The evanescent wave travelling parallel to the atomic beam contains n photons, and the counterpropagating wave contains m photons. The asymptotic kinetic energy of the atom in the y-direction is denoted by the line T_y.

In the quasipotential model, there are two Doppler shifts associated with the motion of the atomic beam relative to the two evanescent waves. Therefore, in the quasipotential model, the symbol Δ refers to the laser detuning in the laboratory frame of reference ($\Delta=\omega-\omega_0$). The Doppler shift is taken into consideration using the Doppler detuning Δ_D, which equals the shift in frequency due to the motion of the atomic beam.

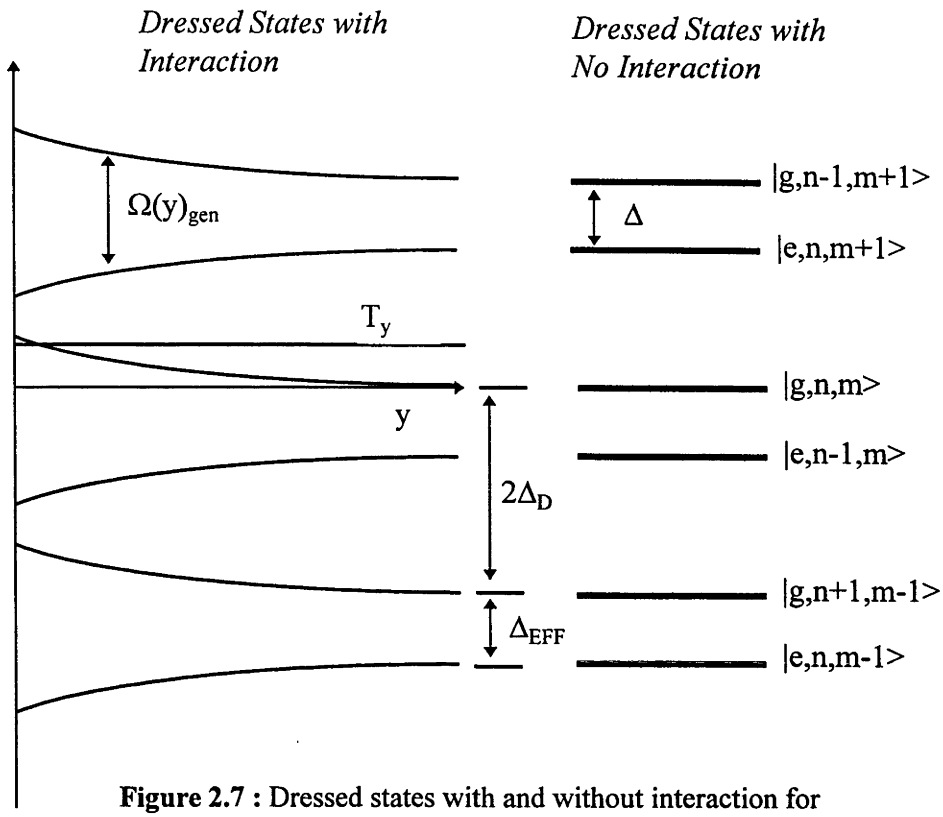

Figure 2.7 : Dressed states with and without interaction for a two-level atom in a near-resonant standing wave. The two optical fields are denoted n and m, the kinetic energy of the incident atom is denoted by T_y.

Although the two laser beams have identical frequency in the laboratory frame, the atomic motion must be considered. The detuning of the copropagating field (n) is effectively $\Delta_{EFF}=\Delta-\Delta_D$, where Δ is the laser detuning in the laboratory frame, and Δ_D is the Doppler detuning due to the motion of the atom in the x direction. The detuning of the counterpropagating field (m) is effectively $\Delta+\Delta_D$.

Thus, if an atom absorbs a photon from field m and coherently emits a photon into field n, the emerging asymptotic state has made a transition from |g,n,m> to |g,n+1,m-1>. The energy difference between these two states is thus twice the Doppler detuning, $2\Delta_D$.

If an atom simply absorbs a photon from field n, the emerging asymptotic state has made a transition from |g,n,m> to |e,n+1,m>. The energy difference between these two states is the effective (Doppler shifted) detuning, $\Delta_{EFF} = \Delta-\Delta_D$.

Note that if the atom were to make a transition from |g,n,m> to |g,n+1,m-1> in the evanescent field, then the asymptotic kinetic energy of the atom (in the y direction) would become equal to $T_y+2\Delta_D$. The atom will therefore leave the evanescent field with a greater perpendicular velocity than the incident perpendicular velocity. The atom is therefore deflected at a greater angle than the incidence angle. This discrete output angle, or channel, corresponds to a diffraction order.

Therefore, transitions between the dressed states in the evanescent field will result in atoms emerging in different asymptotic states which correspond to diffraction orders. The resultant diffraction orders are kinematically equivalent to those described in section 2.4, and arise identically from the exchange of photon pairs between the fields. According to the quasipotential model, the transitions which correspond to photon exchanges in the asymptotic dressed states are possible at the avoided crossings of the quasipotentials.

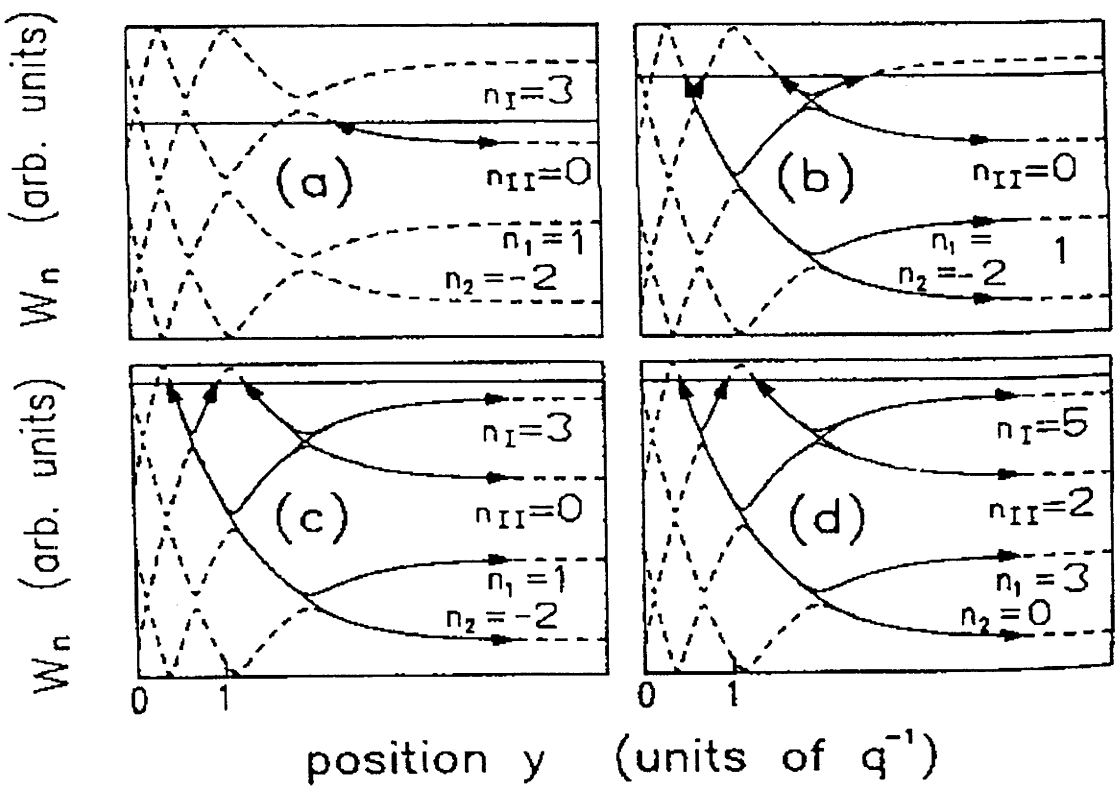

Figure 2.8 : (Dashed) The quasipotentials for a neon atom incident upon an evanescent grating at four different angles: (a) α=35mrad, (b) α=56mrad, (c) α=64mrad, (d) α=105mrad. (Solid) The possible paths taken by the de Broglie wave (atom). Taken from Deutschmann et al (1993).

Avoided Crossings

The separation between the quasipotentials decreases as the laser intensity (Ω_{gen}) increases or the atomic beam velocity (Δ_D) decreases. As they approach one another, the potentials will cross in the diabatic case. In the adiabatic case, the quasipotentials will repel one another. This repulsion gives rise to avoided crossings between the adiabatic potentials. A series of quasipotentials with avoided crossings, taken from Deutschmann et al (1993), is presented as figure 2.8.

Figure 2.8 presents the quasipotentials for an atom incident upon an evanescent grating at four different angles. The quasipotentials are marked with dashed lines. The horizontal lines correspond to the atomic kinetic energy, T_y, which increases for increasing incident angles.

The solid lines depict the quasipotentials which are energetically accessible to those atoms incident in the $n_{II}=0$ (incoming ground state) channel. Note that the avoided crossings with other quasipotentials must be energetically accessible (lie below T_y) for the non-adiabatic transitions to occur.

Figure 2.8(a) presents the scenario where the incident atom is reflected before reaching an avoided crossing. In other words, the atom is not energetically capable of reaching the avoided crossing. The atom will leave the evanescent field in the initial $n_{II}=0$ state, corresponding to specular reflection.

In figure 2.8(b), the angle of incidence (and hence T_y) is increased and the atom has sufficient kinetic energy in the y direction to interact with an avoided crossing. The incoming deBroglie wave can now be coupled to higher diffraction orders through non-adiabatic transitions near the avoided crossings. One interpretation of this model is that when the atom reaches the avoided crossing it may remain in the $n_{II}=0$ potential and follow an adiabatic path as it is attracted to the dielectric. Alternatively, it may make a non-adiabatic transition to the $n_I=3$ potential and continue the reflection process. The possible output channels (diffraction orders) are denoted by solid arrows.

In figure 2.8(c) and (d), the incident perpendicular kinetic energy is sufficient to allow diffraction orders at lower deflection angles than reflection. For example, if an atom is in the state corresponding to $n_I=3$ when it leaves the evanescent field, then the resulting perpendicular kinetic energy (and therefore deflection angle) is much lower than the incident energy (incident angle). This scenario is explored further in section 4.5.

In figure 2.8, the solid arrows indicate possible diffraction orders in which the atom may emerge. An alternative is that some atoms may remain in adiabatic potentials, or may remain in attractive potentials through successive non-adiabatic transitions across avoided crossings. These atoms will become closer to, and may strike, the dielectric medium. This alternative is explored further in section 4.3.

There are a number of variables which affect the probability of the atom making transitions across the avoided crossings, and these are discussed elsewhere (Deutschmann et al, 1993). The focus of this discussion is to determine what transitions are energetically possible, and how the experiment should be configured.

The key to producing populated diffraction orders from this viewpoint is to introduce avoided crossings into the quasipotential diagram. There are two ways of achieving this. The first is to increase the evanescent field intensity to increase Ω_{gen}. This effectively shifts the dielectric boundary to the left in figure 2.8. However, the evanescent field intensity is thus limited by the laser power available in the laboratory. The second method is to decrease the Doppler detuning Δ_D. This will compress the dressed state ladder and produce an ever increasing number of avoided crossings as Δ_D is reduced.

An important consideration in the reduction of the atomic beam velocity (Δ_D) is the effect on the positions of the diffraction orders. From the kinematics given in equation 2.31, the separation of the diffraction orders from an evanescent grating is dependent upon the atomic beam velocity in the x direction relative to the velocity in the y direction. From the quasipotential model viewpoint, the kinetic energy separation in the y direction between the even diffraction orders is equal to $2\Delta_D$. Therefore, as diffraction orders become energetically accessible through the reduction of Δ_D, the energy separation of the diffraction orders will be reduced.

One method (Deutschmann et al, 1993) for decreasing Δ_D is to use a cooled atomic beam. This was not practicable within the constraints of the current project. The novel alternative and the resulting observations are discussed fully in chapter 4.

Chapter 3

Experimental Development

One of the aims of the project was:

- *to construct an improved experimental apparatus to enable diffraction to be measured from the evanescent grating.*

The project involved a great deal of planning and construction of apparatus. This chapter will detail the design principles and apparatus used in the experiments performed.

Section 3.1 contains an overview of the experimental apparatus. It was these ideas which were realised in the construction of the apparatus. Section 3.2 discusses certain fundamental decisions which were made in the design phase of the apparatus. These decisions include which atom to reflect and what method should be employed for detection of the reflected and diffracted atoms. Section 3.3 describes the final experimental systems which were used in pursuit of this project. As far as practicable, the apparatus is broken into functional subsystems which are described separately. Section 3.4 will outline some experimental procedures which may be of benefit to any following this work.

3.1 Overview

Conception

In the most basic conception, the required apparatus for the project must generate an atomic beam, allow the atomic beam to interact with an atomic diffraction grating and measure the results. This requirement is described by figure 3.1. It can be seen that the apparatus can be broken into five distinct sections. They are:

- the atomic beam source
- the interaction region (atomic mirror)
- the detection system
- the optical system
- the vacuum system

The discussion of the apparatus is broken into these five subsystems, and detailed section 3.3.

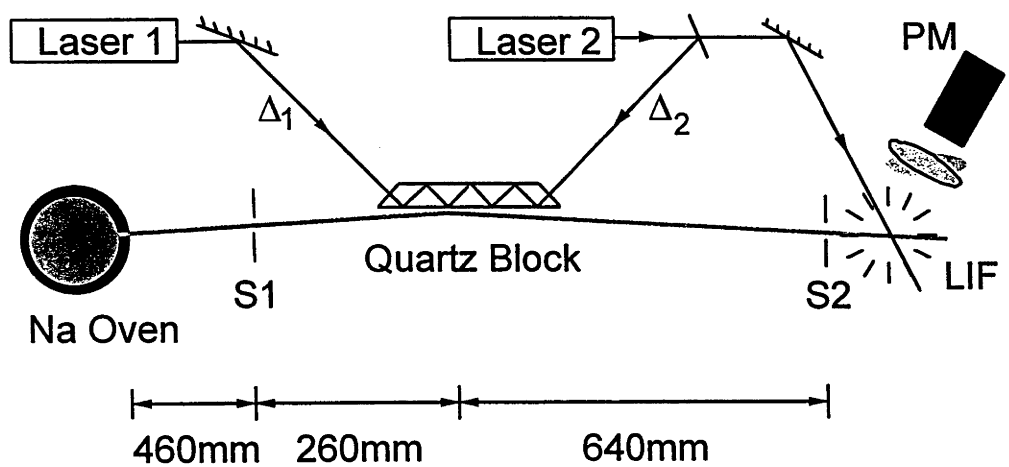

Figure 3.1 : Schematic overview of the experimental apparatus.

Advances

From this broad specification, the project involved almost entirely designing and building the apparatus. Several major advances were made over previous experiments in achieving this. They included:

- velocity selective detection using laser induced fluorescence (LIF) techniques, allowing a velocity resolution of 2%
- improved detection sensitivity by collecting LIF from multiple spontaneous emissions as each atom passes through the detection region
- improved detection sensitivity by collecting a large fraction of LIF with a microscope objective
- increased signal to noise by using a cooled, high quantum efficiency photocathode (optimised for 589.0nm) with a prismatic window
- improved angular detection resolution of 0.16mrad provided by using a 100μm slit scanned at a distance of 640mm from the atomic mirror
- more reliable atomic beam source to yield a constant, high flux atomic beam
- reduced experimental noise by eliminating sodium vapour in the interaction and detection regions

These advances are described in detail in section 3.3.

3.2 Design Fundamentals

Before designing and building the apparatus, a number of fundamental decisions were made to determine the requirements of the apparatus. These initial decisions which shaped the experiment are discussed in this section. The decisions made are firstly, which atom should we use, and secondly, what should be the method of detection.

3.2.1 Which Atom ?

The most fundamental decision to be made to direct the course of the experiment was which atom to attempt to diffract. Around this decision hinged the nature of the atom source, the laser requirements for generating the evanescent field and the scheme for detecting the diffraction.

Candidates which were rejected included:

- barium. Barium was considered due to the experience in the laboratory with barium and its nuclear spin of zero (no hyperfine splitting). Barium was rejected because of its high melting point of 725°C. The requirement that the atomic mirror be heated to this temperature to boil off unreflected atoms precluded barium from further consideration.
- metastable rare gases. Metastable rare gases were considered because they may be readily detected with near-zero background noise. However, it is difficult to produce high density metastable beams. Helium was considered in particular because of its very small mass (and therefore longer deBroglie wavelength for a given velocity / temperature). It was rejected because the wavelength of the transition (1.083μm) was not attainable in the laboratory at that time.

Sodium was selected as the atom with which to perform the experiments because of its many useful properties. They include:

- there was accumulated experience in the laboratory with sodium
- sodium has an achievable melting point of 98°C for evaporation off the atomic mirror
- sodium has a strong D2 line at 589.0nm with a saturation intensity of ~6.3mW/cm^2
- the D2 line is accessible with high laser intensity (500mW) for a ring dye laser using Rhodamine 6G dye (a stable, robust and relatively safe dye which has high efficiency at this wavelength)
- sodium has a small atomic mass of 23 amu

The greatest drawback with sodium was the extensive hyperfine splitting of the D2 line which made theoretical predictions more difficult. This splitting is discussed in more detail in section 3.3.1.

3.2.2 Which Detection System?

The aim of the experiment was to observe diffraction of sodium atoms from the atomic diffraction grating. Since the diffraction angle is dependent on the deBroglie wavelength of the atoms, there was a strong requirement for velocity resolution in the atomic beam.

Previous experiments (Hajnal et al, Baldwin et al) used a hot-wire detector with a time of flight velocity selection system. This provided a velocity resolution of 25% which was found to be insufficient. The velocity resolution was limited chiefly by the response time (~100μs) of the hot-wire detector. Greater resolution could be achieved by increasing the length of the time-of-flight region, but at the expense of signal strength.

Laser induced flourescence (LIF) techniques were selected for the detection system. LIF is described in detail in section 3.3.3. LIF detection techniques were selected for the following reasons:

- LIF provides velocity resolution of 2%
- the detection signal strength can be amplified by multiple emissions from the same atom as it passes through the detection laser
- the atomic velocity being detected may be continuously selected during experimental runs

The two drawbacks of the LIF technique were that:

- the apparatus had to be entirely designed and built
- the apparatus required a third laser (or a novel solution) for the moving grating experiment

3.3 Design

The apparatus required for this project was almost entirely designed and built specifically for this purpose. Apparatus to be produced included large vacuum chambers and control systems. Because of the costs associated with the building of this apparatus, a large emphasis was placed on flexibility and modularity to enable future use of the equipment. These two features are highlighted particularly in the overview of the apparatus, which can be considered as five separate subsystems.

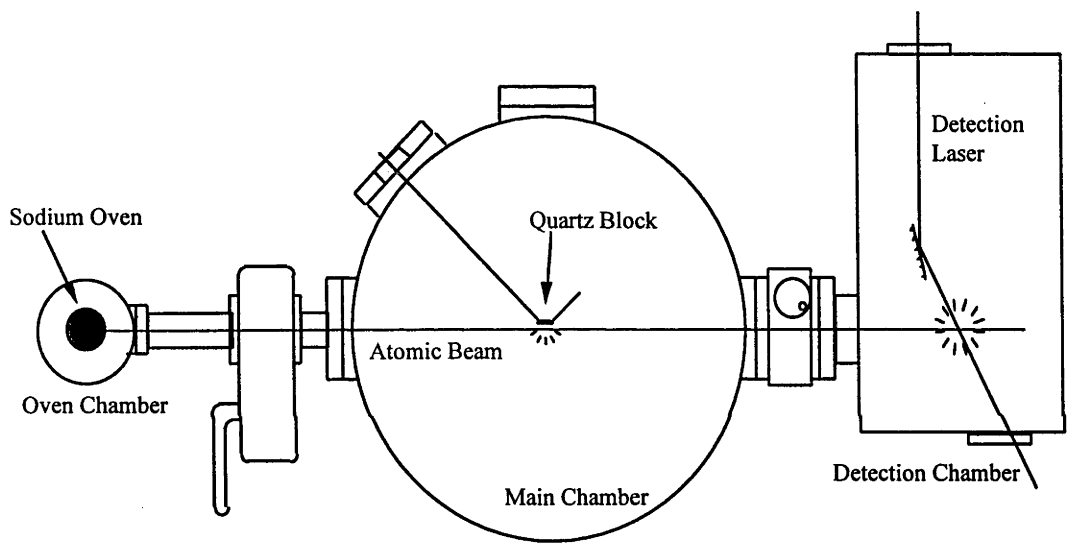

Figure 3.2 : The final design overview of the experimental apparatus.

The final design overview is presented in figure 3.2. There were five major subsystems which had to be brought together to perform the experiments, and they are described below.

- The atomic beam source required the design and construction of the oven chamber, sodium oven and control mechanisms and is detailed in section 3.3.1.
- The interaction region was situated in the already existing main chamber and required the construction of mounting and control systems. It is described further in section 3.3.2.

- The detection system required analysis of the detection technique, design and construction of the detection chamber and detection optics. The final apparatus is described in section 3.3.3.
- The optical system was built from equipment already present in the laboratory and is described in detail in section 3.3.4.
- The vacuum system was separated into three chambers. The oven chamber and the detection chamber were designed and built specifically for this project, while the main chamber was already present in the laboratory from earlier experiments.The complete vacuum system is described in section 3.3.5.

3.3.1 The Atomic Beam Source

Sodium

Sodium was selected for the reasons outlined in section 3.2.1. One drawback of the decision to use sodium in these experiments was the hyperfine splitting of the sodium D2 transition. The splitting is described below.

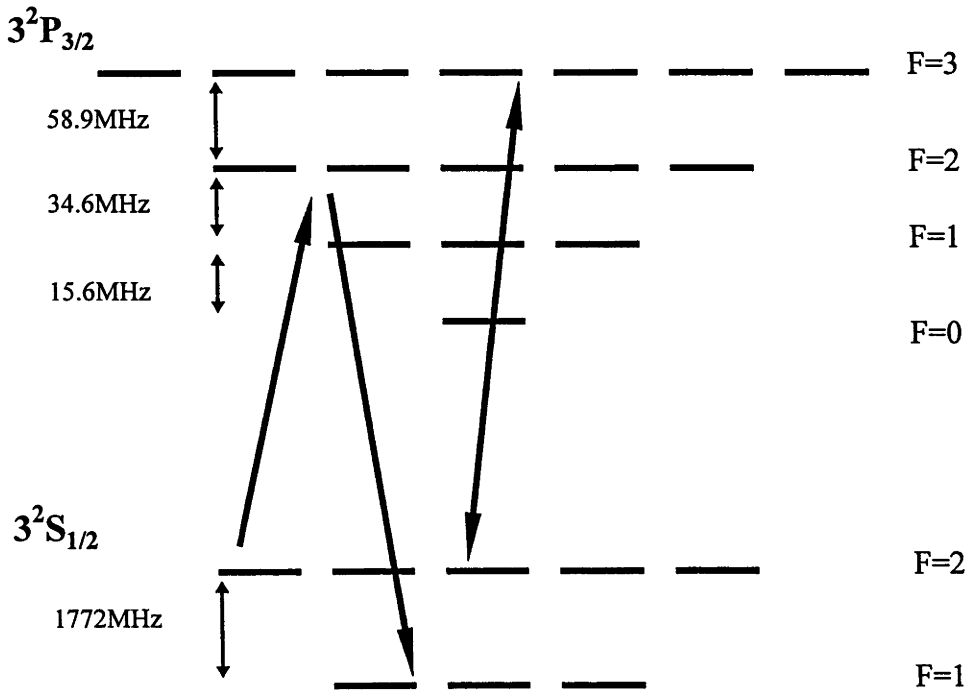

Figure 3.3: Hyperfine splitting of sodium D2 transition

The sodium D2 line has a hyperfine splitting which is described in figure 3.3. The lower $3^2S_{1/2}$ level is split into two hyperfine components (F=1 and F=2), and the upper $3^2P_{3/2}$ level has four hyperfine components (F=0 to F=3).

The detected atoms were those whose velocities brought the detection laser in resonance with the $3^2S_{1/2}$ (F=2) - $3^2P_{3/2}$ (F=3) transition. Spontaneous emission from the $3^2P_{3/2}$ (F=3) level returns the atom to the $3^2S_{1/2}$ (F=2) level, allowing the resonant detection laser to re-excite these atoms. Thus, it was possible to measure multiple emissions from a single atom as it passed through the detection region.

Some atoms with different velocities were resonant with the transitions from the $3^2S_{1/2}$ (F=2) level to the $3^2P_{3/2}$ (F=2 or F=1) levels. These atoms were optically pumped to $3^2S_{1/2}$ (F=1) level. Atoms in this state were far from resonance and would become transparent to the detection system. The fluorescence which occurred during the optical pumping was unwanted noise, and accounted for less than 5% of the detected fluorescence (see section 3.3.3).

In many experiments, the angular momenta of the hyperfine components may be exploited to reduce the effective energy level diagram to two states (Li, PhD thesis). This was not possible in the current experiments because the atomic mirror was illuminated with linearly polarised laser light (see section 3.3.2).

The Sodium Oven

The atomic beam was generated by heating a stainless steel oven containing sodium which could escape through a 350μm pinhole. The design specifications which were used to build the oven are presented as figure 3.4.

The funnel shaped baffles inside the oven are to prevent eruptions in the sodium bath from casting up contaminants and blocking the pinhole, while allowing liquid sodium to dribble back to the reservoir. The oven is sealed with 2.75" conflat flange and copper gasket. To allow good thermal contact between the 2mm diameter Thermocoax (a

coaxial heating element similar to conventional hotplate elements) heating element and the oven, a 2mm groove was machined down the length of the oven. This allowed for the heating element to be wound wherever it was needed. In fact, the top five turns of this groove (at the pinhole) were found to provide sufficient heating of the oven.

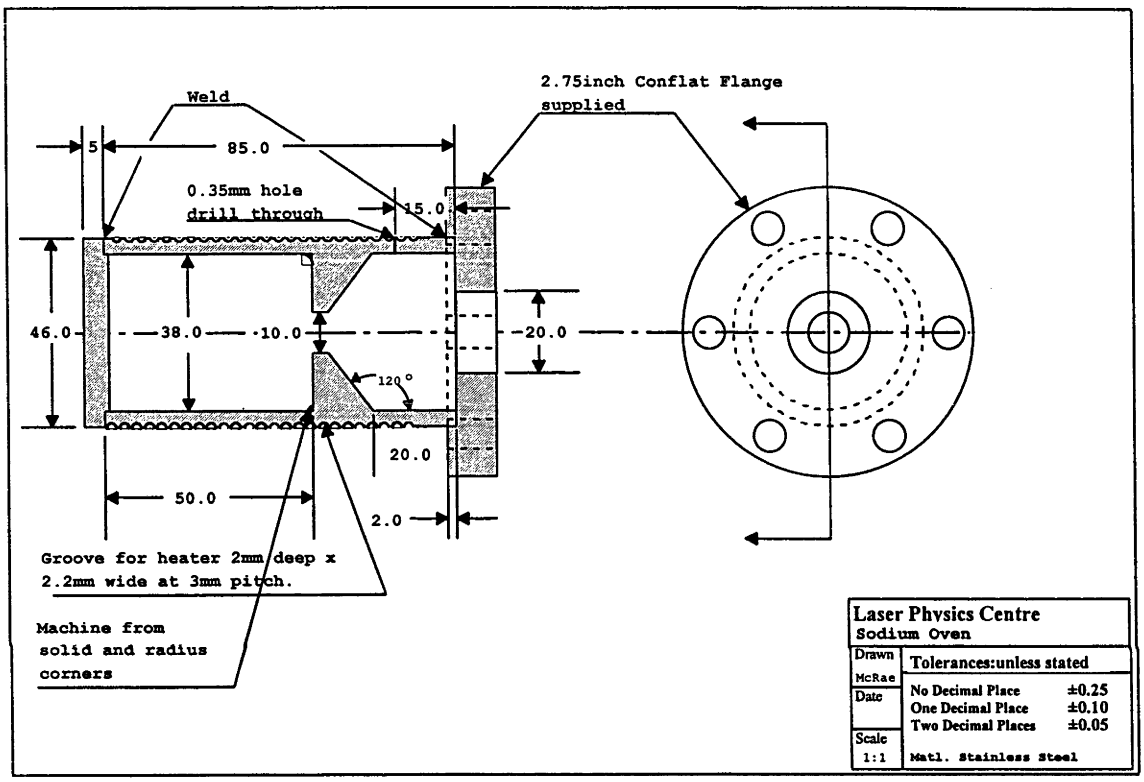

Figure 3.4 : Specifications for the sodium oven. The oven is a stainless steel can, sealed with a conflat flange, with a 350μm pinhole as the atomic beam source. Drawn by Ian McRae

The temperature of the oven was monitored throughout the experiment using two thermocouples. One thermocouple was located at the pinhole and another at the sodium reservoir at the base of the oven. The temperature at the pinhole was set to 680°C by applying 400W to the heating element. The sodium reservoir was initially heated via conduction through the walls of the oven. When there was sodium vapour present in the oven, it also provided heat transfer to the reservoir. The reservoir temperature was typically 520°C during experimental runs. It is worth noting that the reservoir temperature was found to drop significantly when the sodium was depleted.

While a higher oven temperature would provide greater flux in the sodium atomic beam, the loss of sodium in the oven would also increase. The loss of sodium atoms in the oven, L, with an aperture diameter of 350μm was calculated to be

$$L = 5.3 \times 10^{16} \, p / T^{1/2} \text{ atoms/second}$$

where p is the oven pressure, and T is the oven aperture temperature. The value of p depends on T and may be found in the CRC Handbook (1975).

For the aperture temperature of 680°C, a loss of 1 gram of sodium per 30 hours is expected. Increasing the aperture temperature dramatically increases the sodium loss. Experimental downtime for refilling the oven is significant, a minimum of 24 hours. The oven was therefore run at 680°C to compromise atomic beam flux with refill requirements.

The Oven Chamber

A separate, differentially pumped vacuum chamber was designed to house the sodium oven in order to reduce the presence of sodium vapour (which contributed to detection noise) in the interaction and detection regions. The design of the oven chamber had the following requirements:

- The oven must be near to the primary collimation aperture, as the mean free path inside the oven chamber will be small.
- It must be possible to independently control the position of the oven pinhole in the vertical and horizontal directions perpendicular to the atomic beam direction.
- The oven must be heated to around 600°C, while the O-ring seals which mount it are kept cool.
- It must be possible to view the oven and sodium emission inside the chamber.
- It would be preferable if the oven could be removed from the chamber without disconnecting heating elements and thermocouples or dismounting the oven.

The final design met with these five conditions and is shown in figure 3.5. Each of the five conditions is discussed in turn in this section.

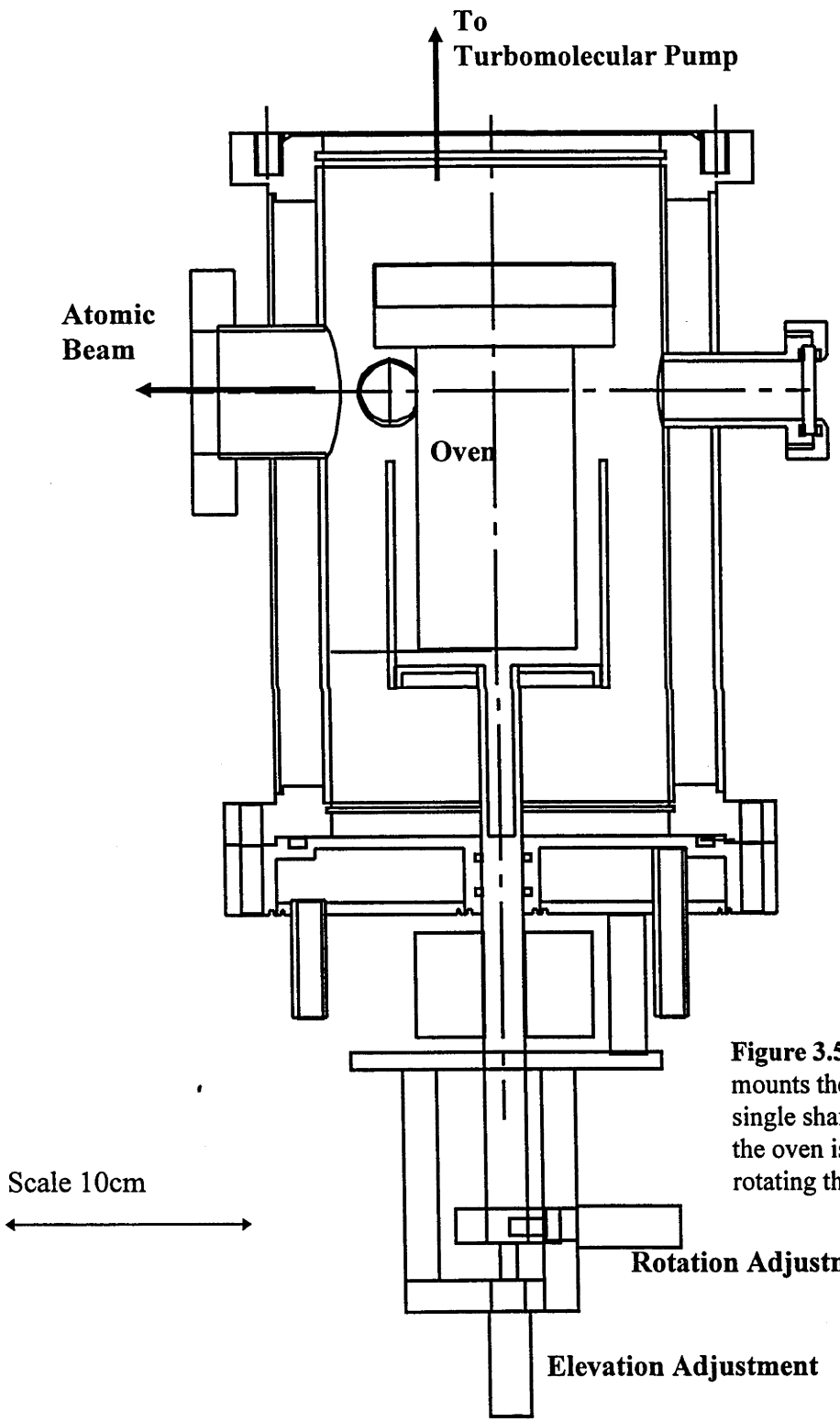

Figure 3.5 : The oven chamber mounts the sodium oven on a single shaft. Position control of the oven is provided by raising or rotating the shaft.

The oven was made near to the primary collimation aperture (first skimmer). The distance between the oven pinhole and the first skimmer was reduced by mounting the skimmer so that it protruded into the chamber. It was found that a distance of 10mm left sufficient space for the placement and removal of the oven. Experiments proved that the skimmer needed to be heated to avoid a buildup of sodium which eventually led to complete blockage of the skimmer. The skimmer was heated by surrounding it with a spiral of heated resistance wire. The wire was kept from electrically contacting the skimmer with ceramic spacers.

Position control of the oven was attained by taking advantage of the large angular spread of the sodium flux. The oven was mounted on a single, vertical rod which could be adjusted using two micrometers outside the chamber. One adjustment would push the rod further into the vacuum chamber, giving vertical control. The other adjustment would rotate the rod, and therefore rotate the oven, by an angle θ. This adjustment would move the pinhole in the horizontal in a direction perpendicular to the atomic beam direction. The sodium flux from the oven is proportional to $\cos\theta$. Therefore, for the small adjustment angles required, there was negligible change in the atomic beam flux.

The oven was heated using Thermocoax heating element. The oven was mounted on three slim pins, and held in place using three long, thin screws to minimise conductive heat loss. The bottom half of the oven was surrounded by a thin cylinder and base of aluminium to act as a heat shield. Also, the mounting and positioning rod was hollowed to reduce heat flow between the heat shield and the O-ring seals. To protect the seals, the entire cylindrical chamber and base was built hollow and water cooled. Additionally, water jackets were clamped around the positioning rod, and above the oven on an elbow which led to the vacuum pump.

Three ports were included in the original oven chamber design. Two allowed viewing across the face of the oven when fitted with windows. Absorption measurements of the

sodium vapour at the oven aperture could be performed. The third port housed the electrical feedthrough required to heat the skimmer.

The ability to remove the oven from the chamber without disconnecting any wires was achieved using the single rod mounting and steering of the oven. All of the electrical feedthroughs for oven heating and monitoring were installed in the oven chamber base. Also, the water cooling pipes to the base were connected with snap fittings for easy removal and replacement. The oven could then be easily removed and replaced when needing refill or repair.

Atomic Beam

The atomic beam path was defined by the primary skimmer and the secondary skimmer. The primary skimmer had an internal diameter of 1mm, and was located 10mm from the oven aperture. The secondary skimmer had an internal diameter of 0.5mm and was located 350mm from the oven aperture, in the entrance port of the main chamber. The aperture of the sodium oven was aligned with the centre of the primary skimmer.

The collimation of the atomic beam was defined by the 350μm diameter oven aperture and a 100μm vertical slit mounted in the main chamber, 460mm from the oven aperture. The atomic beam was therefore collimated to 1mrad. This was confirmed experimentally. Note that the atomic mirror/grating and the detection slit further define the atomic beam path when detecting deflected atoms.

The oven aperture was heated to 680°C, giving a high, constant flux of sodium atoms with velocities between 0 and 2000m/s. The Maxwellian distribution of atomic velocities was found to peak near 1100ms^{-1}. The velocity range of interest for reflected atoms was 700 to 1100m/s. These velocity groups were well populated, while being slow enough to be reflected efficiently from the atomic mirror.

3.3.2 The Interaction Region

The heart of this experiment was the interaction between the sodium atomic beam and the evanescent light field. This section describes the construction and control of the evanescent field.

The Quartz Block

The evanescent laser field used to deflect the atomic beam was produced at the surface of a homosil fused silica block (Hajnal et al, 1989a) which was 25mm long, 6mm wide and 0.375mm thick. The block was bevelled at each end at 45° in opposing directions to allow entry and exit of the laser light. Around 400mW of laser light, tuned to near the sodium D2 line, illuminated the evanescent wave. The laser beams were focussed down to a beam waist of ~350μm, underfilling the 530 μm wide entrance bevel.

For mechanical support, the block was optically contacted to a quartz substrate which had a 2mm wide channel running along its length. This enabled the laser to be totally internally reflected from the quartz vacuum interfaces at both the front and back faces of the block. The reflecting faces were parallel and had a flatness of λ/100 at 633nm. In this way, multiple internal reflections of the laser beam produced an almost continuous evanescent field along the entire length of the block. In order to provide a uniform polarisation for the evanescent field to enable direct comparison with theory (Hajnal and Opat, 1989), the lasers were linearly polarised parallel to the quartz surface.

There was a requirement to heat the quartz block to around 160°C to boil off any sodium which penetrated the evanescent field and stuck to the quartz surface. For this reason, the quartz substrate was mounted with good thermal contact to a brass block. A high power resistor was attached to the back of the brass block, and used to heat the brass and quartz. The temperature was monitored using a thermocouple attached to the quartz substrate. The brass block was isolated from the mounting stages by two slabs of macor, and secured using long, thin screws to reduce thermal conductivity.

The Stages

The quartz block was mounted on two goniometers, a rotation stage, an elevation stage and a translation stage. Their purpose is as follows.

- One goniometer was used in the initial alignment of the system to ensure the atomic mirror was parallel to the atomic beam. That is, to ensure the two ends of the quartz block were at the same height (pitch equals zero).
- One goniometer was used in the initial alignment to ensure the atomic beam would be reflected in the horizontal plane. That is, to ensure that the quartz surface was vertical (yaw equals zero).
- The rotation stage was attached to a mechanical feedthrough, so that the incidence angle of the atomic beam on the mirror/grating could be adjusted during the experiments. The micrometer controlling this stage was calibrated so that the incidence angle could be measured during experiments.
- The elevation stage was used in the initial setup to adjust the elevation of the quartz surface in reference to the atomic beam path, and to ensure the atomic beam was incident upon the cleanest part of the quartz surface.
- The translation stage was attached to a mechanical feedthrough, so that the atomic mirror/grating could be moved in and out of the atomic beam during experiments. This allowed for atomic beam optimisation before the atomic mirror was inserted in the beam, and allowed the mirror to be placed in the peak atomic beam flux.

The Interaction Chamber

The interaction region was housed in a vacuum chamber which was inherited from previous experiments. This interaction chamber was cylindrical and had numerous ports of varying sizes around it's sides. There were 2 mechanical feedthroughs(used for quartz block translation and rotation) and several electical feedthroughs (used for heating the quartz block, chopper power and signal and temperature sensing) in place from previous experiments. There were also two opposing ports of equal height which defined the atomic beam path and two other ports of identical height which were selected for laser input.

3.3.3 The Detection System

In its conception, the detection chamber was to detect diffracted sodium atoms which were deflected up to 10mrad at the atomic grating (Hajnal and Opat, 1989). An angular resolution of better than 0.5mrad was required from the detection system to identify diffracted peaks. Another requirement was to resolve the velocity (deBroglie wavelength) of atoms detected to around 2%, giving an order of magnitude improvement on previous experiments (Hajnal et al, 1989).

Laser Induced Fluorescence

The detection system was built around the concept of laser induced fluorescence (LIF). By intersecting the sodium beam with a laser, atoms of a particular velocity whose Doppler shift corresponds to the laser detuning will be excited, and spontaneously decay, in the field. The sodium D2 linewidth (10MHz) corresponds to a velocity spread of $6ms^{-1}$ when the laser is parallel to the atomic beam.

In the detection system, the angle between the detection laser and the atomic beam was 63°. This corresponds to a velocity spread of $13.2ms^{-1}$ or 2% for an atomic velocity of $660ms^{-1}$. The selected atomic velocity was typically around $800ms^{-1}$ during experimentation, yielding a velocity resolution of 1.6%.

Velocity resolution could be degraded by power broadening. Care was taken to ensure the detection laser was kept around saturation intensities (~$10mW/cm^2$, Shen, 1984) by noting the signal response as a function of laser intensity.

As described in section 3.3.1, the atoms which were detected were those in the $3^2S_{1/2}$ (F=2) state and resonant with the $3^2S_{1/2}$ (F=2) - $3^2P_{3/2}$ (F=3) transition. Note that when the detection laser is resonant with the $3^2S_{1/2}$ (F=2) - $3^2P_{3/2}$ (F=3) transition for a particular velocity group, then it is also resonant with the $3^2S_{1/2}$ (F=2) - $3^2P_{3/2}$ (F=2) or $3^2S_{1/2}$ (F=2) - $3^2P_{3/2}$ (F=1) transitions for other velocity groups. This is important for

the velocity resolution of the system, as the frequency spread of these hyperfine levels is 93.5MHz. The persistent fluorescence of these transitions would therefore degrade the velocity resolution by an order of magnitude. Fortunately, the $3^2P_{3/2}$ (F=2) and $3^2P_{3/2}$ (F=1) states may decay into the $3^2S_{1/2}$ (F=1) gound state which is sufficiently far from resonance to be transparent to the detection system. Therefore, optical pumping depletes the $3^2S_{1/2}$ (F=2) state for those atoms resonant with the $3^2S_{1/2}$ (F=2) - $3^2P_{3/2}$ (F=2) and $3^2S_{1/2}$ (F=2) - $3^2P_{3/2}$ (F=1) transition.

The probability of this optical pumping was calculated using the Clebsch-Gordon coefficients for a linearly polarised detection laser. A computer simulation was employed to determine the population of the hyperfine levels.

The simulation began with the $3^2S_{1/2}$ hyperfine levels equally populated. The effect of the linearly polarised light was simulated by assuming a unit (s=1) saturation intensity. The level population was calculated in finite (2ns) time steps, which were less than the upper state lifetime of 16ns.

Only the $3^2S_{1/2}$ (F=2) state was redistributed into the $3^2P_{3/2}$ (F=1), $3^2P_{3/2}$ (F=2) and $3^2P_{3/2}$ (F=3) states, according to the Clebsch-Gordon coefficients. The laser was detuned 1.77GHz from the $3^2S_{1/2}$ (F=1) state; too far for it to be affected. Spontaneous decay from the upper hyperfine levels was also calculated according to the Clebsch-Gordon coefficients. Atomic populations distributed to the $3^2S_{1/2}$ (F=1) state remained there permanently.

It was found that the fluorescence due to the $3^2S_{1/2}$ (F=2) - $3^2P_{3/2}$ (F=2) and $3^2S_{1/2}$ (F=2) - $3^2P_{3/2}$ (F=1) transitions is quickly damped. With less than 40% of the original population remaining after 100ns, and assuming a detection window of 500ns, their fluorescence constitutes less than 5% of the fluoresence from the desired $3^2S_{1/2}$ (F=2) - $3^2P_{3/2}$ (F=2) transition. Note that the transit time through the detection laser beam was always >1μs, so the fluorescence from the F=3 state dominated.

LIF Detection

In the design of the detection system, there were a number of constraints to be satisfied.

- The fluorescence from the selected atoms is emitted in a random direction. The detection system should maximise the signal by covering as many emission directions as possible.
- The LIF detection technique required a constant angle between the atomic beam and detection laser when scanning the detection apparatus spatially. This ensures the laser remains resonant with one velocity group.
- Angular resolution of the atomic beam of at least 0.5mrad was required.

To ensure a large fraction of the emitted photons were captured by the detection system, a microscope objective was used to collect the LIF. The objective had a numerical aperture of 0.26 and was placed around 7mm from the fluorescence region providing a collection area of 0.22steradians. Additionally, in the initial design, a spherical mirror of radius 25mm was placed 25mm beneath the fluorescence region. Any emission incident upon the mirror would be retroreflected through the fluorescence region and into the microscope objective, thereby doubling the detection area. Unfortunately, this mirror reflected a great deal of scattered laser light into the microscope objective as well, and was therefore replaced with a blackened cavity.

Above the microscope objective lay the microscope. The microscope was a light proof, easily evacuated tube which collimated the signal from the microscope objective. The signal beam was then reflected onto of the photomultiplier. The requirement of the microscope was due to the need to house the (cooled) photomultiplier outside the vacuum chamber.

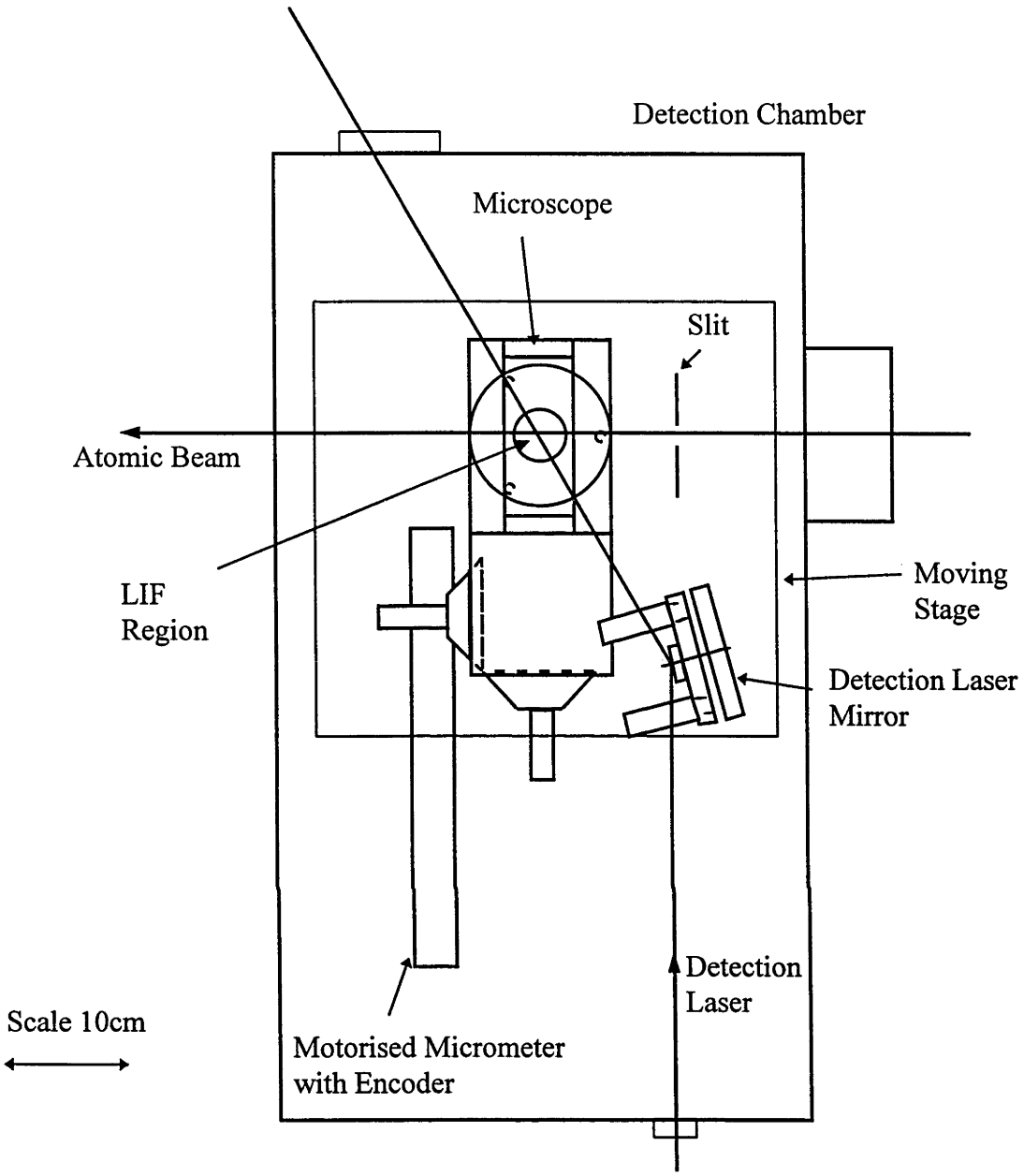

Figure 3.6(a) : Plans for the detection apparatus. Plan view. Drawn by Brett Brown.

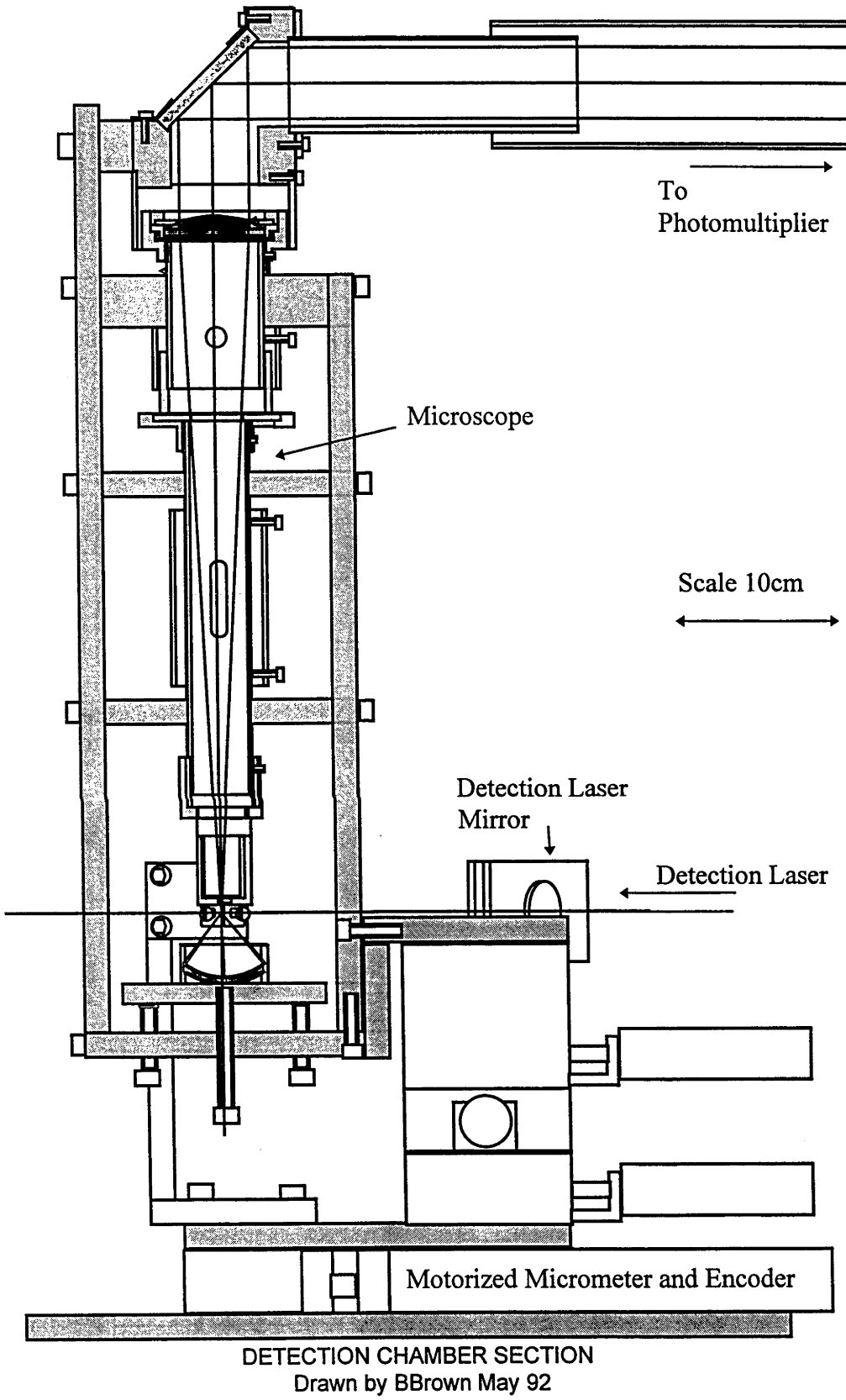

Figure 3.6(b) : Plans for the detection apparatus. Elevation viewing along sodium atomic beam. Drawn by Brett Brown.

The requirement for constant angle between detection laser and atomic beam placed the greatest constraint on the design. The final solution was to move the entire detection apparatus on a translation stage within the vacuum chamber. By simulataneously moving the microscope and the mirror which deflected the detection laser (detection mirror), the *angle of the detection laser beneath the microscope remained constant.* Further, the initial direction of the detection laser was parallel to the motion of the detection apparatus, so that the *location of the detection beam beneath the microscope remained constant.* Finally, the reflected, collimated signal beam from the microscope was parallel to the motion of the detection apparatus, so that the signal beam made a constant spot on the photomultiplier. Figure 3.6 shows the design of the detection apparatus, including microscope, detection mirror and translation stage. The additional three translation stages were used to adjust the microscope position over the atomic beam using motorised micrometers.

It should be noted that while the angle of the detection laser beneath the microscope remained constant, the atomic beam direction changes as the microscope is scanned spatially. There will therefore be a change in the angle between the two beams. The resulting change in velocity group detected is small, being a 0.3% change over the entire parameter space of 10mrad.

Angular resolution of the atomic beam was achieved by placing a 100μm slit before the microscope. The slit was mounted on the translating stage, and provided an angular resolution of the reflected atomic beam of less than 0.16mrad.

Detection Electronics

There were two critical pieces of information from the detection system. They were:

- atomic beam flux
- detection system (slit, microscope and detection mirror) position

The atomic beam flux was measured using the LIF technique, with the fluorescence collected by the microscope and directed into a photomultiplier tube. The Thorn EMI

9658R photomultiplier was chosen for its high quantum efficiency (>12%) at 589.0nm. It has an S20 (trialkali) photocathode, and a prismatic window for enhanced red response. The photomultiplier was cooled to -18°C to reduce dark current. A power supply held the voltage across the photomultiplier dynode chain at -1450V, and could deliver 0.1A to the tube.

Signal from the photomultiplier was fed into a pre-amplifier and then into a lock-in amplifier. The phase signal for the lock-in amplifier was provided by a chopper in the atomic beam, 800mm upstream from the detection region and located in the interaction chamber. The chopper speed was ~70Hz to avoid interference from the 50Hz mains frequency and its harmonics.

The output of the lock-in amplifier was fed into a bank of amplifiers which changed the output signal voltage up to a full scale range of 0 - 10V. This signal was digitised in a bank of a/d converters, and recorded on an IBM PC running DATAK (a data acquisition program written in the laboratory by Peter Manson, 1986).

The laser frequency scans were controlled by DATAK. The laser frequency calibration information was also digitised and recorded using DATAK. These functions are further discussed in section 3.3.5.

The position of the detection system was monitored and controlled using a motorised micrometer with encoder. The encoder was zeroed at the peak of the unobstructed atomic beam, and then used for measuring the angles of deflected beams. The encoder was capable of measuring translation to within 0.1μm, well within the resolution provided by the 100μm detection slit.

3.3.4 The Vacuum System

The experiment required that an atomic beam travel 1.5metres without significant loss to collisions. A mean free path of 5 metres is provided by a 10^{-5}torr vacuum (Moore et

al, 1989). The target pressure in all vacuum chambers was therefore 10^{-5}torr. Additionally, to reduce background sodium levels, a differentially pumped atomic beam source was used. The vacuum system is illustrated in figure 3.7.

The system consisted of 4 sections which required pumping. These were the oven chamber, the interaction chamber, the detection chamber and the differentially pumped section between the two skimmers. These sections were all pumped with 150 litres per second turbomolecular pumps, which were backed by a single rotary oil pump. This configuration provided vacuum of better than $6x10^{-6}$torr in all chambers.

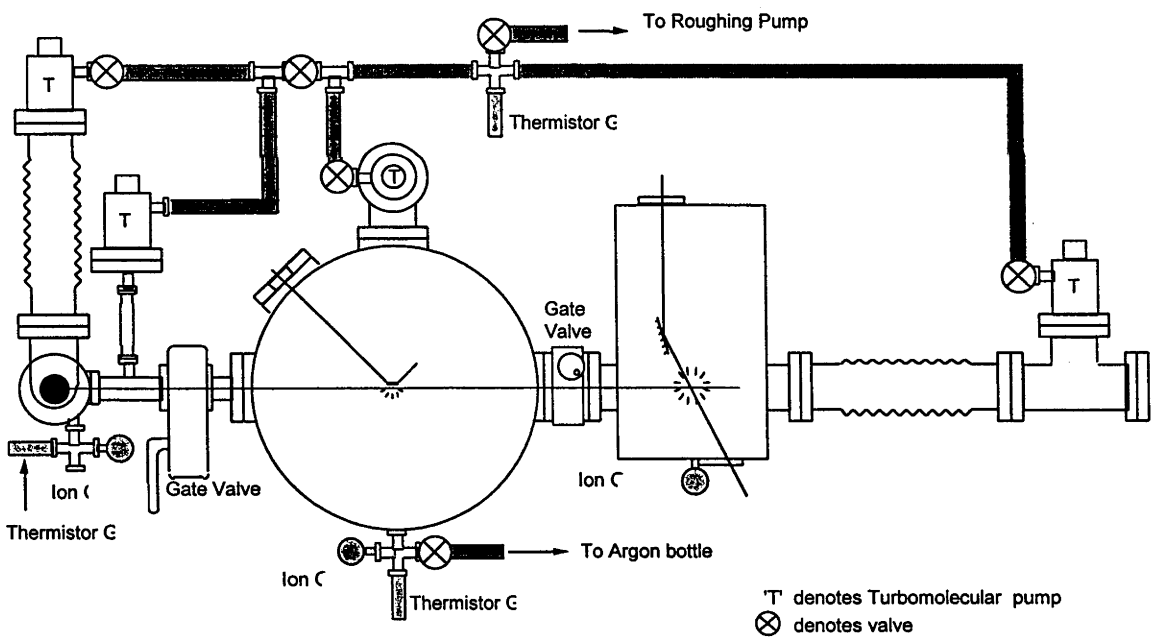

Figure 3.7 : The vacuum system. The gate valves were oriented to isolate the vacuums in the oven or detection chambers. Thermistor and ion gauges were used to monitor vacuum levels.

Pressures were monitored at four places in the vacuum system, as shown in figure 3.7. There were remote ion gauges in the three chambers, and a thermistor gauge on the backing line. The main chamber and oven chamber also had thermistor gauges which were used for vacuum diagnostics.

There existed gate valves between the main chamber and the detection chamber, and between the differential section and the main chamber. When opened, the chambers were always flooded with argon through the main chamber to minimise the pump-down time. The gate valves were oriented to isolate the detection chamber and the oven chamber when the main chamber was opened, so these chambers could remain evacuated.

3.3.5 The Optical System

In the experiments performed in this project, there was a requirement for three high-power, tuneable laser beams at a wavelength near 589.0nm. They were:

- a laser beam to illuminate the evanescent wave. This laser would create the atomic mirror, and would be retroreflected to create the stationary atomic grating.
- a laser beam to counterpropagate against the atomic mirror laser to create a two-colour (moving) atomic grating
- a laser beam to intersect with the atomic beam for laser induced fluorescence detection

The Lasers

Two argon ion pumped, frequency stabilised, ring dye laser systems were used to generate the required laser light. The laser used for detection and generation of the evanescent wave was a Spectraphysics 380D, hereafter 380D. The laser which was used exclusively for generation of the evanescent wave was a Coherent 699, hereafter 699. The dye used was Rhodamine 590 (Rhodamine 6G), which allowed approximately 500 mW output power per laser at the sodium D2 line (589.0nm).

The paths of the laser beams is shown in figure 3.8. A small fraction (10mW) of the 380D beam is split off for LIF detection of the sodium atoms. In the experiments, the 699 beam was used to generate the co-propagating (with the atomic beam) evanescent field. In the initial (stationary grating) experiments, the 699 beam was then retroreflected to generate the counter-propagating field also. In the later (moving grating) experiments, the 380 was used to generate the counter-propagating field as well as the detection laser beam. It is this later configuration which is shown in figure 3.8.

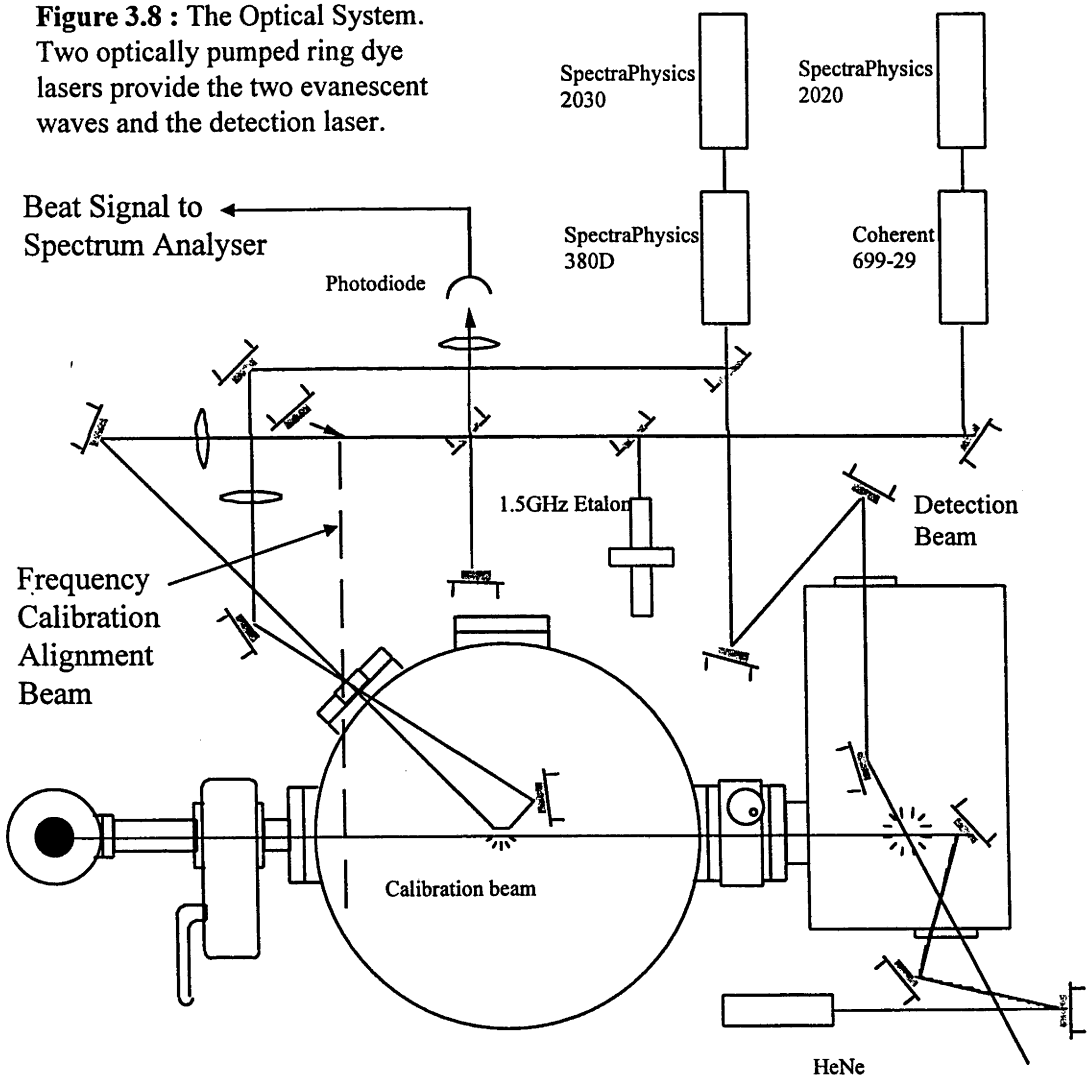

Figure 3.8 : The Optical System. Two optically pumped ring dye lasers provide the two evanescent waves and the detection laser.

The Evanescent Field

The two laser beams which illuminated the evanescent field were focussed to a spot size of 350μm to allow both clean entry into the quartz block and sufficiently overlapping spots on the front of the quartz face. The beams were focused using 750mm focal length lenses which ensured a broad waist centred on the quartz block, creating an almost constant spot size along the 35mm path length through the quartz block. The beams were overlapped precisely, with both beams being fed into the other laser. A Faraday isolator was required to prevent destabilisation of the 699 laser.

Both evanescent waves were polarised parallel to the quartz face to ensure constant polarisation of the evanescent field along the surface of the quartz block.

The laser power entering the interaction chamber was approximately 200mW for both beams. With the spot size of 0.035cm, the laser power entering the quartz block was $160W/cm^2$. This gives a saturation parameter $G=2.5x10^4$ for the incident laser beams. The evanescent field is more intense than the incident beam due to the enhancement of the electric field by the dielectric (Cook and Hill, 1982) and gives an evanescent field strength of $G=3.8x10^4$ for each beam. This evanescent field strength lies within the parameter space of our theoretical predictions. It corresponds to a maximum reflected velocity of $5ms^{-1}$, or a maximum deflection angle of 5mrad for $1000ms^{-1}$ atoms.

The frequencies of the two lasers were varied throughout the experiments. In general, the 380D was detuned approximately 0.7GHz below resonance with the sodium $3^2S_{1/2}$ (F=2) - $3^2P_{3/2}$ (F=3) transition. The precise detuning was governed by the requirements of the detection system. Note that although the 380D was detuned below resonance in the laboratory frame, for the evanescent field the doppler shift of the counter-propagating atomic beam would change the detuning to around 0.7GHz above resonance. The 699 was used as the scanning laser, and was usually scanned from 2GHz below resonance to 8GHz above resonance. These detunings are given with each data set in chapter 4.

Detection Laser

The detection laser was produced by splitting a small fraction from the 380D beam. The beam was focussed to a broad waist of 0.3mm diameter and aligned to be parallel with the detection system motion. Attenuators were employed to reduce the beam power to 0.01mW to provide the saturation intensity of $10mW/cm^2$ required at the interaction region.

The frequency of the detection laser was used to select one velocity group in the atomic beam. At the interaction region, the angle between the detection laser and the atomic beam was 63°. The relationship between detuning and velocity is simply the doppler shift. The atomic beam was travelling away from the detection laser, therefore a positive detuning (above resonance) was required. The relationship between detection laser detuning, Δ_2, and atomic velocity, v_a, is

$$v_a = c.(\Delta_2/\omega) / \cos 63^0$$

The detection laser was detuned according to this relationship. Thus, to select the atoms travelling at 910m/s, a detuning of Δ_2=700MHz was selected.

Calibration

The calibration of the laser frequencies was achieved by calibrating the 699 frequency, and then comparing the 380D frequency to it. The manufacturer's specification for the linewidth of the two lasers was of the order of 1MHz, which is much smaller than the linewidth of the sodium D2 transition of 10MHz.

The position of the sodium D2 lines were located in the 699 frequency scan. The detection system was located to measure the flux of atoms unobstructed by the quartz block. The 699 beam was then intersected perpendicular to the atomic beam (to within 0.5^o) and scanned in frequency. The result was a characteristic optical pumping trace measured by the detection system. When the 699 was resonant with the $3^2S_{1/2}$ (F=2) - $3^2P_{3/2}$ (F=1 or 2) transitions, spontaneous emissions from those excited states would

allow the $3^2S_{1/2}$ (F=2) state to be depleted and the $3^2S_{1/2}$ (F=1) state to become more populated. As the detection system measures the $3^2S_{1/2}$ (F=2) - $3^2P_{3/2}$ (F=3) transition, a depletion of the $3^2S_{1/2}$ (F=2) state corresponds to a reduction in detected atoms, and a reduction in signal. When the 699 frequency reaches the $3^2S_{1/2}$ (F=1) - $3^2P_{3/2}$ (F=1 or 2), this optical pumping will increase the population of the $3^2S_{1/2}$ (F=2) state, causing an increase in detected atoms. These changes in detected atoms served to absolutely calibrate the 699 at two frequencies. This calibration was performed at the beginning and end of experimental sessions, and was used to check for mode hops in the laser frequency. If a change in laser frequency calibration was detected, the data was considered uncalibrated and discarded.

The frequency scale of the 699 was accurately determined. A small fraction of the 699 beam was split off into a confocal, Fabry-Perot etalon with a free spectral range of 1.5GHz. Light passing through the etalon was measured by a photodetector. The signal from the photodetector was passed to DATAK, giving frequency markers every 1.5GHz on a calibration trace. The detuning of the 699 was therefore calibrated precisely relative to the D2 line position to within 20MHz. This calibration was performed for every trace.

The frequency of the 380D was measured against the calibrated 699 scale. A small fraction of each laser was split off and superimposed into one beam. The beat signal between the two lasers was detected by a fast photodetector and fed into a spectrum analyser. When the beat frequency was 250MHz, the spectrum analyser would raise an output voltage. This output voltage was recorded using DATAK on a second calibration trace. By taking the average of the two peaks in the calibration trace, the position of the 380D frequency was found relative to the calibrated 699 scan to a resolution of 20MHz. These beat frequencies were recorded for every scan performed.

3.4 Procedures

The following is a series of procedures used in order to align, adjust or replenish the apparatus.

3.4.1 Atomic Beam Path Alignment

Before an atomic beam was generated, it was necessary to align all of the components of the system. A HeNe laser was used to define the atomic beam path in the following manner. The laser was directed backwards along the atomic beam path from the detection system to the oven chamber, as shown in figure 3.8, with the chopper, quartz block and detection slit removed from the beam path. The laser intensity entering the oven chamber was maximised to determine a central path through the skimmers. The process was more convenient with the removal of the oven.

Components could then by replaced individually, and aligned using the HeNe beam.

3.4.2 Oven Alignment

The oven was located in its mount using three screws. After removal, the oven could be easily relocated if only one screw was loosened during removal. However, this method of relocation was occasionally known to fail due to the thread cut down the sides of the oven. To ensure precise relocation, the HeNe laser beam was used to define the atomic beam path as in section 3.4.1. A small mirror (similar to a dentist's mirror) was inserted into the oven chamber from above to allow a view of the aperture. The oven was then aligned so that the oven aperture was illuminated by the HeNe beam. Note that this method correctly aligns the oven when cold. When heated, the oven needed to be lowered by approximately 0.5mm to account for thermal expansion. The final oven alignment procedure was to maximise the detection signal for the unobstructed atomic beam.

3.3.3 Quartz Block Alignment

The alignment of the quartz block required the alignment of three parameters:

- The pitch. To ensure the two ends of the quartz block were at the same height.
- The yaw. To ensure that the quartz surface was vertical.
- The elevation.

The alignment of the pitch and yaw were very important, as it was critical that the laser beams illuminating the evanescent fields were perpendicular to the bevelled entry surfaces on the quartz block.

First, the quartz block was roughly located so that the HeNe beam defining the atomic beam path skimmed the face. The pitch was aligned by ensuring that the HeNe beam ran parallel to the edge of the quartz block.

The yaw was then aligned. It depended upon the atomic beam path. The atomic beam path (HeNe beam) elevation was measured at both ends of the interaction chamber. The elevation of the atomic beam path was then extrapolated to find the elevation of the atomic beam at a distance of 600mm from the quartz block. A mirror was placed 600mm from the quartz block at an angle of 45° to the atomic beam path, directly in front of the bevelled edge of the quartz block. A laser spot (from the 699) was located on the mirror at an elevation equal to the atomic beam path elevation at 600mm from the quartz block. The yaw of the quartz block and the mirror were adjusted so that the 699 laser beam was retroreflected from the bevelled edge on the quartz block.

Finally, the elevation of the quartz block is adjusted so that the HeNe beam skims past a clean and damage free area.

3.4.4 Detection System Alignment

The detection system alignment required the alignment of:

- the simulated atomic beam
- the detection laser
- the microscope

The atomic beam was simulated by using a short length of wire which was attached to the detection slit and extended horizontally under the microscope. The atomic beam path was defined, as described in section 3.4.1. The short wire was then placed in the HeNe beam, so that it was illuminated along it's length. The reflection of the HeNe beam off the wire simulated the LIF from the atomic beam.

The detection laser was then aligned by intersecting the detection laser with the simulated atomic beam while minimising the scattered detection laser light in the chamber. Next, it was ensured that the initial detection laser direction was parallel to the detection apparatus motion. This was accomplished by quickly moving the detection system along its range of motion, and checking the detection laser spot on the detection mirror was stationary.

Before the microscope was installed, it was adjusted so that the output was collimated for an object at a working distance of 7mm. The alignment of the microscope was then reduced to locating the simulated atomic beam which was illuminated by the detection laser only. This was achieved by removing the photomultiplier and moving the microscope until the illumination was seen by eye. The mirror at the top of the microscope could also be adjusted at this stage.

Finally, after closing the system and pumping down, the microscope could be fine adjusted using the three motorised micrometers to maximise signal for the unobstructed atomic beam.

Chapter 4

Results and Discussion

Two aims of this project were:

- *to demonstrate diffraction of neutral sodium atoms from a standing evanescent field grating*

and later;

- *to investigate the interaction of neutral sodium atoms with a moving evanescent field grating*

This chapter presents the results obtained in the course of attempting to achieve these aims. The results will be presented in the order in which they developed. The chapter is separated into five sections.

The first section contains the preliminary results obtained from the atomic mirror. The reflection of the atomic beam is examined quantitatively and compared to the results expected from the law of reflection.

The second section reports the results of experiments with the stationary atomic grating. This section has a null result, and led to the investigation of the moving evanescent grating described in the following section.

The third section presents the most significant results of the thesis. The resonant behaviour between the atomic beam and the moving (two-colour) evanescent grating is examined. A marked reduction in reflected flux was found to be a doppleron interaction between the atoms and the two laser beams. The dopplerons are explained in detail.

The fourth section presents a complete parameter space search in an attempt to observe diffraction from the moving grating. This section has a null result, but did highlight a number of frequency dependent deflections.

The final section reviews the frequency dependent deflections of the atomic beam. This deflection is explained qualitatively in terms of the quasipotential model.

4.1 Reflection Experiments

When the atomic mirror was illuminated with just one laser, a simple reflection of the atomic beam was expected (Cook and Hill, 1982; Balykin et al, 1987). The results presented in this section show the response of the reflected beam with variations of the incidence angle on the atomic mirror.

The experimental configuration was similar to that shown in figure 3.1, except that the evanescent field was illuminated by only one laser (laser 1), which was propagating in the same direction as the atomic beam, while laser 2 was used solely as the detection laser.

During experimental sessions, after the unobstructed atomic beam was detected and optimised, the quartz block was moved into the atomic beam. The quartz block was rotated by approximately 1mrad and the evanescent field was illuminated. The detection system was scanned spatially to observe the profile of the reflected beam.

Figure 4.1 presents a trace of the atomic flux across the unobstructed beam [A] as well as a second trace which contains the atomic flux across the obstructed beam and the reflected atomic beam[B]. The data presented is taken from a single scan of the detection system.

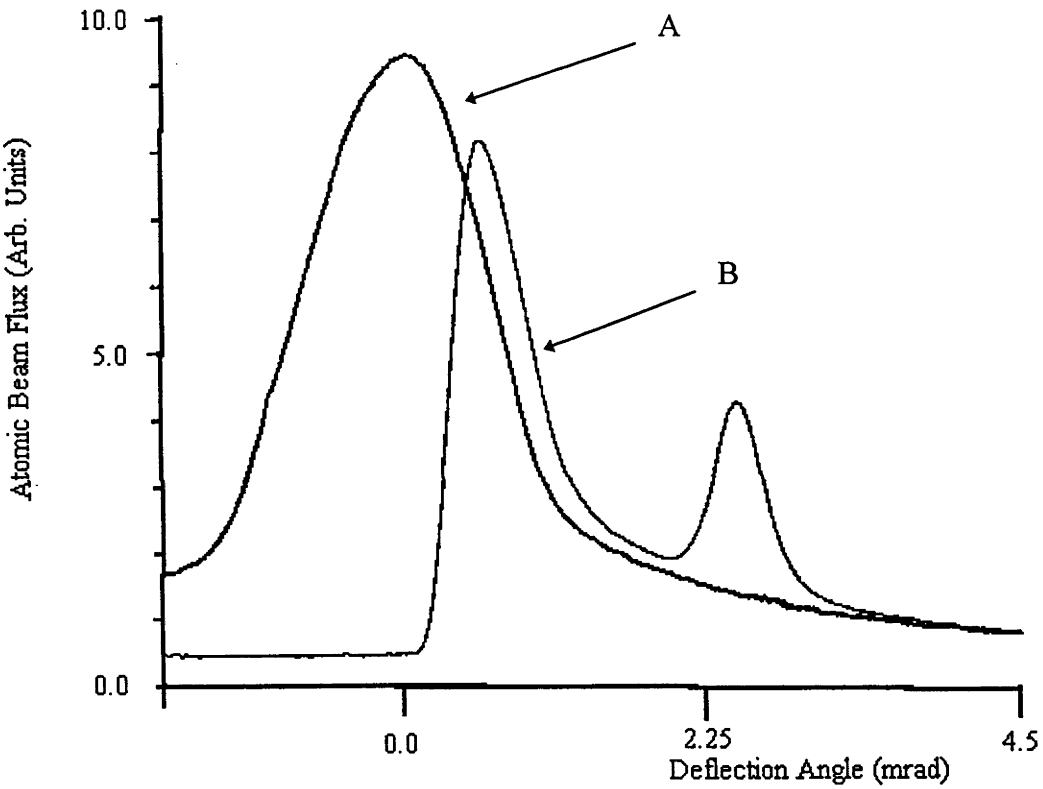

Figure 4.1 : [A] The atomic beam unobstructed by the atomic mirror. [B] The atomic beam obstructed by the atomic mirror and the reflected atomic beam.

Figure 4.1 is presented as an example of the reflected atomic beam which was studied in detail during this project. For these traces, the detection laser (laser 2) was tuned to maximise the signal of the atomic beam (Δ_2=+800MHz) by selecting the most populated atomic beam velocity, v_a, of 1050m/s. The evanescent field was generated

using laser 1 which was detuned to Δ_1=+4GHz. The saturation parameter of the evanescent field was G=3.8x10^4 (see section 3.3.5). The atomic mirror was rotated by 1.1mrad.

The horizontal scale in figure 4.1 is the detection angle subtended from the atomic mirror. The unobstructed beam on trace A has a width of 1.5mrad, which is consistent with the atomic beam collimation of 1mrad (subtended from the source). The reflected peak in trace B is much narrower, with a width of 0.6mrad. This narrowing demonstrates the additional collimation inherent in the reflection process due to the finite width which the atomic mirror presents to the atomic beam. In this instance, the 25mm long atomic mirror is rotated at 1.1mrad, presenting the atomic beam source with a 27.5μm wide reflecting surface. For the reflected beam only, the reflecting surface may be considered an additional collimating aperture of width 27.5μm at a distance of 720mm from the (degraded 450μm diameter) oven pinhole, producing a collimation of 0.6mrad.

When measuring the deflection angle of the atomic beam, it is important to note that the reflected atoms are those incident upon the atomic mirror, not those at the unobstructed beam centre. The incidence position is measured by observing the edge of the obstruction of the atomic beam when the quartz block lies parallel to the atomic beam. The quartz block is rotated about the centre of the 25mm face, so this incidence position is true for all rotation angles. The angle of deflection is therefore the difference between the observed deflected position and the recorded incidence position. For the data presented in figure 4.1, the section of the atomic beam incident upon the atomic mirror lies slightly to the left of the sharp rise at 0.25mrad. The deflection angle for the reflected beam is therefore 2.5mrad minus 0.25mrad, or 2.25mrad.

The broad wings on traces A and B indicate a collimation problem which arose in the atomic beam. These wings became more pronounced over the course of several months of experimentation. The wings are believed to be due to scattering arising from the degradation of the oven pinhole. To eliminate these wings, an additional collimating

blade was introduced in the interaction chamber. The blade was mounted on a swinging arm, 100mm downstream from the atomic mirror, using a motorised micrometer. The blade position was adjusted to obstruct the line of sight between the atomic beam source and the detection slit (when detecting the reflected beam). This procedure eliminated the presence of the wings under the reflected beam until the oven was ultimately replaced. These wings do not appear in any further results in this document.

It may be noted in figure 4.1 that the unobstructed regions of the two traces have differing magnitude. The traces were taken during the initial stages of an experimental session, and have not been normalised to account for the changes in atomic beam flux between the two scans.

4.1.1 Reflected Beam Distribution vs Atomic Mirror Angle

By increasing the incidence angle of the atomic beam on the atomic mirror, the reflected beam was moved away from the unobstructed beam position. There were two competing processes controlling the shape of the reflected beam.

- The subtended width of the mirror presented to the atomic beam was increased as mirror angle increased. This served to effectively increase the width of this collimating component.
- The perpendicular atomic velocity incident upon the atomic mirror was increased as the mirror angle increased. The reflected atoms thus reached a higher potential in the atomic mirror before being reflected. Since the atomic mirror was generated using a Gaussian laser beam, the effective reflection area decreased as the regions in the Gaussian wings became unable to provide the potential required for reflection. The reflected flux therefore decreased as the incidence angle increased.

The intensity of the reflected beam was found to be dominated by the second process. As incidence angle increased, the reflected beam flux became smaller and slightly

broader. In addition, the reflected beam profile became asymmetrical, with greater flux on the low angle side of the beam. This effect was examined further by Snoad (1993).

A number of reflected beam profiles are presented in figure 4.2. As with figure 4.1, laser 2 was tuned to maximise the fluoresence signal from the unobstructed atomic beam (Δ_2=+800MHz => v_a=1050ms^{-1}) and laser 1 was tuned to Δ_1=+4GHz. The saturation parameter of the evanescent wave was 3.8x10^4.

The vertical scale of figure 4.2 has been selected to present the reflected beam shape. The unobstructed beam (at 0mrad) peaks off the scale, and the vertical lines are an artifact of this. Note the wings on the unobstructed beam (present in figure 4.1) are not present in figure 4.2. The results presented in this figure were observed before the degradation of the oven pinhole.

In Figure 4.2, the traces A through D represent spatial scans which show the position and shape of the reflected beam as the atomic mirror is rotated. The atomic mirror angle (or incidence angles of the atomic beam) for the four traces are: [A] 0.3 mrad; [B] 0.6mrad; [C] 1.8mrad; [D] 2.3mrad. Comparison of the four traces indicates that for greater angles of incidence, the reflected peaks do indeed become broader and smaller.

As the reflection angle increases the reflected beam profiles become asymmetric, with greater reflected flux at lower deflection angles. One explanation for this asymmetry is presented here. It is understood that the reflected flux will be reduced as incidence angle increases. Within the incident atomic beam, there is a range of incidence angles upon the atomic mirror due to the finite size of the beam source. Those atoms incident on the atomic mirror at shallower angles are reflected more effectively than those incident at steep angles. There are therefore more reflected atoms at reflection angles on the low deflection angle side of the reflected beam profile.

A more complete explanation of this phenomenon was developed by Nigel Snoad (1993). Snoad developed a comprehensive model using a series of simulated atomic trajectories reflected from gaussian shaped evanescent spots. He found that atoms could be reflected from a single gaussian spot at steeper angles than incidence, and that the reflection was quite diffuse. Atoms reflected from a series of adjacent spots, while being turned in their trajectory a little by each spot, were on average reflected according to the law of reflection. For a series of spots, the incidence angle equalled the reflection angle.

The reason for the asymmetry in the reflection from a single gaussian spot may be determined by considering the spatial spread of incident atoms across the spot profile (peak at x=0). There will be some atoms whose closest point to the quartz block (v_y=0) is at the centre of the gaussian beam (x=0). Those atoms will ride up the potential hill with v_y and v_x both reducing. As they move away from the quartz block, they will roll back down the potential hill, so that the final v_x remains unchanged, while v_y has been reversed. The symmetry of this trajectory about x=0 means that these atoms obey the law of reflection.

However, some atoms which skim across the top of the gaussian spot (x>0) will not encounter sufficient intensity to be deflected significantly and may be lost. Alternatively, those striking the gaussian spot at x<0 will continue to lose v_x after the point of reflection (v_y = 0) as they move to a more intense part of the gaussian spot. These atoms continue to climb the potential hill, reducing in v_x even as they move away from the quartz block in the y direction. The reduction in the final v_x will thus lead to an increased output angle, thereby creating an asymmetric reflected beam with a high angle tail.

The evanescent standing wave mirror in this experiment is in fact a series of ~33 gaussian spots arising from the multiple internal reflections in the quartz block (3.3.2). Snoad demonstrated that the presence of multiple spots reduce the asymmetry in the reflected beam, due to the x<0 trajectories being shadowed by adjacent spots.

However, at high incident angles, this shadowing is less pronounced, leading again to an increased asymmetry. The spreading of trajectories in the high angle tail means that the apparent maximum in the reflection peak is shifted to lower angles. This result was shown in both Snoad's simulations and in the experimental results outlined in the next section.

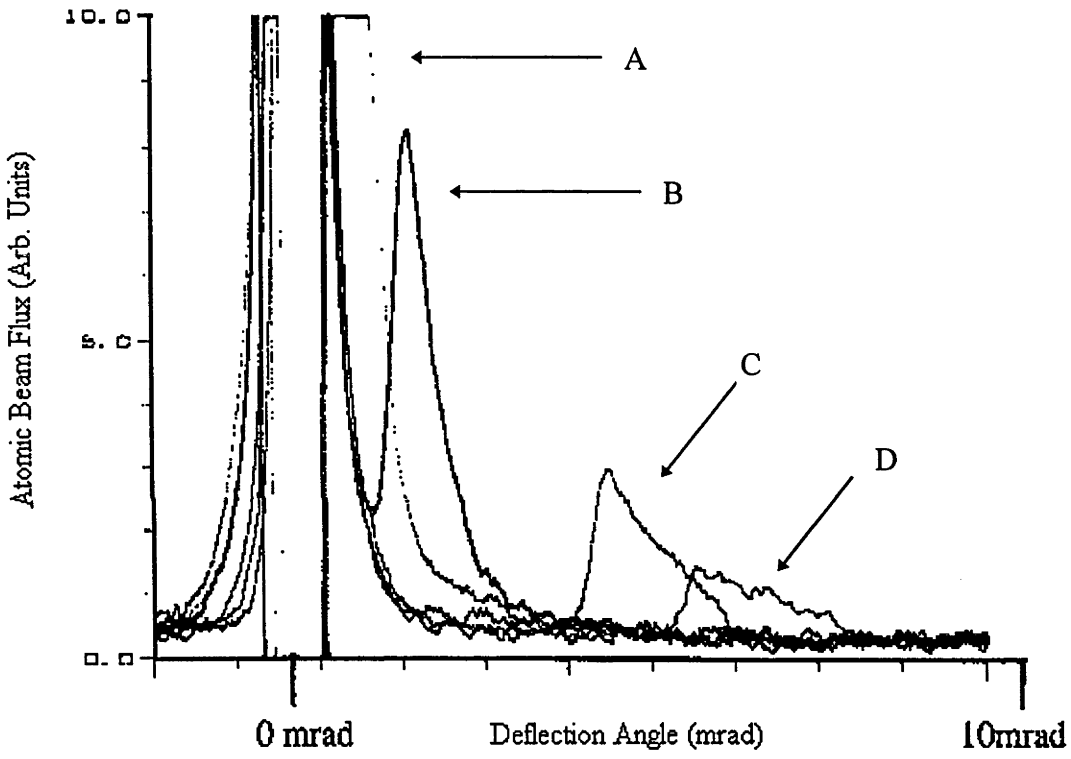

Figure 4.2 : A series of reflected atomic beams. Incidence angles were: [A] 0.3mrad, [B] 0.6 mrad, [C] 1.8 mrad, [D] 2.3 mrad.

4.1.2 Reflected Beam Profile

The deformation of the reflected beam profile is an undesired experimental artifact. When making comparisons with theory, and searching for variations in beam profile which may be attributed to diffraction, it is important to have a well characterised reflected beam profile.

For incidence angles of around 1mrad, the reflected beam profile appeared symmetrical and Gaussian. For incidence angles of 2.3 mrad, the beam profiles were asymmetric. A series of experiments were performed to determine the point at which the asymmetry of the reflected beam profiles occurred.

As the atomic mirror was rotated, the incidence angle of the atomic beam is increased. According to the law of reflection, the angle of reflected flux should be twice that of the atomic mirror rotation. Deviation from the law of reflection indicates the presence of asymmetry in the reflected beam profile. Figure 4.3 presents a compilation of measured atomic mirror angles against the resulting reflected beam direction.

The data in figure 4.3 was taken during three separate experimental runs. For all three series, the conditions were similar. Laser 2 was tuned to maximise the unobstructed beam (v_a=1050±70 ms^{-1}) and laser 1 was tuned to Δ_1=+4GHz. The results were not sensitive to the evanescent field detuning (see section 2.3). The saturation parameter of the evanescent wave was G=3.8x10^4 in all three series. The experiments were repeated to improve the uncertainty in atomic mirror angle calibration. The data series PROFE.22 was later provided by Snoad (1993).

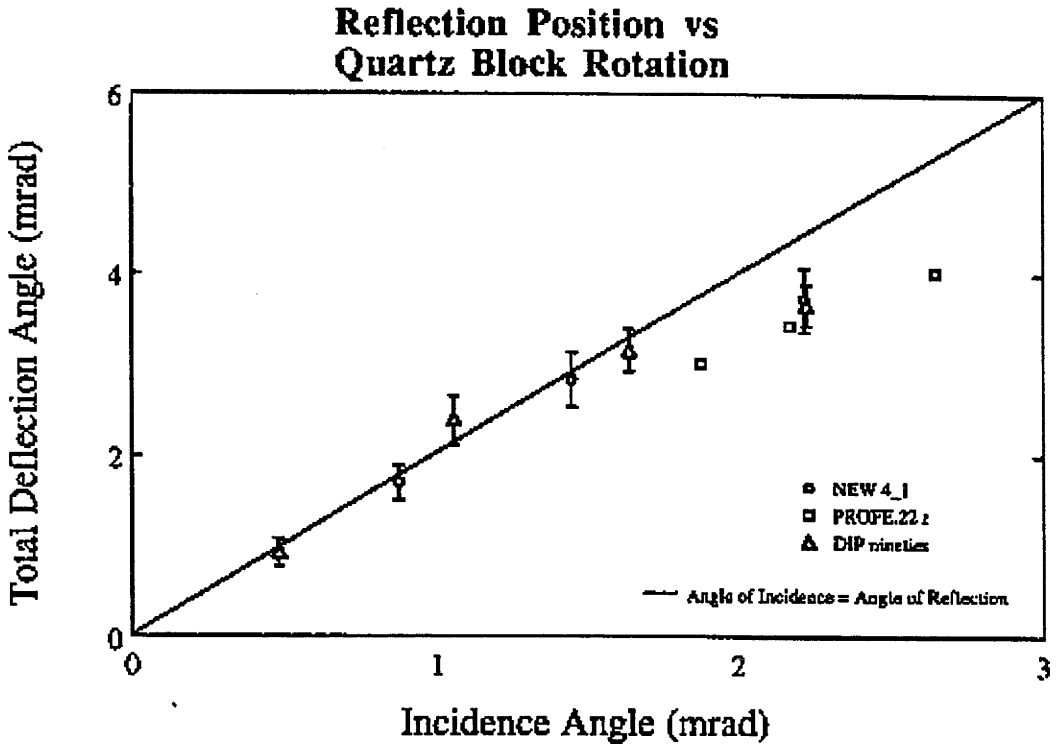

Figure 4.3 : (Points) Reflection angle vs incidence angle for the reflected atomic beam. (Solid line) The law of reflection

The reflection angles plotted were found by measuring the position of the highest point of the reflection peaks. The error bars on the graph represent the full width at half maximum signal from the reflected beam. The solid line denotes the law of reflection, where the angle of incidence equals half the reflection angle. Note that the results are consistent with the law of reflection for incidence angles less than 1.7mrad, but then clearly diverge.

In summary, the observed reflected beam was found to yield symmetrical profiles and thus obey the law of reflection for incident angles of less than 1.7 mrad. At higher reflection angles the incident beam is only partially reflected, with the reflection flux higher for those atoms in the diverging beam which are incident at lower transverse velocities, and therefore shallower incidence angles. The resulting asymmetric reflected beam profiles are shifted towards lower reflected angles.

4.1.3 Reflected Beam Flux vs Laser Frequency

The response of the reflected beam flux to variations in the evanescent field detuning was the focus of these experiments. This section presents the response of the reflected beam flux to variations in the detuning of the single laser (laser 1) generating the evanescent field. This data is valuable for comparison with further configurations described in section 4.3.

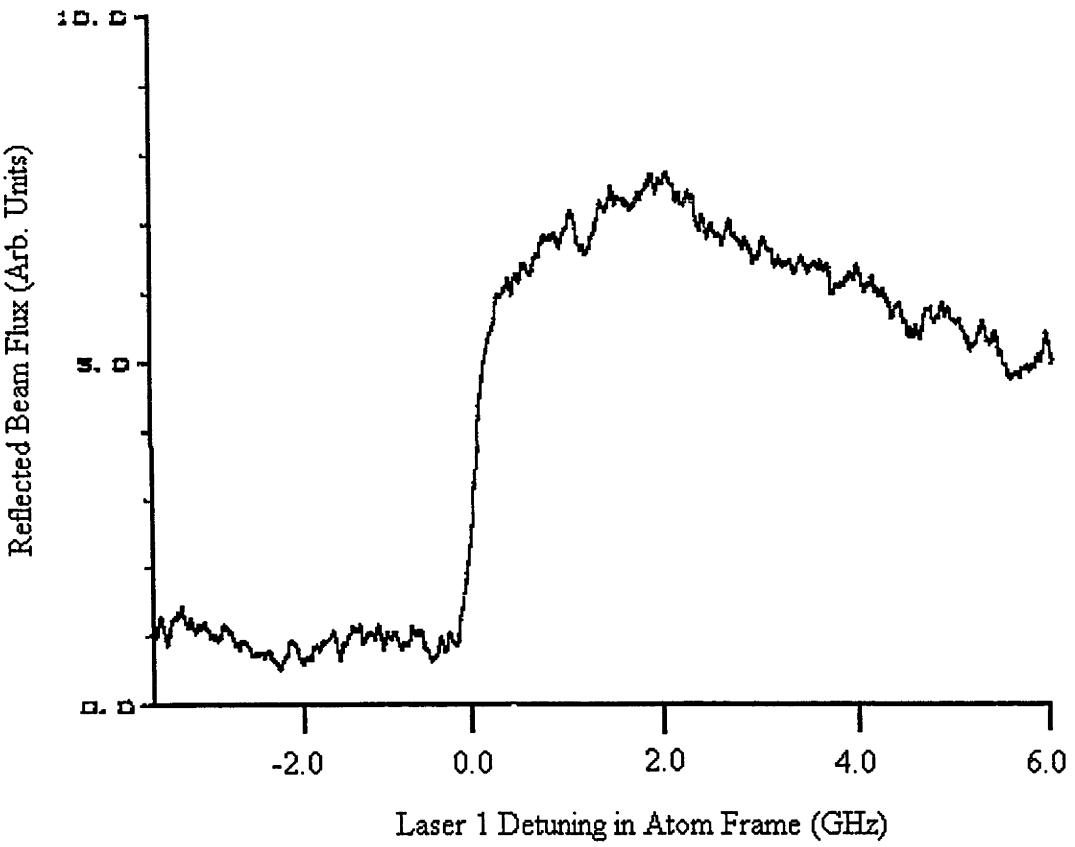

Figure 4.4 : The reflected beam flux as a function of laser 1 detuning (atom frame) for an atomic mirror.

Figure 4.4 presents a trace of reflected beam flux vs laser 1 detuning. The incidence angle of the atomic beam was 2.5 mrad, and the detection system was located at the peak flux of the reflection. The detection laser was tuned to +800MHz, and was resonant with $1050ms^{-1}$ atoms.

The laser generating the evanescent field (laser 1) had a saturation parameter of 3.8×10^4. The detuning, Δ_{EFF}, was scanned from 4GHz below to 6GHz above resonance (in the frame of reference of the detected velocity group of atoms).

Note that below resonance, atoms incident upon the evanescent field are attracted to the quartz block and lost. As detuning increases above resonance, the reflected flux increases sharply between 0.0 and +0.1 GHz, then increases more gradually until it peaks at around +2.0 GHz. At higher detunings the reflected flux gradually decreases, but is still significant at +6.0GHz.

The frequency dependence of the reflected beam flux is similar to the response observed elsewhere (Hajnal et al, 1989; Feron et al, 1993). As the evanescent field is generated using a Gaussian laser beam, the reflected flux is the sum of the reflected atoms from all parts of the Gaussian laser profile. For $\Delta >> \Omega$, the height of the evanescent potential is reduced as the laser detuning increases. The wings of the Gaussian profile gradually become unable to reflect incident atoms and the total reflected flux decreases. This effect is examined in detail by Snoad (1993).

4.2 Experiments with a Stationary Evanescent Grating

The experimental apparatus was reconfigured to retroreflect laser 1 upon itself to produce a standing evanescent field. Reflection was observed and the experiments performed by Hajnal et al (1989) were repeated. Although an exhaustive search was performed of the parameter space, no diffracted sodium atoms were observed.

In the search for diffraction, the detected atomic velocities, v_a, ranged from $700 ms^{-1}$ to $1100 ms^{-1}$ (Δ_2 = +530 to +830 MHz). The lower velocity range was chosen because the atomic mirror was capable of deflecting slower atoms at greater angles. The upper velocity range was selected because it was the most populated velocity group in the unobstructed atomic beam.

To generate the standing evanescent field, a laser intensity of 200mW ($G=3.8x10^4$ per beam in the evanescent field) and detuning of +2.0GHz was used. This field was capable of reflecting sodium atoms with a perpendicular velocity of $6ms^{-1}$. This corresponds to a reflection angle of 5.5mrad for $v_a=1100ms^{-1}$ and 8.5mrad for $v_a=700ms^{-1}$. According to theory (Hajnal and Opat, 1989), the observation of diffraction into a given deflection angle requires that the evanescent wave be able to reflect atoms at that angle (i.e., to transfer the appropriate amount of momentum into the y direction). For example, a $700ms^{-1}$ atom incident at an angle of 2mrad produces a first order diffraction peak at a deflection of 7.8mrad. The evanescent field intensity was therefore just sufficient to provide diffraction in this situation.

By reviewing the results presented in figure 4.2, it can be seen that the noise ratio of the reflected beam signal at the limit of reflectivity is approximately 5%. Therefore, the apparatus was capable of detecting a diffracted atomic beam at a deflection angle of 8mrad, provided the flux of the diffracted beam is sufficiently large.

The theory used (Hajnal and Opat, 1989) did not predict the flux of the diffracted beam for the experimental conditions used. It is concluded empirically that the diffracted beam flux was less than 5% of the reflected beam flux under these conditions.

At a later stage in the project, it was possible to consider the standing evanescent wave case in terms of the quasipotential model (Deutschmann et al, 1993). Figure 4.5 demonstrates the quasipotentials for a standing evanescent wave obtained using the experimental parameters described above. The quasipotentials are the energy eigenvalues of the AC Stark shifted energy levels of the sodium atom. They are calculated by determining the AC Stark shift of the levels in the exponentially decaying evanescent field, as described in equation 2.25 and shown in figure 2.3.

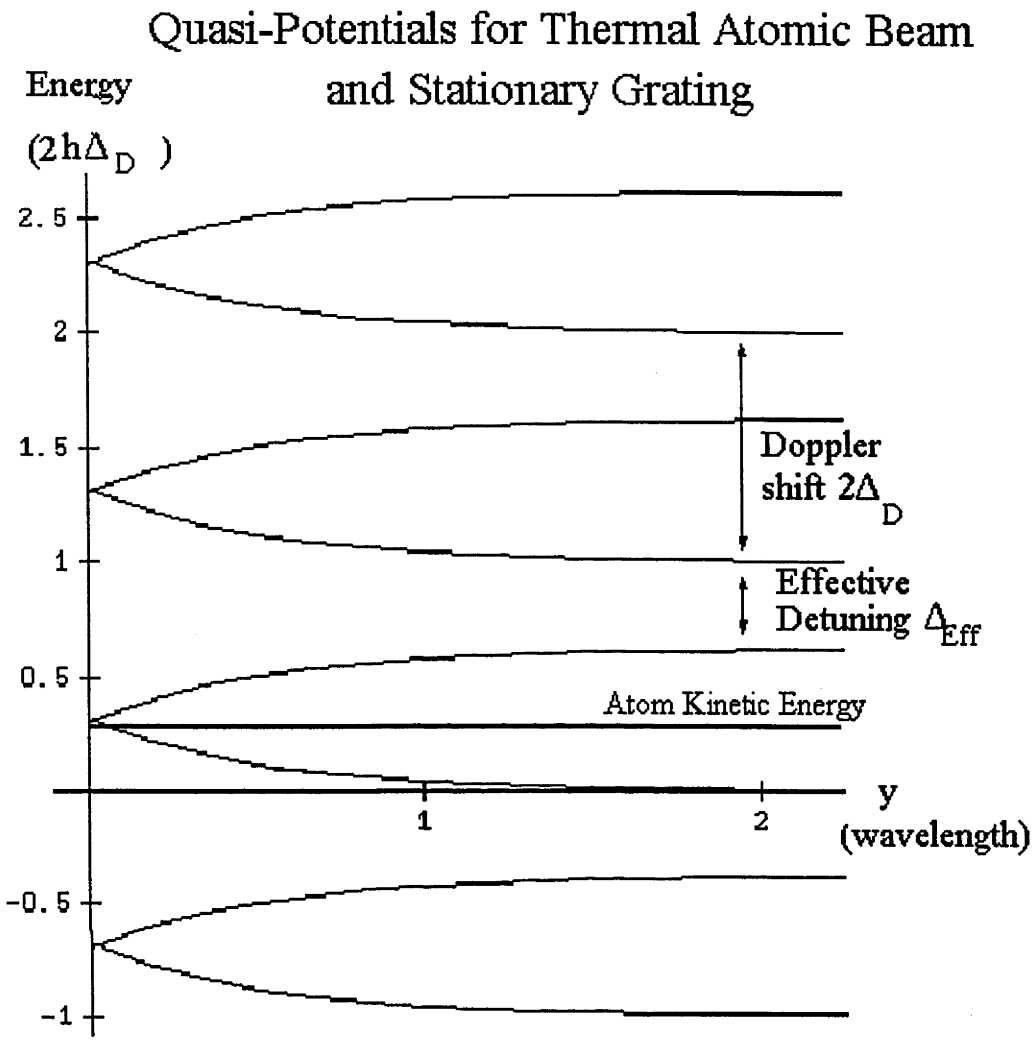

Figure 4.5 : The ladder of quasipotentials for a thermal atomic beam incident upon a standing evanescent grating. The experimental conditions used were $G=7x10^4$, $\Delta=2GHz$, $v_a=900ms^{-1}$ and $\alpha=2.4mrad$.

Note that, according to the quasipotential model (Deutschmann et al,1993 or section 2.5), for diffraction to be observed there must be interactions with at least four avoided crossings. In figure 4.5, the potentials are spaced too widely for avoided crossings to occur. According to the quasipotential model, it is therefore not possibe to observe diffraction for a thermal atomic beam using a standing evanescent field under these conditions.

4.3 Observation of Doppleron Resonances in a Moving Evanescent Grating

Using the quasipotential model (Deutschmann et al, 1993), a necessary condition for the diffraction of sodium atoms is the existence of avoided crossings. There are a number of ways to increase the number of avoided crossings of the quasipotentials in figure 4.5.

- Increasing the field intensity would increase the height of the quasipotentials, allowing for a greater number of avoided crossings. This method was not practical, however, as the evanescent field was at the maximum intensity achievable in the laboratory.
- Decreasing the velocity of the atomic beam would reduce the value of Δ_D, compressing the ladder of quasipotentials and allowing for a greater number of avoided crossings. This method was rejected, however, as a source of slowed sodium atoms was not readily available.
- Increasing the velocity of the grating to near to the atomic velocity would also effectively reduce Δ_D. This method could be achieved by generating the evanescent field with two lasers of differing detuning. This novel technique of using a moving evanescent grating was developed here to overcome the limitations of the first two methods.

The crucial aspect of using the two lasers to generate the moving grating is that the grating may move at velocities very near to the velocity of the detected atoms. It is possible to transform the quasipotential model into this moving frame, and consider the interaction to be between a stationary evanescent grating and a "slow" atomic beam. The theory and results of generating a moving evanescent grating for the compression of the quasipotential ladder are discussed in this section.

The requirement of a third laser (two now required to generate the evanescent field and one for the detection system) was circumvented by using laser 2 to generate both the couterpropagating evanescent wave and the detection laser beam. Laser 1 could then be

tuned independently to control the grating velocity. The experimental configuration is shown in figure 3.1. Note that the detuning requirement for laser 2 determines not only the velocity of the evanescent grating, but also the velocity of the detected atoms. This places a restriction on the phase space over which experiments may be conducted.

To provide the laser beam required to detect atoms near $1050ms^{-1}$, laser 2 was tuned to near Δ_2=+800MHz. In the frame of reference of the detected atoms, the apparent detuning of laser 2 would be $\Delta_2+\Delta_D$. For atoms travelling at $1050ms^{-1}$, Δ_D is equal to 1330MHz. The effective detuning of the counterpropagating evanescent field is therefore around 2130MHz. This detuning is near the peak of the reflection intensity for a single travelling wave.

4.3.1 The Transformation into the Moving Grating Frame

An evanescent grating which is generated using two counterpropagating laser beams of slightly different frequency will be moving. Consider the addition of the two waves travelling in the +x and -x direction

$$I_1 = I_0 \sin(\omega_1 t + k_1 x) \text{ and } I_2 = I_0 \sin(\omega_2 t - k_2 x) \qquad (4.1)$$

where ω and k are the frequencies and wave vectors, respectively. Then

$$\begin{aligned} I_1 + I_2 &= I_0 \sin(\omega_1 t + k_1 x) + I_0 \sin(\omega_2 t - k_2 x) \\ &= 2I_0 \cos 0.5\,[(\omega_1-\omega_2)t + (k_1+k_2)x]\, \sin 0.5\,[(\omega_1+\omega_2)t + (k_1-k_2)x] \\ &\cong 2I_0 \cos[(\omega_1-\omega_2)t/2 + kx]\, \sin[\omega t + (k_1-k_2)x/2] \end{aligned} \qquad (4.2)$$

where $k \sim k_1 \sim k_2$ and $\omega \sim \omega_1 \sim \omega_2$. The result is a slowly moving, standing wave. The velocity, v_g, of the moving, standing wave is found from the cos[..] term in equation 4.2, and is

$$v_g = (\omega_1-\omega_2) / 2k$$

$$= (\Delta_1 - \Delta_2) / 2Q \qquad (4.3)$$

for the evanescent grating case, where Δ_1 and Δ_2 are the laser detunings, respectively, and Q is the wave vector (from chapter 2) of the evanescent field travelling parallel to the surface of the quartz block. The evanescent wave vector, Q, is given by

$$Q = n \sin\theta \; 2\pi / \lambda \qquad (4.4)$$

where n=1.458 is the refractive index of the quartz block, $\theta=45^{\circ}$ is the angle of incidence of the laser beams on the quartz surface and the $\lambda \sim \lambda_1 \sim \lambda_2$ is the laser wavelength in free space.

The quasipotential model may now be transformed into a frame of reference in which the grating is stationary. The resulting parameters of the transformation are denoted with a prime.

In the moving grating frame of reference, the two lasers have the same detuning. The effective detuning of the evanescent field is simply the detuning of laser 1 in the laboratory frame minus a Doppler shifted component for the movement of the grating (Δ_g); that is,

$$\begin{aligned} \Delta' &= \Delta_1 - \Delta_g \\ &= \Delta_1 - Q\, v_g \\ &= \Delta_1 - Q\,(\Delta_1 - \Delta_2) / 2Q \\ &= (\Delta_1 + \Delta_2) / 2 \end{aligned} \qquad (4.5)$$

The detuning of the moving evanescent grating is simply the average of the two laser detunings.

The transformed atomic beam Doppler shift is found by determining the Doppler shift associated with an atom travelling at a velocity $v_a - v_g$. That is

$$\begin{aligned} \Delta'_D &= Q\,(v_a - v_g) \\ &= Q\,v_a - Q\,v_g \\ &= \Delta_D - Q\,(\Delta_1 - \Delta_2)\,/\,2Q \\ &= (2\Delta_D - \Delta_1 + \Delta_2)\,/\,2 \end{aligned} \qquad (4.6)$$

As has already been shown in chapter 3, the value for v_a (and therefore Δ_D) may be derived from the detuning of laser 2 and the detection system configuration:

$$\begin{aligned} \Delta_D &= Q\,v_a \\ &= Q\,\Delta_2\,\lambda\,/\,2\pi\cos 63^0 \end{aligned} \qquad (4.7)$$

The kinetic energy, T_y, associated with the atomic velocity in the y-direction (perpendicular to the quartz block) is an important parameter which needs no transformation into the frame moving in the x direction. It is noted here for completeness, and is equal to

$$\begin{aligned} T_y &= 0.5\,m\,v_y^2 \\ &= 0.5\,m\,\alpha^2\,v_a^2 \\ &= 0.5\,m\,\alpha^2\,(\Delta_2\,\lambda\,/\,2\pi\cos 63^0)^2 \end{aligned} \qquad (4.8)$$

where m is the mass of the sodium atom and α is the (grazing) incidence angle of the atomic beam upon the quartz block.

Using the new parameter set, it is possible to obtain a set of quasipotentials for a moving grating case. A typical case is presented in figure 4.6.

In figure 4.6, the transformed quasipotential model is used to demonstrate the increase in avoided crossings for the moving grating case. The parameters used to generate these quasipotentials are a detection laser detuning (Δ_2) of +700MHz ($v_a = 910ms^{-1}$),

scanning laser detuning (Δ_1) of +1860MHz and saturation parameter of both lasers of G=3.8 x 10^4. These parameters provide a grating velocity of 270ms^{-1}.

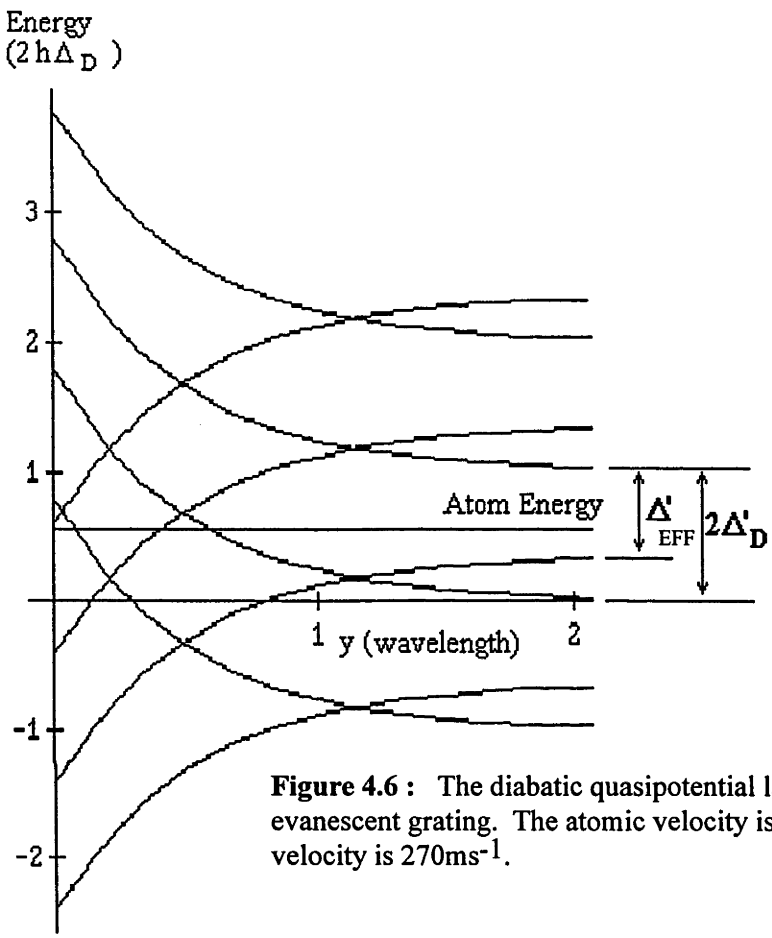

Figure 4.6 : The diabatic quasipotential ladder for a moving evanescent grating. The atomic velocity is 910ms^{-1} and the grating velocity is 270ms^{-1}.

Figure 4.6 presents a model of the quasipotential ladder for the given parameters, and allows the determination of the exit channels energetically accessible to the incident atomic beam. For simplicity in the calculation of a large range of conditions, only the diabatic potentials are used. The diabatic potentials do not interact with one another, and there are therefore no avoided crossings in the figure. The diabatic potentials are used simply to indicate where the avoided crossings would appear. The equivalent adiabatic potentials may thus be visualised by recognising that the avoided crossings of the adiabatic potentials occur at the crossing points of the diabatic potentials.

There are a number of features of note in figure 4.6. Firstly, the Doppler detuning Δ'_D in figure 4.6 is significantly reduced when compared to Δ_D in figure 4.5 (the atom energy is the same in both figures). This demonstrates the desired compression of the quasipotential ladder. Notice also that there is an intersection (avoided crossing) which lies below the atomic kinetic energy in figure 4.6. Incident atoms interact with this avoided crossing, and may either make a non-adiabatic transition to the adiabatic potential above and continue the reflection process, or else remain in the same adiabatic potential to become attracted to the quartz block, and possibly diffracted (as described in section 2.5).

In summary, the quasipotential model may be expressed in the new moving grating frame using the parameters Δ'_D and Δ' which may be found in terms of Δ_1 and Δ_2. The transformed quasipotential model is used to demonstrate the opening up of possible diffraction channels for the experimental conditions used in this experiment.

4.3.2 The Resonance Observations

Experiments were performed to investigate the behaviour of the reflected atomic beam as the grating velocity was varied. The results of these experiments are presented in this section.

Figure 4.7 presents an experimental trace for $910ms^{-1}$ atoms incident at an angle of 2.5mrad to the quartz block. The flux of the atoms measured at the peak of the spatial reflection profile is plotted as a function of laser 1 detuning. The saturation parameters of the two evanescent waves were 3.8×10^4. The detuning of laser 1 is given by the top horizontal scale, which commences at the left-hand side when the two laser frequencies are equal ($\Delta_1 = \Delta_2$ and $v_g = 0$).

The frequency of laser 2 is constant at $\Delta_2 = +700MHz$. The detected atoms therefore have a velocity of $910ms^{-1}$, yielding a value for Δ_D of approximately 1.5GHz. The Doppler shifted detuning of the evanescent wave generated by laser 2 is therefore

+2.2GHz. The frequency difference between the two lasers causes the grating to move with a velocity shown on the bottom horizontal axis. This movement of the grating is described further in section 4.3.1.

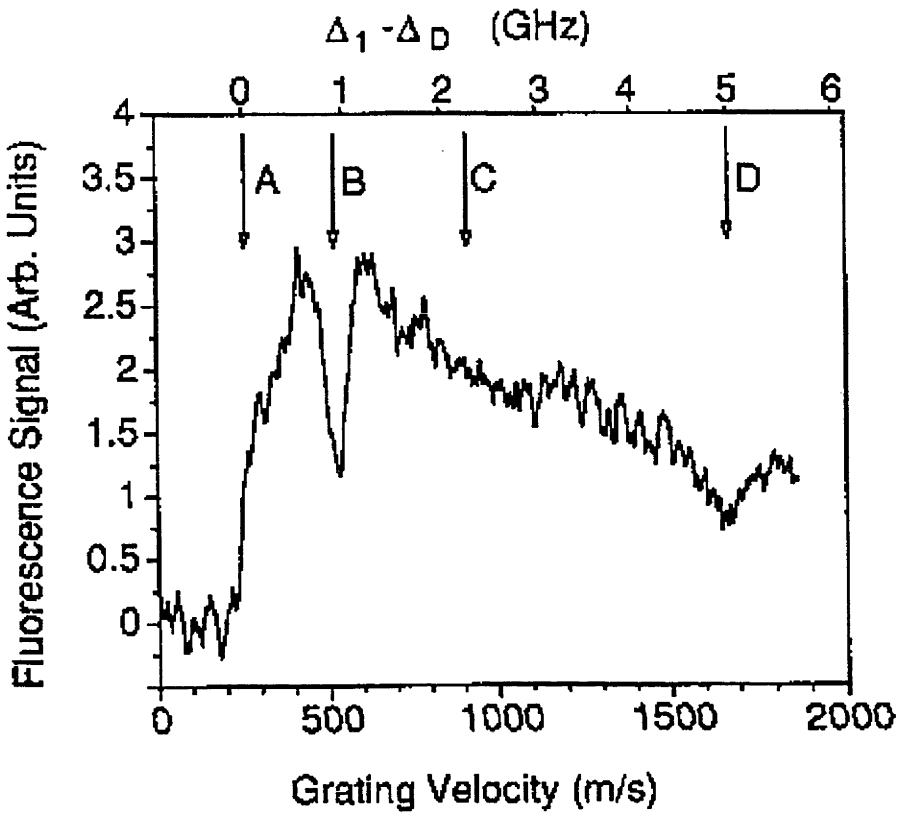

Figure 4.7 : The reflected atomic beam flux as a function of grating velocity for 910ms^{-1} atoms. Note the resonances at B and D.

The zero point on the top scale (point A) marks the frequency at which laser 1 is resonant with the moving atoms ($\Delta_1 = \Delta_D$). When the detuning is negative in the moving atom frame, no reflection is expected from the evanescent field generated by laser 1 alone since its potential is attractive. The small amount of reflected signal for negative detunings is due to reflection by the evanescent wave generated by laser 2.

For positive detunings in the the atom frame, the potential of the evanescent field generated by laser 1 is repulsive. The general behaviour of the reflected signal as a

function of positive laser detuning in figure 4.7 is then similar to the reflection results described in section 4.1.3.

The point C in figure 4.7 marks the laser 1 detuning where the grating velocity is equal to the detected atomic beam velocity. At this point in the moving grating frame of reference, the atomic beam has a velocity v_y and is incident at right angles to the grating. The Doppler shift Δ'_D is equal to zero at the point C. Therefore, the dressed state ladder has compressed to two highly degenerate states (assuming no interaction between the potentials).

In this two laser grating experiment, a resonant decrease in the reflected flux is observed at point B in figure 4.7 for a particular value of Δ_1. A second, smaller resonance is located at point D in the figure. These resonances disappear in the absence of either laser, or upon misalignment of the overlap between the two lasers on the surface of the quartz block. It is concluded that the resonances are not the result of single photon processes, such as optical pumping, but are due to an interaction between the atoms and both laser fields.

The position of the resonances is dependent upon the velocity of the detected atomic beam and the velocity of the grating. As these two parameters were coupled through the use of laser 2, it was not possible to vary these parameters independently. This was a fundamental limitation on the phase space of the experimental parameters. It was, however, possible to make observations of the change in the resonance as laser 2 was varied. Typical experimental results are presented in figure 4.8.

Figure 4.8 presents three experimental traces which were obtained for the atomic beam incident at 1.73mrad to the quartz block. The frequency of laser 2 (and detected atomic velocities) varied between the three traces, and were: [A] 800MHz ($v_a = 1050ms^{-1}$) ; [B] 900MHz ($v_a = 1190ms^{-1}$) ; [C] 1000MHz ($v_a = 1320ms^{-1}$). Laser 2 was scanned from approximately -1GHz to +7GHz in the laboratory (stationary atom) frame. The

detuning in the laboratory frame (Δ_l) was used in this figure because the moving atomic beam frame (Δ_l-Δ_D) of reference is different for each trace.

For the three traces, the point at which reflection occurs (laser 1 becomes repulsive) is different. This is due to the Doppler shift of laser 1 in the atomic beam. Since laser 1 is travelling parallel to the atomic beam, Δ_l must increase to remain in resonance with atoms at higher velocities.

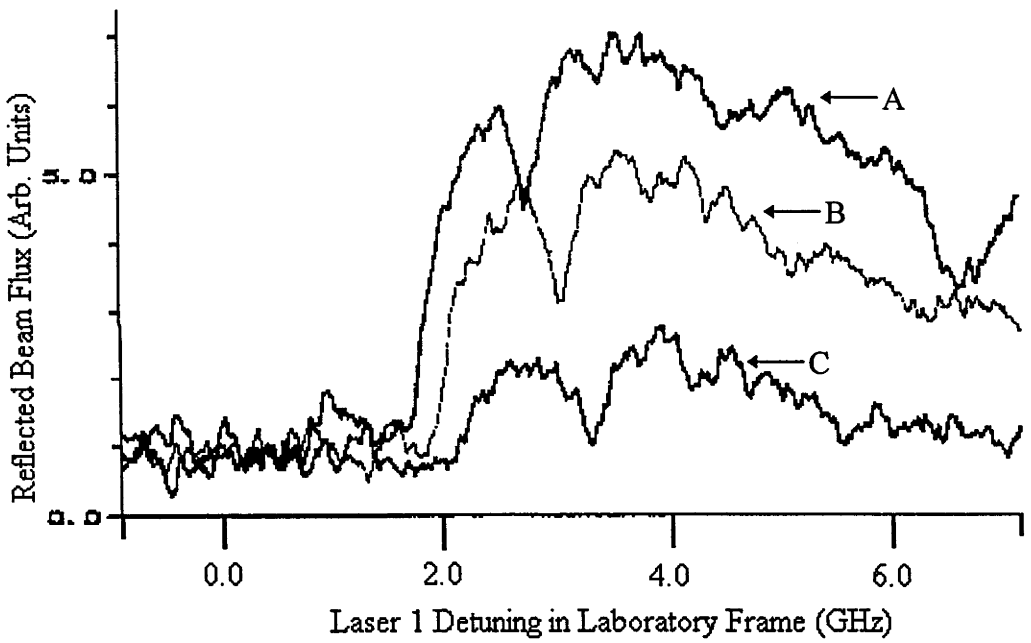

Figure 4.8 : The resonant behaviour in the laser 1 frequency scan is dependent upon the laser 2 detuning. Laser 2 detuning for the three traces were :
[A] 800MHz ($v_a = 1050ms^{-1}$)
[B] 900MHz ($v_a = 1190ms^{-1}$)
[C] 1000MHz ($v_a = 1320ms^{-1}$)

The resonances (similar to those at point B in figure 4.7) also change in position for different atomic velocities. This velocity dependence is a result of these features being produced by doppleron resonances, and is discussed further in the next sections.

4.3.3 The Reflection Loss Mechanism

The explanation for the resonant loss of reflected atoms lies in the quasipotential model. Figure 4.9 presents the quasipotential positions for the experimental conditions at point B in figure 4.7.

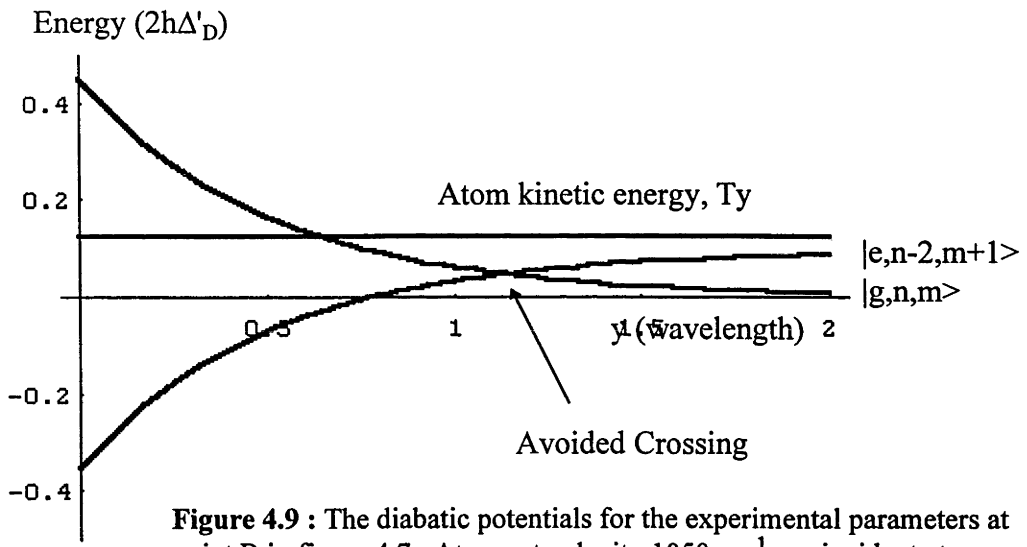

Figure 4.9 : The diabatic potentials for the experimental parameters at point B in figure 4.7. Atoms at velocity 1050ms^{-1} are incident at an angle of 2.5mrad on a 185ms^{-1} grating of detuning 1.33GHz. The diabatic potentials cross, thus indicating the position of the avoided crossing of the adiabatic potentials.

The parameters used to calculate the quasipotential positions in figure 4.9 were Δ_2=700MHz (v_a = 910ms^{-1}) and Δ_1=1.95GHz (the frequency of the point B in figure 4.7). These parameters transform to a grating moving at v_g=185ms^{-1} with a detuning of 1.33GHz. The angle of incidence of the atomic beam upon the quartz block was 2.5mrad. The position of the quasipotentials shown are independent of the saturation parameter, as increasing the laser intensity is equivalent to moving the quartz block boundary further to the left, and extrapolating the potential curves. For figure 4.9, the saturation parameter was G=3.2x10^4.

Under normal reflection conditions, incident atoms are repelled via the gradient force along the (diabatic) evanescent potential. Atoms which are incident upon the moving evanescent grating for these parameters will encounter the avoided crossing between the

two quasipotentials (shown in figure 4.9) as they approach the quartz block. At the avoided crossing, the atoms may do one of two things:

- The atoms may continue the reflection process by making a non-adiabatic transition to the higher adiabatic quasipotential (|e,n-2,m+1>) at the avoided crossing. The atoms will then be reflected where the potential energy is equal to the kinetic energy, T_y. As the atoms travel away from the quartz block, they will encounter the avoided crossing for a second time. At this point, the atoms may do one of two things:
- The atoms may make a non-adiabatic transition to the original |g,n,m> adiabatic potential to continue the reflection process. The results of atomic reflection are presented in section 4.1.
- Alternatively, the atoms may remain in the |e,n-2,m+1> adiabatic potential. These atoms will be attracted to the quartz block, and will be slowed as they travel out of the field and up the adiabatic potential |e,n-2,m+1>. The atoms will undergo spontaneous emission, and emerge in the ground state. The final perpendicular velocity, v_y, of these atoms will be smaller than the incident perpendicular velocity due to the time spent in the attractive potential. Observations of this process (or similar) are presented in section 4.5.
- Alternatively, when the atoms encounter the avoided crossing for the first time, they may remain in the |g,n,m> adiabatic potential which becomes attractive. These atoms will be drawn towards the quartz block. These atoms may not be reflected but instead strike the quartz block and be lost. This leads to the reduction in the reflected atom flux observed for these conditions (point B in figure 4.7). The dependence of this process on the velocity of the atomic beam and grating is discussed in detail below.

Note that those atoms in the |g,n,m> state being drawn towards the quartz block will probably undergo spontaneous emission, and resume the reflection process. The resonances were found to be more pronounced if the incident velocity was close to the reflection limit of the evanescent field. In this situation, the small period of time for the atom in the attractive potential is sufficient to cause it to collide with the quartz block.

4.3.4 The Doppleron Resonances

The doppleron condition is normally expressed in terms of the bare states of an interaction |g> and |e>. The doppleron resonances correspond to exchanges (through successive coherent absorption and stimulated emission) of photons between the two counter-propagating fields comprising the standing wave. Doppleron resonances are denoted with a parameter n which corresponds with the number of photons exchanged. The n=+1 photon is the trivial case where one laser field is in resonance with the atomic transition. There are two possible doppleron resonances which exchange three photons between the field, as shown in figure 4.10.

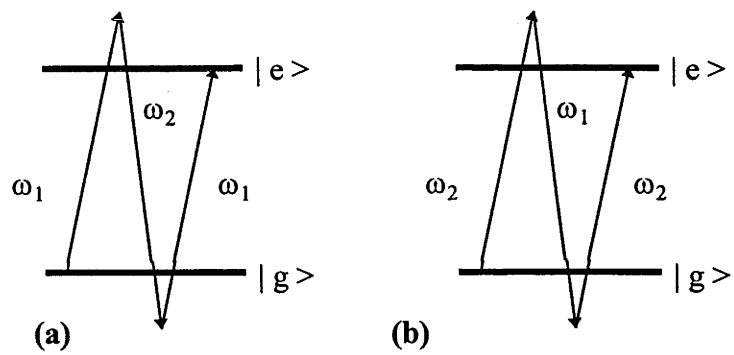

Figure 4.10 : The doppleron (multi-photon resonance) conditions (a) n=+3 doppleron (b) n=-3 doppleron.

In figure 4.10(a), the n=+3 doppleron condition is

$$\omega = 2\omega_1 - \omega_2 \qquad (4.9)$$

This condition occurs near point B of figure 4.7 (see Stenlake et al, 1994). Equation 4.9 may be expressed to include the motion of the atoms as a function of the moving grating parameters by considering that for the moving grating condition,

$$\omega_1 = \omega + \Delta' - \Delta'_D \qquad (4.10)$$

and

$$\omega_2 = \omega + \Delta' + \Delta'_D \tag{4.11}$$

Substituting equations 4.10 and 4.11 into 4.9 yields the doppleron condition for the non-interacting states in the moving grating frame to be

$$0 = \Delta' - 3\Delta'_D \tag{4.12}$$

Similarly, in figure 4.10(b), the doppleron condition corresponds to

$$0 = \Delta' + 3\Delta'_D \tag{4.13}$$

In general, the doppleron condition for a multiphoton interaction is equal to

$$\Delta' = n\Delta'_D \qquad (n \text{ is odd}) \tag{4.14}$$

Note that the doppleron conditions described by equations 4.12 to 4.14 are the conditions for the bare states |g> and |e>. For $\Omega >> \gamma$, the AC Stark shift of the interacting dressed states must be considered. The quasipotential model is used to determine the doppleron conditions.

In the quasipotential model, the multiphoton doppleron transition is equivalent to a non-adiabatic transition at an avoided crossing. An atom which makes a non-adiabatic transition at the avoided crossing in figure 4.9 is making a transition between the interacting dressed state |g,n,m> and the interacting dressed state |e,n-2,m+1>. In the limit of no interaction, these two states correspond to the initial and final states of the n=+3 doppleron resonance transition. The presence of the avoided crossing therefore allows a transition between the dressed states which corresponds to a doppleron transition in the asymptotic states.

The doppleron resonance condition described by figure 4.10 corresponds to the bare state definition of a quasipotential (equations 4.12 to 4.14). This is where the "avoided crossing" occurs when the two quasipotentials are equal in the far field. The diabatic quasipotentials corresponding to this situation are presented graphically in figure 4.11a. This quasipotential condition may be found in terms of the moving grating frame parameters (from figure 4.6) and is described by

$$\Delta' = n\,\Delta'_D \qquad \text{(n is odd)} \qquad (4.15)$$

which is identical to equation 4.14.

In the dressed state model, the doppleron resonance conditions may be met for the atom in the far field. In addition, the doppleron resonance conditions may be met for the atom when subject to an intense field producing an AC Stark shift of the dressed states. An atom which is being reflected encounters a range of evanescent field intensities, and therefore a range of doppleron resonance conditions. There is therefore a band of conditions which meet the doppleron resonance conditions at some point in the reflection process. The limitations of this band are defined by the condition that for the doppleron resonance conditions to be met, the atom must encounter an avoided crossing during the reflection process. (This condition coincides with the presence of the reflection loss mechanism described in the section 4.3.3.) The lower bound on the position of the avoided crossing is defined by figure 4.11(a).

The upper bound corresponds to the point where the avoided crossing lies at the atomic kinetic energy, T_y. The diabatic quasipotentials corresponding to this bound are presented graphically in figure 4.11b, and is described (in the moving grating frame) by

$$\Delta' = +/- (n\,\Delta'_D + 2T_y) \qquad (n \text{ is odd}) \qquad (4.16)$$

where the separation of the dressed states in the far field is equal to $2T_y$. Note that an avoided crossing may exist above the energy T_y, but in this case the atom is not sufficiently energetic to penetrate to the high intensity field to interact with it.

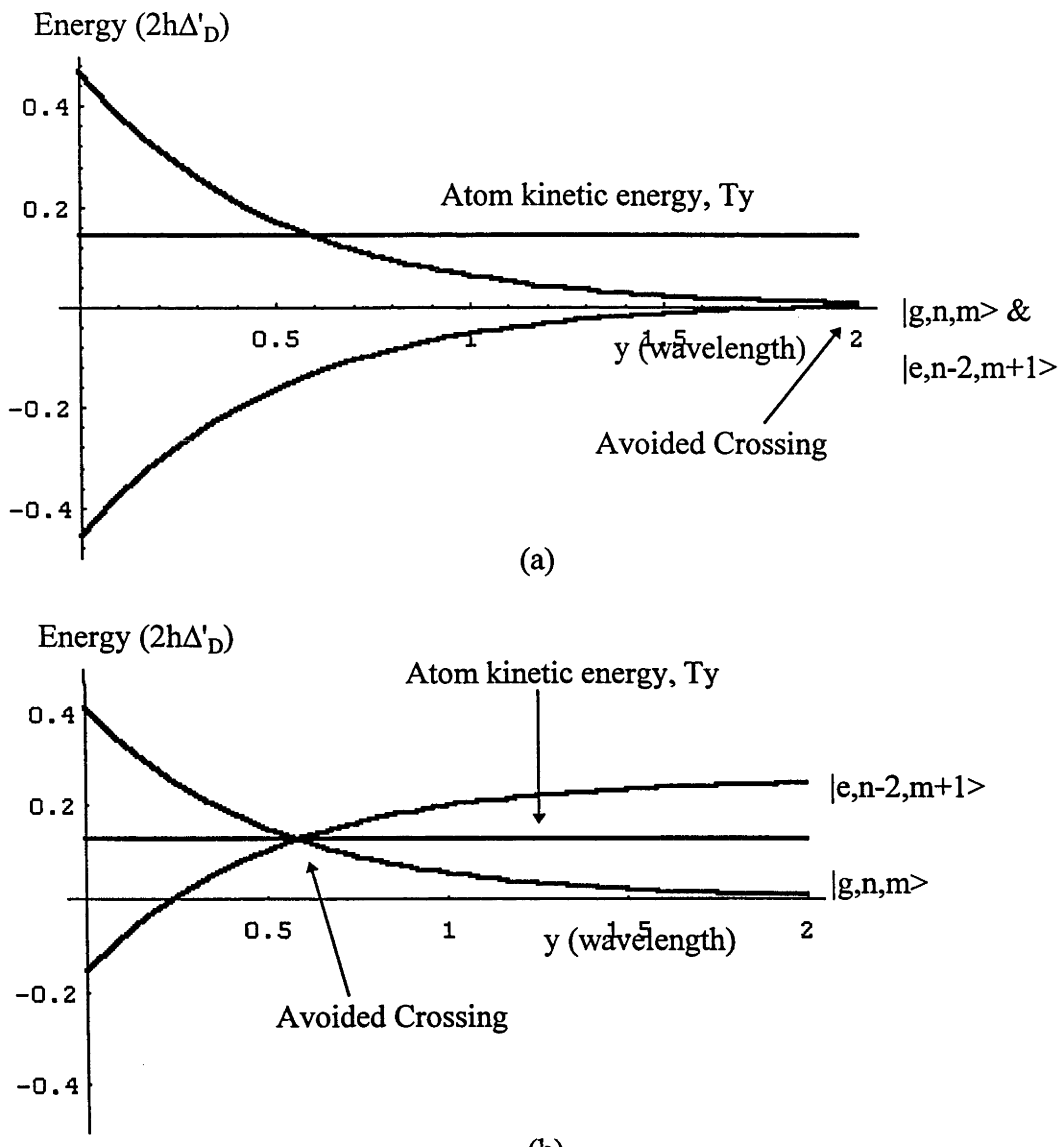

Figure 4.11 : The upper and lower bounds for the interaction of the incident atomic beam with the avoided crossing. (The diabatic potentials are shown) (a) The lower bound for Δ_1 (b) The upper bound for Δ_1. The parameters for the calculation were a saturation paramater $G=3.2\times10^4$, and incidence angle of 2.66mrad, laser 2 detuning of 700MHz and laser 1 detuning of (a) 2.00GHz and (b) 1.84GHz.

Figure 4.7 may be re-examined in light of the correlation between the doppleron resonance condition and the reflection loss mechanism. The n=1 doppleron resonance is the trivial case where one laser field is in resonance with the atom. This resonance is marked by point A in figure 4.7. The laser detuning corresponding to the n=+3 doppleron is marked near point B in figure 4.7, which corresponds to the dip in reflected flux. Another doppleron resonance is expected for n=-3, and is close to the point D in figure 4.7 which locates to the second, broader and shallower, observed resonance.

As the grating velocity is increased to approach the atomic velocity at point C in figure 4.7, the Doppler detuning Δ_D approaches zero. The quasipotential ladder is therefore compressed, creating higher-order doppleron conditions. However, no features corresponding to higher-order doppleron resonances (n>3) were observed.

In summary, the resonant reduction in the reflected flux from a moving evanescent grating may be explained in terms of doppleron resonances. The doppleron resonance conditions coincide with the presence of a quasipotential avoided crossing being energetically accessible for the atom. The experimental parameters which correspond to the n=+3 doppleron resonance conditions were predicted, using the transformed quasipotential model, to be $0 \leq \Delta'-3\Delta'_D \leq 2T_y$.

4.3.5 Experimental Examination of the Doppleron Model

There are a range of conditions over which the doppleron resonances may be expected in the dressed state quasipotential model. The experimental parameters which correspond to the n=+3 doppleron resonance conditions were predicted, using the transformed quasipotential model, to be $0 \leq \Delta'-3\Delta'_D \leq 2T_y$.

The detunings of the experimentally observed resonances were examined to determine whether they fulfilled these conditions over a wide range of experimental conditions.

Atomic beam velocity, angle of incidence and grating velocity were varied, and the results compared with the presented doppleron model. These results are described in this section.

The laser detunings of the doppleron resonances from a series of experimental runs are presented in figure 4.12. The angle of incidence, α, for this series was 2.2mrad. This figure is a plot of laser 2 detuning (velocity of detected atoms) against laser 1 detuning (which governs grating velocity for a given laser 2 detuning). The theoretical bounds for the doppleron condition have been transformed using equations 4.1 to 4.5.

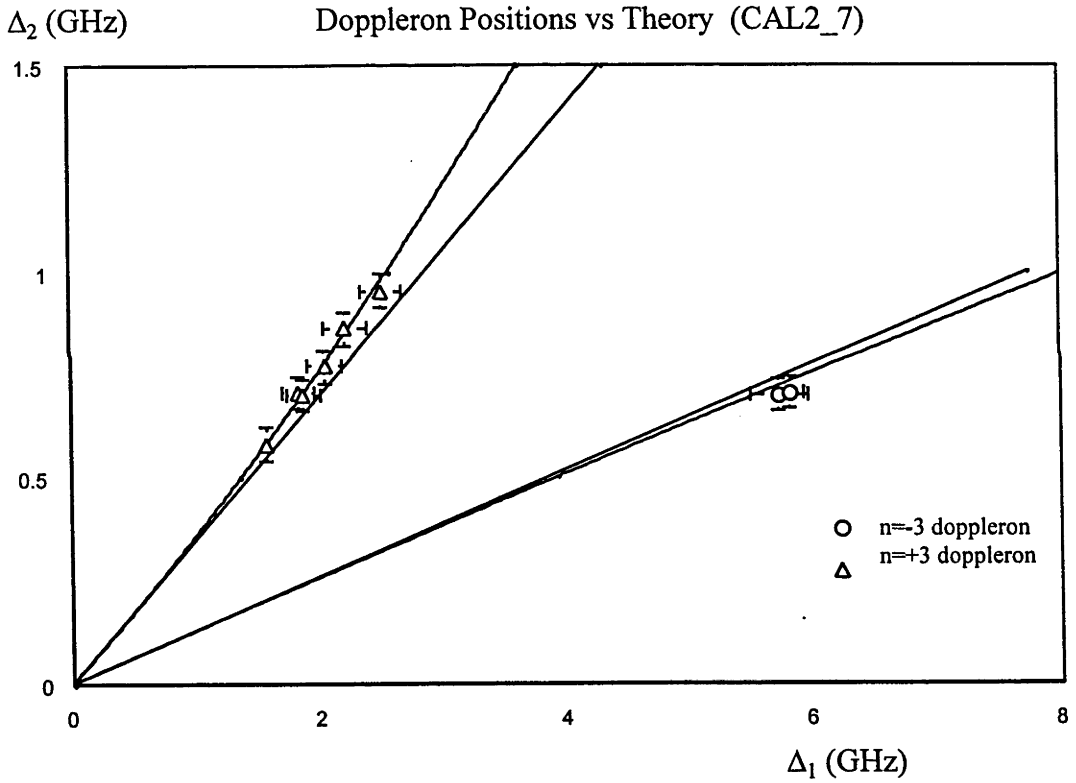

Figure 4.12 : The laser detunings of the doppleron positions are plotted against the theoretical bounds.
The straight lines correspond to the condition $\Delta' = +/- 3\Delta'_D$.
The curved lines correspond to the condition $\Delta' = +/- (3\Delta'_D + 2T_y)$.

There are four theoretical curves in figure 4.12. The upper left pair are the upper and lower bounds for the n=+3 doppleron (i.e. the avoided crossing is energetically accessible between these limits for an atom with kinetic energy T_y). The upper, curved

line corresponds to the condition $\Delta'=3\Delta'_D+2T_y$. It has a parabolic shape as T_y is dependent upon v_a^2, which is proportional to Δ_2^2. The lower, straight line corresponds to the condition $\Delta'=3\Delta'_D$. The positions of the experimental n=+3 doppleron resonances (such as point B in figure 4.7) are marked with triangles. As predicted, the experimental data falls between these upper and lower bounds.

The lower right pair of theoretical curves correspond to the upper and lower bounds for the n=-3 doppleron. The straight line corresponds to the condition $\Delta'=-3\Delta'_D$, while the curved line corresponds to the condition $\Delta'=-3\Delta'_D-2T_y$. The positions of the few recorded n=-3 dopplerons (such as point D in figure 4.7) are marked with circles. The experimental data falls, within the uncertainties, between the two bounds.

The experimental uncertainties, represented by error bars in figure 4.12, are derived from the finite width of both the doppleron resonance and the uncertainty in the laser frequency calibration.

Further data was recorded over a range of incidence angles (from 1.15mrad to 2.34mrad) and atomic velocities (Δ_2 tuned for v_a from $790ms^{-1}$ to $1800ms^{-1}$) . This data is presented in figure 4.13 in four series. The experimentally determined detunings of the n=+3 doppleron resonances in these series are plotted with the corresponding n=+3 doppleron bounds. The scales on all four plots are identical for ease of comparison.

For all of the data presented in figure 4.13, the saturation parameter for lasers 1 and 2 in the evanescent field was $3.8x10^4$.

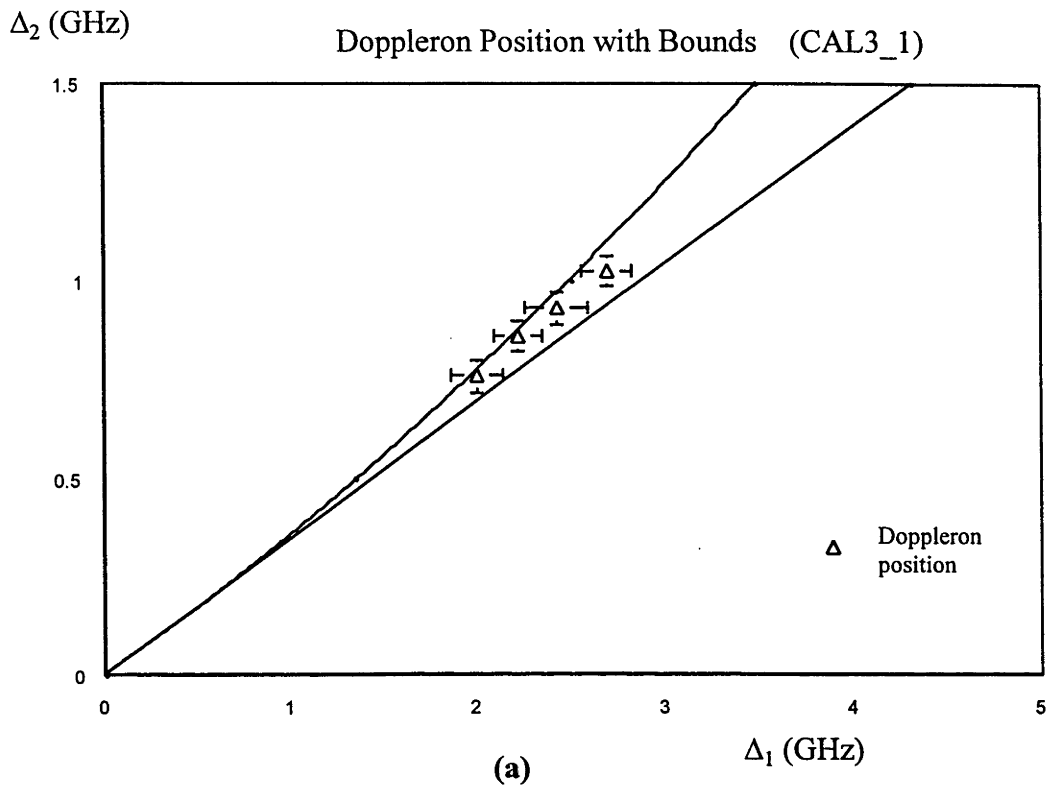
Δ2 (GHz)
Doppleron Position with Bounds (CAL3_1)
1.5
1
0.5
0
0
1
2
3
4
5
Δ1 (GHz)
Δ Doppleron position

(a)

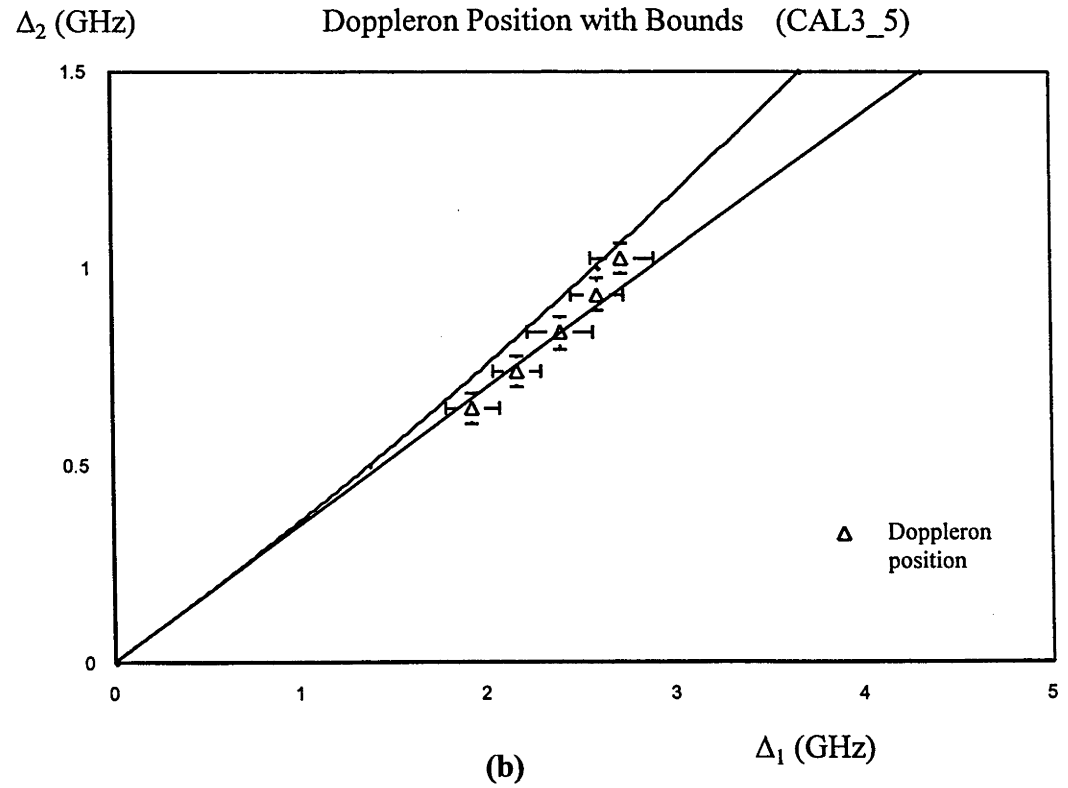
Δ2 (GHz)
Doppleron Position with Bounds (CAL3_5)
1.5
1
0.5
0
0
1
2
3
4
5
Δ1 (GHz)
Δ Doppleron position

(b)

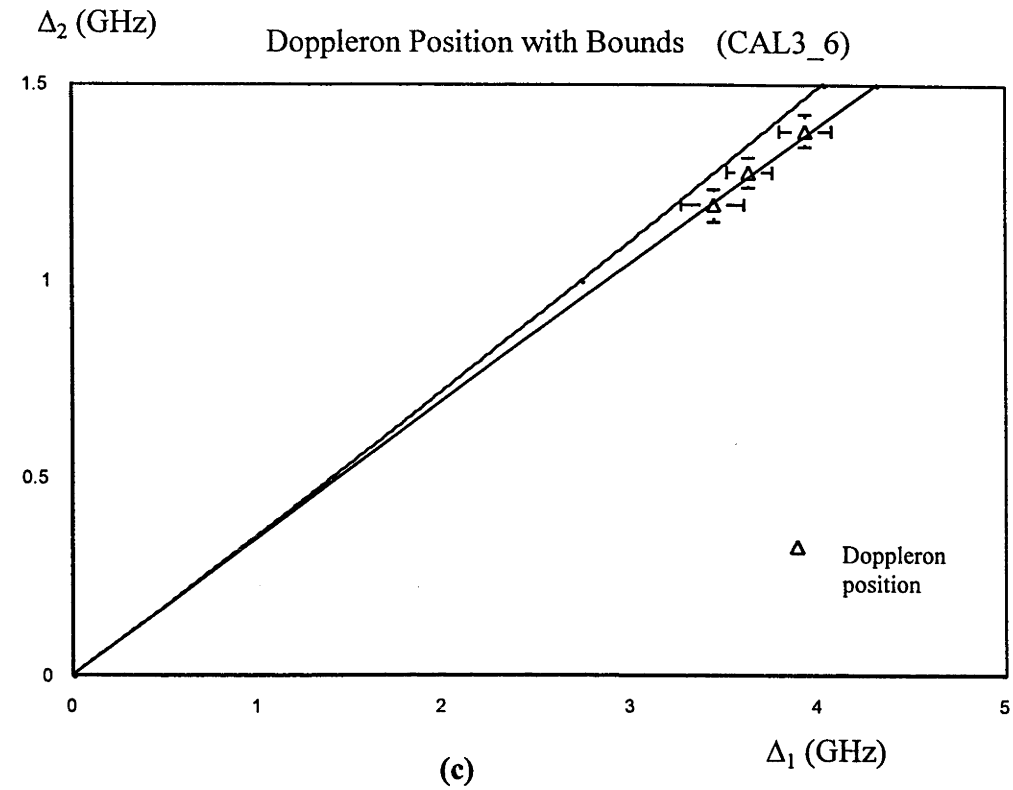

(c)

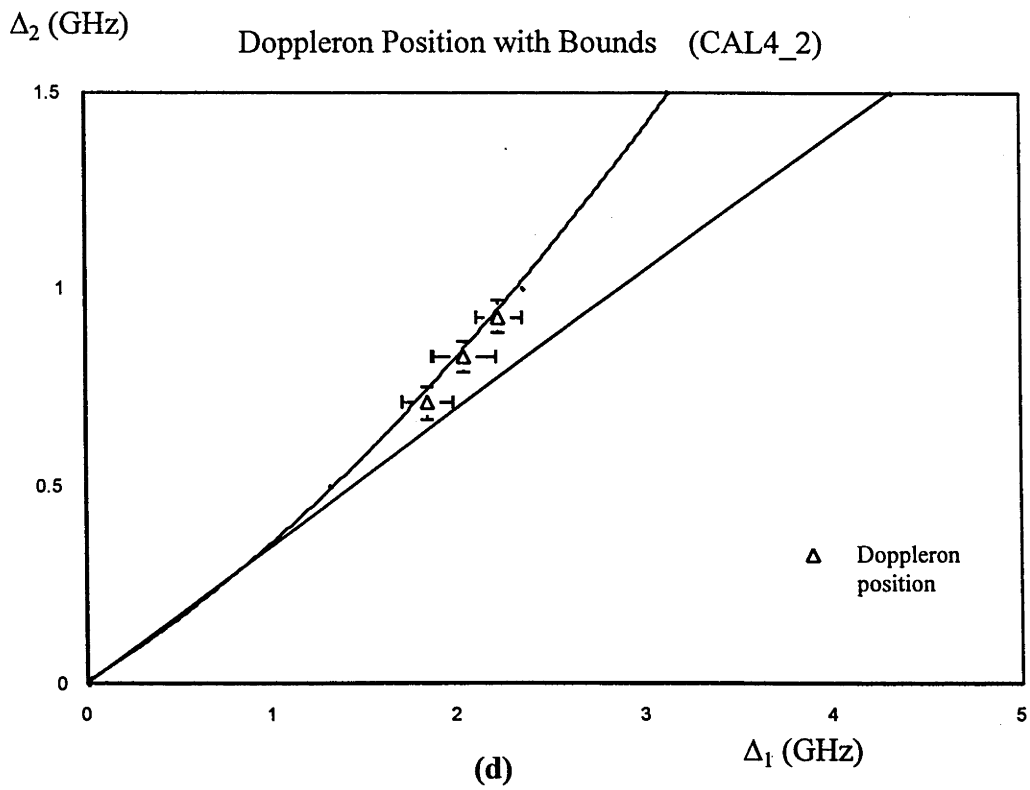

(d)

Figure 4.13 : Doppleron resonance positions plotted with the bounds of accessible avoided crossings. Incidence angles were (a) 2.03mrad (b) 1.72mrad (c) 1.15mrad (d) 2.34 mrad.

In figure 4.13, each series corresponds to a different incidence angle, α. The incidence angles were: (a) 2.03mrad, (b) 1.72mrad, (c) 1.15mrad and (d) 2.34 mrad. Note that for graph (c), where the incidence angle is smallest, the value for T_y is also smallest, and presents the narrowest range of bounds. The graph (c) also contains the highest atomic velocities, as the high velocities could be reflected at shallow incidence angle.

Figures 4.12 and 4.13 indicate that, within the experimental uncertainty indicated by the error bars, the observed doppleron resonance positions do indeed lie between the upper and lower bounds. The results are therefore consistent with the explanation presented in sections 4.3.3 and 4.3.4. It is thus concluded that the incident atomic beam interacts with the quasipotential avoided crossing. This observation confirms the notion of the quasipotential model.

In addition, the interaction of the atomic beam with one avoided crossing provides evidence for the plausibility of several consecutive interactions with avoided crossings; that is, the required interactions necessary for diffraction of the atomic beam from a moving evanescent grating. In a renewed effort to observe diffraction of the thermal sodium atomic beam, a parameter space search was conducted, and is described in the next section.

Note that no significant loss of signal was detected at the conditions corresponding to the n=±5 or higher dopplerons. The n=±5 doppleron condition occurs at a grating velocity much closer to the atomic velocity, and the quasipotential ladder is more compressed in this region. This makes the n=±5 doppleron condition very narrow in frequency space, and much more difficult to detect.

Furthermore, because the n=±5 doppleron represents a higher order non-linear process (5 photon compared with 3 photon for n=±3), the transition probability is less, making the the n=±5 doppleron more difficult to observe. Both characteristics of the n=±5 doppleron, the narrower width and weaker intensity, are predicted by the theory of

Savage et al (1995) (see Fig. 5.1). It is thus likely that the n=±5 dopplerons were not observed due to the magnitude of the experimental noise.

4.4 The Moving Grating Parameter Search

A necessary condition for the observation of diffraction is the presence of multiple avoided crossings in the quasipotential model (Deutschmann et al, 1993) as described in section 2.5. To produce an increased number of avoided crossings, the value for Δ'_D was decreased by increasing the grating velocity to near the detected atomic beam velocity. The diabatic quasipotentials for the condition where Δ'_D is reduced to 480MHz (v_a-v_g=275ms^{-1}) is presented in figure 4.14.

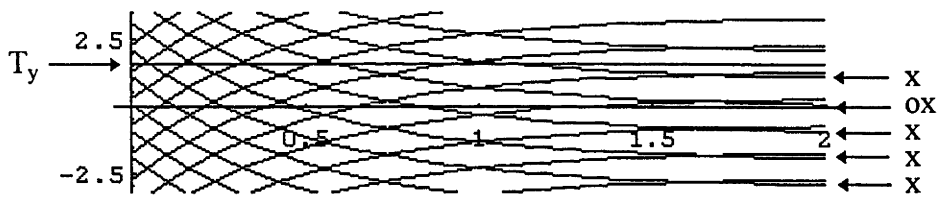

x -Possible output channels
o -Input channel

Figure 4.14 : The diabatic potentials for a grating velocity close to the atomic beam velocity. Energy($2\hbar\Delta'_D$) is plotted against distance (λ). In this case, v_a-v_g=275ms^{-1}. The input channel is denoted o, and some possible output channels are denoted x.

The parameters used in the calculations for figure 4.14 were atomic velocity, v_a=1050ms^{-1}, grating velocity, v_g=775ms^{-1}, and an evanescent field detuning of 2.45GHz. The saturation parameter of the evanescent field in these calculations was G=3.2x10^4.

Figure 4.14 demonstates the compression of the ladder of quasipotentials as the grating velocity approaches the atomic beam velocity. There are many crossings of diabatic potentials in the figure, which correspond to avoided crossings in the adiabatic case. These avoided crossings lead to the possibility of the atoms emerging from the

evanescent grating in a variety of output channels corresponding to diffraction orders (some are marked in the figure).

Note that the energy separation between the output channels in figure 4.14 is smaller than for figure 4.6. The energy separation between adjacent repulsive output channels is equal to $2\Delta'_D$, which is reduced as the grating velocity approaches the atomic beam velocity. The diffraction orders are therefore more closely spaced in energy space under these conditions.

A parameter space search was conducted in an attempt to observe diffraction of the atomic beam. The angle of incidence of the atomic beam on the evanescent grating was α=1.76mrad. This angle was chosen so that the reflected beam profile would be symmetrical and have a good signal to noise ratio (see section 4.12), while being steep enough to allow the observation of doppleron resonances. The detected atomic beam velocity was v_a=1050ms^{-1} (Δ_2=800MHz). The saturation parameters of the laser beams generating the evanescent grating were G=3.8x10^4.

The reduction in the angular separation of diffraction orders as the grating velocity approaches the atomic beam velocity was exploited to minimise the spatial bounds of the parameter space search. A simple kinematic analysis predicts that for an incident angle of 1.76mrad, the diffraction orders should be observable within 0.8mrad of the specular reflection peak for Δ'_D less than approximately 500MHz. The parameter space searched therefore included deflection angles between 3.0mrad and 4.3mrad, where the specular reflection peak was located at 3.5mrad. The detuning of laser 1 ranged from -3GHz to 7GHz in the moving atom frame, which corresponds to a range of grating velocities equal to -500ms^{-1} to 2500ms^{-1}.

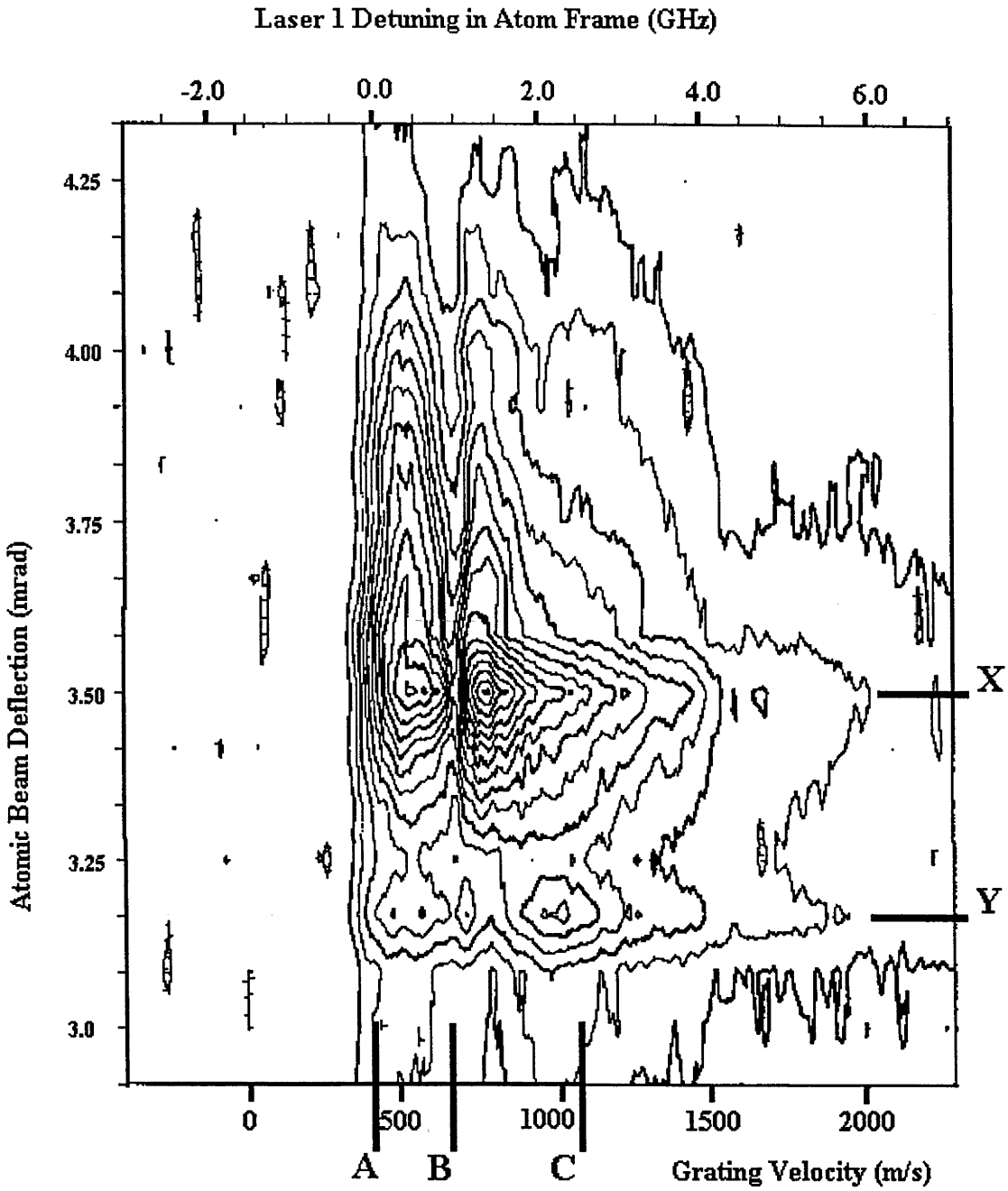

Figure 4.15 : The contour map of reflected flux as a function of deflection angle and laser 1 detuning. A horizontal slice taken at deflection angle X (the specularly reflected peak) is similar to figure 4.7, while a vertical slice taken between points A and B is similar to the specularly reflected peak shown in figure 4.1. The points A,B,C,X and Y are described in the text.

Eighteen frequency scans of laser 1 were recorded at regularly spaced (~0.07mrad) intervals of deflection angle across the reflected beam profile. These scans were compiled into a two dimensional contour map of reflected flux, which is presented in figure 4.15. Each contour represents an increase in reflected flux of 5% of the full scale of the recording device, in arbitrary units. The deflection angle is denoted on the vertical axis and the detuning of laser 1, Δ_1, on the top horizontal axis. As the grating velocity is dependent upon Δ_1 for fixed Δ_2, the horizontal axis also represents grating velocity. An additional equivalent scale has been placed on the bottom horizontal axis denoting the grating velocity, v_g. Note that figure 4.7 is equivalent to a horizontal slice taken through figure 4.15 at the deflection angle marked X (the specularly reflected peak).

The point A marks the frequency at which laser 1 is resonant with the moving atoms ($\Delta_1 = \Delta_D$). When the detuning is negative in the moving atom frame, no reflection is expected from laser 1 alone since its evanescent potential is attractive. The small amount of reflected signal for negative detunings is due to reflection by laser 2.

For positive detunings in the the atom frame, the potential for laser 1 is repulsive. The general behaviour for the reflected signal as a function of positive laser detuning is then similar that described previously (section 4.3.2).

The point B marks the position of the n=+3 doppleron resonance. This resonance position is independent of the deflection angle.

The point C denotes the detuning Δ_1 for which the evanescent grating is moving at the same velocity as the detected atomic beam ($v_g=v_a$). It is at point C that the Doppler detuning Δ'_D goes to zero, and the quasipotential ladder compresses to allow many avoided crossings accessible to the atoms. According to the tranformed quasipotential model, diffraction of the sodium atoms should occur near point C. An example of such a set of quasipotentials is shown in figure 4.14.

No diffraction peaks were observed at deflection angles greater than the specular reflection peak (between 3.50mrad and 4.30mrad) under these conditions. The reflected flux contour map contained a noise of approximately 5% of the reflected peak signal in the region of interest. Therefore, it is concluded that the population of the diffracted atomic beam peaks was less than 5% of the reflected beam peak.

The next stage in the project may have been to model the experimental parameters using the quasipotential model to predict the theoretical population of the diffraction orders. At this stage, however, limitations of the two-level quasipotential model were becoming apparent. The intensity calculations eventually required a full multi-level approach. These developments are discussed in chapter 5.

Another feature of interest, however, was observed at lower deflection angles than the specularly reflected beam peak.

The point X on figure 4.13 represents the peak of the reflection profile. The point Y is located at a shallower deflection angle, and marks the position of a series of 'islands' on the contour map. These 'islands' represent atoms which have been deflected at angles less that the reflection angle, and appear to have a frequency dependence unlike the reflected atoms at the deflection angle marked X. It is concluded that these 'islands' are not simply wings of the reflected peak, but represent a different phenomenon. These frequency dependent deflections are examined more closely in section 4.5.

4.5 Frequency Dependent Deflections

An investigation was made on the frequency dependence of the 'islands' observed in the complete parameter search. Frequency scans of Δ_1 were again recorded at different locations in the reflected beam profile. In addition, deflection angle scans across the reflected beam profile were recorded at differing laser 1 detunings. The results of this investigation are presented in figure 4.16.

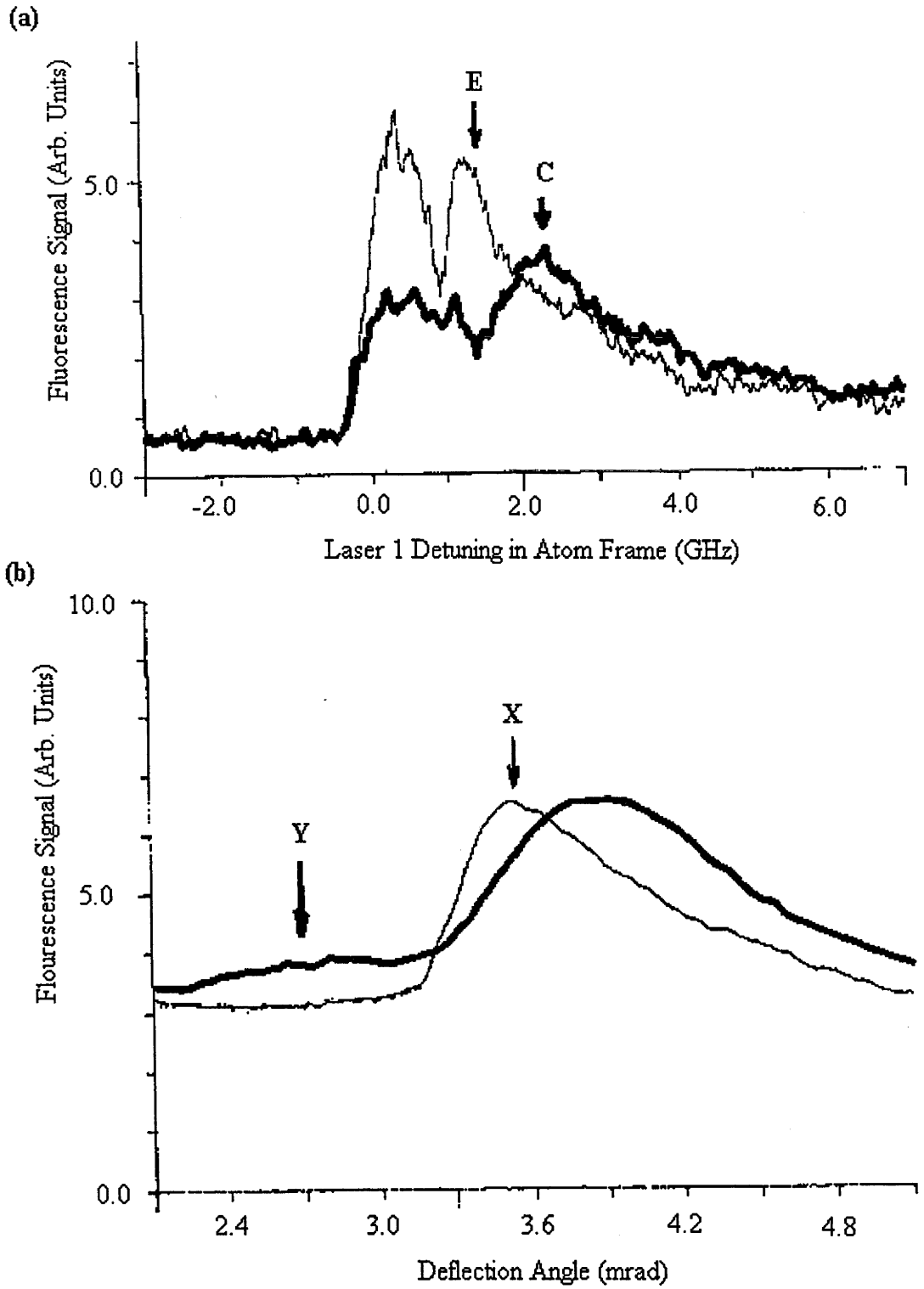

Figure 4.16 : (a) Frequency scans of laser 1 recorded at deflection angles X and Y from figure 4.15. (b) Deflection angle scans recorded at two different laser 1 frequencies corresponding to points E and C in figure 4.16(a).

Figure 4.16 presents two series of traces which were recorded using the same experimental parameters. The velocity of detected atoms was 1088ms^{-1} (Δ_2=+825MHz), and the incidence angle of the atomic mirror was 1.79mrad. The saturation parameter of both evanescent waves was G=3.8x10^4.

Figure 4.16(a) presents two frequency scans which were recorded at different deflection angles on the reflected beam profile. The light trace is the familiar frequency scan taken at the peak of the reflection profile (at position X in figure 4.15 or 4.16 (b)). The heavier trace is a frequency scan recorded for a shallower deflection angle (at point Y in figure 4.15 or 4.16(b)). Note that the heavy trace is 2.5x more sensitive than that for the light trace.

There are significant differences between the two traces in figure 4.16(a). The shape of light trace has been explained in section 4.3. The heavy trace, however, reaches a maximum at the position marked C on figures 4.15 and 4.16(a). This position corresponds to the detuning Δ_1 at which the grating velocity is equal to the atomic velocity.

Figure 4.16(b) presents two reflected beam profiles taken at two different laser 1 detunings. The light trace is the familiar reflection profile (from figure 4.1 and 4.2) taken while laser 1 was tuned to peak reflection flux (at point E in figure 4.16(a)). The heavy trace is a reflection peak profile taken when laser 1 was tuned so that the grating velocity was equal to the atom velocity (at point C in figure 4.15 and 4.16(a)). The scales for the two traces X and Y are identical.

The heavy trace in figure 4.16(b) is a spatial profile of the reflected atomic beam. The plateau at the low deflection angle side of the reflected beam is the feature of interest, and corresponds to the 'islands' in the parameter search (figure 4.15). This plateau occurs at some particular frequencies of laser 1, but comparison with the light trace

shows that at other frequencies of laser 1 it is not present at all. This plateau at point Y is therefore a frequency dependent deflection.

To examine the dependence of the plateau on frequency, the detection system was positioned at point Y and a laser 1 detuning scan was recorded. This frequency scan is the heavy trace in figure 4.16(a). This trace peaks at the point where the grating is moving with the same velocity as the detected atoms. At this point, there are the greatest number of quasipotential avoided crossings energetically accessible to the atoms.

Although there is insufficient data to make any quantitative assessment of the competing process, one possible explanation is proposed here.

Consider the case where the quasipotential positions are similar to those in figure 4.14 (a condition which occurs near the point C). At these conditions, there is a possible output channel (diffraction order) which lies above the input channel. This channel corresponds to lower atomic velocity in the y direction for emerging atoms. Thus, atoms which emerge from the evanescent field in such a channel would be detected at lower deflection angles than specular reflection.

Alternatively, the presence of atoms at deflection angles lower than the specular reflection angle may be explained by the presence of one avoided crossing. As discussed in section 4.3.3 and using figure 4.9, an atom may encounter an avoided crossing during the reflection process as it leaves the evanescent field. If the atom remains in the higher adiabatic potential at the avoided crossing, then it will emerge from the evanescent field in an attractive potential. The time spent in the attractive potential will reduce the kinetic energy of the atom, thus reducing the final deflection angle.

While these explanations are consistent with the features of the heavy traces in figure 4.16, the only firm conclusion which may be drawn at this point is that a frequency

dependent deflection of the atomic beam has been observed for a moving evanescent grating. This deflection has the greatest flux when the velocity of the atomic beam in the moving grating frame is small.

The next stage in the project may have been to model the experimental parameters using the quasipotential model to predict the theoretical population of the diffraction orders. At this stage, however, limitations of the two-level quasipotential model were becoming apparent. Furthermore, the frequency dependent deflections occurred in a region where the quasipotentials were very closely spaced (as in Fig. 4.14).

The modelling of this process was therefore deferred and the development of the multi-level theory is described in section 5.2.

Chapter 5

Conclusion

This project yielded many achievements, both in the development of apparatus and significance of the results. This chapter will review the achievements and provide an insight into the importance of this work in the search for atom diffraction.

5.1 Summary of Major Achievements

There are three major achievements of this project. They were

- the construction of an improved experimental apparatus for the measurement of atomic diffraction and for other atom optics experiments
- the demonstration of a coherent exchange of photons between the two laser fields comprising the moving grating as shown by the observation of doppleron resonances
- the systematic exploration of the parameter space to determine whether diffraction occurs under the experimental conditions used

A number of new theories were developed outside this project to explain the phenomena observed. These theories are discussed further in section 5.2.

Improved Experimental Apparatus

The experimental apparatus used by Hajnal et al (1989) was completely redeveloped in pursuit of the aims of this project. The new system was designed and constructed as part of this project. Improvements to the apparatus included

- an increase in velocity resolution by an order of magnitude to better than 2%

- greater detection sensitivity
- an increase in angular resolution of the deflected atomic beam to better than 0.2mrad
- the generation of a reliable, constant, high flux atomic beam with a reduction of the scattered atoms present in the detection region

Doppleron Resonances in the Moving Grating

An important conceptual advance which was made during the project was the introduction of the moving evanescent grating.

The moving evanescent grating was generated using two counter-propagating laser beams of differing frequency. The quasipotential model (Deutschmann et al, 1993) was transformed into the moving grating frame. This highlighted the compression of the ladder of dressed states, causing avoided crossings to become energetically attainable to the atoms. The atoms interacted coherently with both beams when an avoided crossing was energetically attainable. This was demonstrated by the doppleron resonances observed in the frequency scans of one laser.

The observation of doppleron resonances during the interaction of the atoms with the moving evanescent grating provided verification of the quasipotential model.

Parameter Space Search

The doppleron resonances strongly indicated the possibility of observable diffraction according to the quasipotential model.

A search of the parameter space was conducted. The parameter space search was limited by the availability of only two lasers to provide the two counter-propagating evanescent waves and the detection laser beam. The parameters Δ, v_g and v_a were therefore not independently tuneable in the experiments performed. Kinematic predictions using the quasipotential model identified an experimentally accessible region of parameter space in which diffraction should occur.

Diffraction was not observed in this parameter search. It was concluded that if the diffraction order was present, then it was not well populated (<5% of reflected beam peak). The expected population of the diffraction orders was not calculated because the limitations of the two-level quasipotential model were becoming apparent. The observation of diffraction of metastable neon atoms (Christ et al, 1994), described in section 5.3, could not be modelled using the two-level quasipotential model.

The prediction of the diffraction order intensities using a full multi-level model was left for future projects.

Recommendations

It was recommended that the search for diffraction continue by

- performing the necessary calculations using a multi-level atomic model for the diffraction process from a moving grating
- employing the available experimental parameters in predicting the populations of the diffraction orders
- improving the signal to noise ratio of the experiment by reducing scattered light in the detection chamber
- using three lasers in the experiment to independently select the grating velocity, the grating detuning and the velocity of the detected atomic beam

In the years between September 1993 (end of project) and March 1997 (thesis submission), many of these recommendations have been implemented. The field of atom optics has grown rapidly both within the Australian National University and around the world. Recent work which is relevant to this project is summarised in the following sections.

5.2 Further Theoretical Modelling of Results

This project stimulated a great deal of interest in the field of atomic diffraction. Calculations were motivated by the observations made in this project. These new results provide insight into the experimental results obtained, and so are included in this document.

Doppleron Resonance

The diffracted intensities of sodium atoms by a standing evanescent light wave near the n=3 doppleron resonance were calculated by Murphy et al (1993) using a multi-slice technique. With an atomic velocity of $600ms^{-1}$, a laser detuning of 3.24GHz was selected to produce the n=+3 (asymptotic) doppleron in the quasipotential model. The calculation predicted a sharp dip in the reflected intensity of the specular beam for a detuning slightly below this resonance. Although these calculations were not performed for a moving grating, the theoretical result of a reflection decrease just below the asymptotic doppleron resonance is qualitatively consistent with the experimental results presented in section 4.3.

Modelling of Experimental Conditions

Savage et al (1995) numerically solved the time-dependent Schrodinger equation for a two-level atom interacting with a moving evanescent grating. This model yielded quantitative results for the amplitude and position of the interacting diffraction orders. Typical experimental parameters from this project (reported in chapters 3 and 4) were modelled.

While this model did not predict diffraction for the experimental conditions of this project, the observed doppleron resonances were predicted. Figure 5.1 is taken from Savage et al (1995). The figure was deliberately plotted to be compared directly with figure 2 of Stenlake et al (1994), which is reproduced in this thesis as figure 4.7. Comparison of the theoretical and experimental plots shows striking agreement between

this model and the experimental results observed in this project for the n=+3 and n=-3 dopplerons. The n=+5 and n=-5 dopplerons were not observed experimentally, possibly due to their narrow structure.

The experimental and theoretical observations are also compared numerically in Savage et al (1995). The most striking comparison is the central frequency of the doppleron resonances. For the n=+3 doppleron, the predicted laser 1 detuning is 1.02GHz, compared with the observed position of 0.95GHz. The width of this feature is 0.24GHz (experimentally). For the n=-3 doppleron, the predicted laser 1 detuning is 4.94GHz, compared with the observed position of 4.95GHz. This feature is quite broad, with a width >0.25GHz.

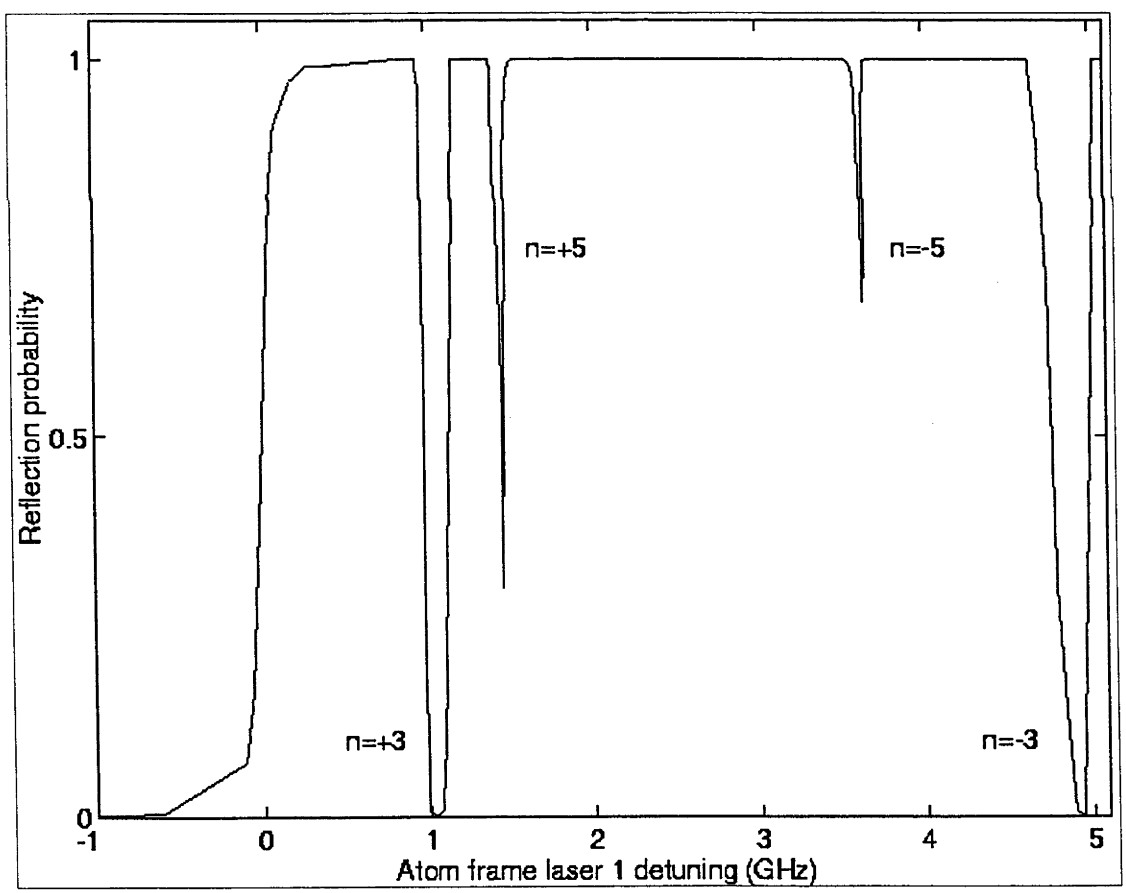

Figure 5.1 : Reflection probability vs laser 1 effective detuning predicted by Savage et al (1995). This figure should be compared to figure 4.7. Taken from Savage et al (1995).

The agreement between this model and the experimental results obtained in this project is striking. This model supports the doppleron explanation for the resonance features presented in section 4.3.

Multi-Level Atom Modelling

Further work by this group (Gordon and Savage, 1996) produced numerical modelling of the diffraction of *multi-level atoms* by an evanescent grating by solving the time-dependent Schrodinger equation. This model was used to explain the observation of diffraction of metastable neon atoms (Christ et al, 1994) which is described in section 5.3. The multi-level solution is an important advance, as the observed diffraction could not be explained using two-level atom models (Savage et al, 1995; Deutschmann et al, 1993).

The multi-level atom model leads to a more complicated structure of quasipotentials. The richer structure of the multi-level theory allows avoided crossings between ground state quasipotentials which are impossible in the two-level theory.

The multi-level model not only explains the atomic diffraction observed (Christ et al, 1994), but also suggests further work. In particular, it predicts a very sensitive dependence of diffraction on the polarisation of the laser beams. For pure s-polarisation (used exclusively in this project), the system was found to be represented by a series of non-interacting, two-level systems and hence predicts no diffraction in this case. The original reason for the use of polarisation parallel to the surface of the quartz block was to produce a uniform polarisation in the evanescent field in order to allow comparison with the theory of Hajnal and Opat (1989).

The key of the multi-level atom model is the existence of avoided crossings between the ground Zeeman states. One transition between these states allows for diffraction into

the n=-2 order (first order) to occur. This transition is extremely sensitive to polarisation, and in particular the model predicts no diffraction for pure s-polarized light. The model suggests that by careful control of the polarisation angle from pure p-polarisation, diffraction efficiencies up to 40% in first order can be achieved.

5.3 Further Experimental Work in the Field

Further investigations of the interaction of neutral atoms with evanescent gratings have been made in recent years. Those most relevant to this project are summarised below.

Observation of Dopplerons

Metastable neon atoms have been reflected from a surface plasmon wave generated using a silvered quartz block (Feron et al, 1992). The enhancement of the intensity of the evanescent wave was around two orders of magnitude, smaller by a factor of 4 than calculations predicted. This enhancement may be less than expected since surface plasmons are scattered by the corrugations of the silver surface.

This experiment also observed doppleron resonances in the reflected metastable beam. It was proposed that the corrugations in the silver surface cause the back-scattering of some surface plasmons. Regions of standing wave are therefore produced. For a given laser detuning and atomic beam velocity, the doppleron condition is met, and has been observed.

Analysis of Mirror Flatness

In 1996, Landragin et al reported careful tests of the conditions required for specular reflection from an atomic mirror. They used trapped rubidium atoms, and dropped them onto a flat atomic mirror. By measuring the spread of the atomic cloud, they drew conclusions about the specular or diffusive nature of the reflection process.

They found that in order for atoms to be reflected perfectly specularly from an atomic mirror, the RMS surface roughness of the underlying optical material (the quartz block), needs to be less than around 0.1nm, or around $\lambda/5000$. This flatness is a great

improvement on the λ/100 quartz block flatness used in the experiments reported in this thesis. Nevertheless, the present reflection observations obeyed the law of reflection sufficiently well for the thermal atomic beam used here to provide useful results.

Diffraction of Cooled Atoms

In 1994, the group which produced the quasipotential model (Deutschmann et al, 1993) reported the first experimental observation of atomic beam diffraction (Christ et al, 1994). A slow metastable neon beam was diffracted by coherent transfer of two photon momenta from an evanescent standing laser field. The atomic beam had a mean velocity of $25ms^{-1}$, and was was transversely compressed to a diameter below 0.15mm and to sub Doppler temperatures. Specular reflection of the atomic beam was observed at deflection angles up to 74mrad, with the first even diffraction order from 81 to 92mrad. The population of the diffracted beam was up to 3% of the reflected beam population.

The two-level atom quasipotential model did not predict diffraction under the experimental conditions used. A multi-level atom model (Gordon and Savage, 1996) was required to model the observations made.

Diffraction of Thermal Atoms

In 1996, the group which observed doppleron resonances in the reflection of metastable neon atoms (Feron et al,1992), reported the first observation of the diffraction of a thermal supersonic beam of metastable atoms by a standing evanescent grating (Brouri et al, 1996).

Brouri et al (1996) overcame the problem of the large quasipotential Doppler shift, Δ_D, by rotating the plane of incident matter waves by 81^o to the evanescent field. Moreover, in order to yield a high AC Stark splitting, the evanescent wave was enhanced by exciting a surface plasmon wave, yielding an 100 fold increase in the intensity of the evanescent wave.

The diffracted atomic beam was observed at a kinematically predicted deflection angle of 7mrad, whereas the reflected beam was observed at an angle of 3.2mrad. The population of the diffracted peak corresponds to 40% of the atoms which interact with the surface plasmon wave. This diffracted peak population is very high, and is yet to be explained.

5.4 Further Work at the Australian National University

The work described in this thesis was limited by cost and time. After this project was completed, a great deal of interest was generated within the Physics Department and the Research School of Physical Sciences. Many atom optics projects have been undertaken within the University, including those which continued the search for diffraction. They are described in this section.

One major limitation of this project was that imposed by having only two lasers to produce the three required laser beams (two evanescent waves plus one detection beam). Work which followed this project sought to overcome this problem by introducing three lasers to the experiment (Snoad, 1993).

The work by Snoad made an attempt to reproduce the doppleron resonances observed in this project. Difficulties arising from maintaining the laser stability and calibration for three independent lasers led to inconsistent results. No diffraction was observed, possibly due to difficulties in laser stability which prevented an extensive parameter search.

The focus of the search for diffraction in this laboratory has since changed to producing diffraction of slow caesium atoms from a standing evanescent grating. Caesium atoms are trapped and cooled, then launched with a (variable) velocity of a few metres per second. Since relatively large (non-grazing) incidence angles can be used, the slow

beam is incident upon a single evanescent grating spot for simplicity. By selecting very small incident velocities, the deBroglie wavelength may be made very large. This will hopefully lead to diffraction of neutral atoms with very large diffraction angles.

References

Adams, C.S., Sigel, M., and Mlynek, J. (1994). *Physics Reports* **240**, 143 - 210.

Anderson, A., Haroche, S., Hinds, E. A., Jhe, W., Meschede, D., and Moi, L. (1986). *Phys. Rev. A*, **34** (4), 3513-3516.

Ashkin, A. (1970). *Phys. Rev. Lett.* **25**, 1321.

Aspect, A., Arimondo, E, Kaiser, R., Vansteenkiste, N., and Cohen-Tannoudji, C. (1988). *Physical Review Letters* **61** (7), 826-829.

Baldwin, K.G.H., Hajnal, J.V., Fisk, P.T.H. and Bachor, H.A. (1988) "Preliminary Investigations into the Reflection and Diffraction of Sodium Atoms by an Evanescent Standing Wave Laser Light Field", *Laser Physics Centre Internal Report* (Australian National University).

Baldwin, K.G.H., Hajnal, J.V., Fisk, P.T.H., Bachor, H.-A., and Opat, G.I. (1990). *J. Mod. Opt.* **37** (11), 1839-1848.

Balykin, V.I., Letokhov, V.S., Ovchinnikov, Yu. B., and Sidorov, A.I. (1987) *Pis'ma Zh. Eksp. Teor. Fiz.* **45** (6), 282-284.

Balykin, V.I., Letokhov, V.S., Ovchinnikov, Yu. B., and Sidorov, A.I. (1987) *JETP Lett.* **45**, p.353.

Balykin, V.I., Letokhov, V.S., Ovchinnikov, Yu. B., and Sidorov, A.I. (1988). *Phys. Rev. Lett.* **60** (21), 2137-2140.

Balykin, V. I., and Letokhov, V.S. (1989). *Appl. Phys.* B **48**, 517-523.

Balykin, V.I., and Letokhov, V.S. (1989a). *Physics Today* **42** (4), 23-28.

Balykin, V. I., and Letokhov, V.S. (1995). 'Atom Optics with Laser Light', Harwood Academic.

Bjorkholm, J. E., Freeman, R. E., Ashkin, A., and Pearson, D. B. (1978). *Phys. Rev. Lett.* **41**, (20) 1361-1364.

Brouri., R., Asimov, R., Gorlicki, M., Feron, S., Reinhardt, J., Lorent, V., and Haberland, H. (1996). *Optical Communications* **124**, 448-451.

CRC (Chemical Rubber Company) (1975) "CRC Handbook of Materials Science" (Cleveland)

Christ, M., Scholz, A., Schiffer, M., Deutschmann, R., Ertmer, W. (1994). *Optics Communications* **107**, 211-217.

Cohen-Tannoudji, C. (1977) "Quantum Mechanics" (J. Wiley, New York)

Cohen-Tannoudji, C. (1991) "*Fundamental Systems in Quantum Optics*" (Elsevier Science Publ., B.V.)

Cook, R.J. (1979). *Phys. Rev. A* **20**, 224-228.

Cook, R.J., and Hill, R.K. (1982). *Opt. Commun.* **43**, p.258.

Dalibard, J. and Cohen-Tannoudji, C. (1985) *JOSA B* **2**, 1707-1720

Deutschmann, R., Ertmer, W., and Wallis, H. (1993). *Phys. Rev. A* **47** (3), 2169-2185.

Dowling, J.P. and Gea-Banacloche, J. (1996). *Adv. At. Mol. Opt. Phys.* **37**, 1-94.

Einstein, A. (1909) *Phys. Zs.* **10**,185

Feron, S., Reinhardt, J., Le Boiteux, S., Gorceix, O., Baudon, J., Ducloy, M., Robert, J., Miniatura, Ch., Chormaic, S. Nic, Haberland, H., and Lorent, V. (1993). *Opt. Commun.* **102**(1,2), 83-88.

Feron, S., Reinhardt, J., Ducloy, M., Gorceix, O., Chormaic, S. Nic, Miniatura, Ch., Robert, J., Baudon, J., Lorent, V., and Haberland, H. (1994). *Physical Review A,* **49**, 4733-4741.

Gordon, D., Savage, C.M. (1996). *Opt. Commun.* **130**, 34. (Erratum **136**, 503 (1997))

Gordon, J.P. and Ashkin, A. (1980). *Physical Review A.* **21** (5), 1606-1617.

Gould, P.L., Ruff, G.A., and Pritchard, D.E. (1986). *Phys. Rev. Lett.* **56** (8), 827-830.

Hajnal, J.V. and Opat, G.I. (1989). *Opt. Commun.* **71** (3,4), 119-124.

Hajnal, J.V., Baldwin, K.G.H., Fisk, P.T.H., Bachor, H.-A., and Opat, G.I. (1989a). *Opt. Commun.*, **73** (5), 331-336.

Haken, H. and Wolf, H.C. (1987) "Atomic and Quantum Physics" 2nd ed., Springer-Verlag

Jackson, J.D. (1975) "Classical Electrodynamics" 2nd Ed. (Wiley & Sons, New York).

Kaiser, R., Lévy, Y., Vansteenkiste, N., Aspect, A., Seifert, W., Leipold, D., and Mlynek, J. (1994). *Opt. Commun.* **104**, 234-240

Kasevich, M. A., Weiss, D. S., and Chu, S. (1990). *Opt. Lett.* **15** (11), 607-609.

Keith, D. W., Schattenburg, M. L., Smith, H. I., and Pritchard, D. E. (1988). *Phys. Rev. Lett.* **61** (14) 1580-1583.

Landragin, A., Labeyrie, G., Henkel, C., Kaiser, R., Vansteenkiste, N., Westbrook, C. I., and Aspect, A., (1996), *Optics Letters*, **21**, 1591

Levenson, M.D and Kano, S.S, (1988) "Introduction to Nonlinear Laser Spectroscopy", Revised Edition, Academic Press

Li, Qiming (1994) "The Investigation of the Interaction of a Sodium Atomic Beam with a Strong Standing Wave Laser Field", PhD Thesis, Australian National University.

Li, Qiming, Stenlake, B.W., Littler, I.C.M., Bachor, H.-A., Baldwin, K.G.H., and McClelland, D.E. (1994). *Laser Physics 4* (5), 983 - 994.

Manson, P.J., (1987) "An Investigation of a Strongly Driven Multi-Level Atomic System", PhD Thesis, Australian National University.

Martin, P.J., Oldaker, B.G., Miklich, A.H., and Pritchard, D.E. (1988). *Phys. Rev. Lett.* **60** (6), 515-518.

Moore, J.H, Davis, C.C, Coplan, M.A. (1989) "Building Scientific Apparatus - A Practical Guide to Design and Construction" (Addison-Wesley)

Murphy, J.E, Goodman, P., Smith, A. (1993), *J Phys.: Condensed Matter*, **5**, 4665-4676

Murphy, J.E., Hollenberg, L.C.L., Smith, A.E. (1994) *Phys. Rev. A*, **49**, 3100.

Savage, C. M. (1996) *Australian Journal of Physics*, **49**, 745-764.

Savage, C. M., Gordon, D., and Ralph, T. C. (1995). *Phys. Rev. A.* **52** (6), 4741.

Shen, Y.R. (1984) "The Principles of Non-Linear Optics" (Wiley)

Snoad, N (1993) "Atomic Reflection and Multiple Photon Processes in an Evanescent Laser Light Field", *Honours Thesis*, Australian National University.

Stenlake, B.W., Littler, I.C.M., Bachor, H.-A., Baldwin, K.G.H., and Fisk, P.T.H. (1994). *Phys. Rev. A.* **49** (1), R16 - 19.

Thorne, A.P. (1974) "Spectrophysics" (Chapman and Hall)

Wallis, H. (1993) *Private communication.*

Wei, C., Manson, N.B., and Martin, P.D. (1995). *Phys. Rev. A* **51** (2), 1438-1445.

Wei, C. (1997) *Private communication.*

Weissbluth, M. (1989) "Photon-Atom Interactions" (Academic Press, London).

Appendix A

Significant Publications

This appendix contains two journal papers which were produced as a result of the work performed during the course of the PhD project.

Stenlake et al (1994) is a summary of the major results obtained in this project. My contribution to this work included the design and construction of the experimental apparatus, the performance of experimental runs, the development of the transformed quasipotential model and the explanation of the results in terms of this model.

Li et al (1994) contains a summary of the work of a fellow student, Qiming Li. My contribution to this work was limited to the construction of the experimental apparatus, configuration of the experiment for Qiming's needs and occasional assistance during experimental runs.

PHYSICAL REVIEW A VOLUME 49, NUMBER 1 JANUARY 1994

Observation of velocity-tuned resonances in the reflection of atoms from an evanescent light grating

B. W. Stenlake, I. C. M. Littler, H.-A. Bachor, and K. G. H. Baldwin
Laser Physics Centre, Australian National University, Canberra, Australian Capital Territory 0200, Australia

P. T. H. Fisk
Division of Applied Physics, Commonwealth Scientific and Industrial Research Organization, Lindfield, New South Wales 2070, Australia

(Received 3 May 1993)

We report on the observation of velocity-tuned (doppleron) resonances in the grazing-incidence reflection of thermal sodium atoms from a moving evanescent light grating created by interference between two counterpropagating laser beams. The relative velocity between the atoms and the grating can be varied continuously by adjusting the frequency of one laser. We observe an exchange of photons between copropagating and counterpropagating fields in an evanescent light grating. The results are in general agreement with a dressed-state model for the diffraction of atoms from such a grating.

PACS number(s): 32.80.Pj, 42.50.−p

An important goal in atomic optics is the creation of a large-angle beam splitter, since for many applications of atomic interferometers the sensitivity depends on the area enclosed by the two arms. Interferometers have been realized using material microstructures [1] and also by employing the coherent exchange of a pair of photons [2].

Mechanisms utilizing stimulated light forces with the exchange of multiple photon momenta ($\hbar k$) have shown promise for the creation of large-angle splitters. Experiments employing the optical Stern-Gerlach effect [3], the stimulated magneto-optic effect [4], and standing-wave transmission light gratings [5] have demonstrated transfer of multiple photon momenta. Splittings of up to $40\hbar k$ have been observed [6]. However, a large angular separation of the partial waves was not achieved by these techniques, either because the de Broglie wavelength was significantly less than the structure size, or because the photon momentum transfer perpendicular to the atomic beam was small compared to the atomic momentum.

An alternative approach for generating large separation angles was suggested by Hajnal and Opat [7] who proposed an atomic reflection grating. They extended the atomic mirror concept of Cook and Hill [8] based on a positively detuned evanescent light field by suggesting the use of a standing-wave interference pattern created by two identical, counterpropagating laser beams totally internally reflected at a dielectric surface. If used at grazing incidence, this reflection grating would magnify the angular separation of the diffracted orders by reducing the effective grating spacing to the order of the de Broglie wavelength.

An early investigation in this laboratory into the properties of such a reflection grating demonstrated specular reflection of atoms from both traveling and standing evanescent waves [9]. However, there was no direct evidence for diffraction of atomic de Broglie waves from the standing-wave field.

Recently, simulations by Deutschmann, Ertmer, and Wallis [10] using a dressed-state approach have shown that diffraction is possible, but under a different set of experimental parameters. Essentially, if there is to be significant interaction of the atom with both laser light fields, then the Rabi frequency must be much larger than the Doppler shift in both the copropagating and counterpropagating laser fields. This is a difficult criterion to satisfy using thermal atoms for which the Doppler shift is large, because the light intensity available in cw dye laser experiments is limited. Consequently, it would appear necessary to decelerate the atoms in order to observe diffraction.

Our approach to this problem was different: rather than slow the atoms, we created a moving grating by using two counterpropagating lasers of different frequency. The velocity v_g of the grating in the direction of the atoms is given by

$$v_g=(\Delta_1-\Delta_2)/2Q\ , \tag{1}$$

where Δ_1 and Δ_2 are the respective detunings (referred to a stationary atom) of the lasers which copropagate and counterpropagate with the atomic beam. The wave vector of the evanescent traveling wave parallel to the surface is $Q=n\sin\theta/\lambda$, where n is the refractive index of the quartz block, θ is the angle of incidence of the laser beam, and $\lambda\sim\lambda_1\sim\lambda_2$.

A transformation of the laser frequencies and atomic velocities to the frame moving with the grating is then performed:

$$\Delta'_D=(2\Delta_D-\Delta_1+\Delta_2)/2\ , \tag{2}$$

$$\Delta'=(\Delta_1+\Delta_2)/2\ . \tag{3}$$

Here Δ_D is the Doppler shift in the laboratory frame due to the moving atom. In the moving grating frame (primed parameters), both laser fields have the same frequency. Thus the problem is once again reduced to the interaction of an atom (Doppler shift Δ'_D) with a standing wave detuned Δ' from resonance.

The experimental arrangement is shown in Fig. 1. A sodium atomic beam was produced by an oven at a tem-

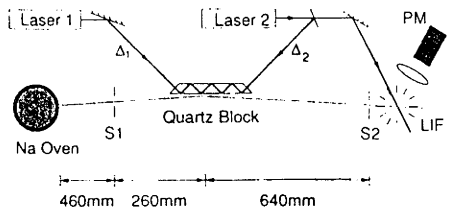

FIG. 1. Experimental schematic: the detuning of laser 1 (Δ_1) is varied to change the grating velocity. The detuning of laser 2 (Δ_2) is set to detect a specific atomic velocity group. LIF, laser induced fluorescence; PM, photomultiplier; $S1$, 40-μm slit; $S2$, 100-μm slit.

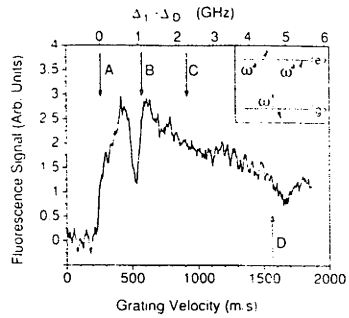

FIG. 2. Fluorescence signal due to specularly reflected atoms traveling at 910 m/s and incident at an angle of 2.5 mrad. Here Δ_2 was fixed at $+700$ MHz, while Δ_1 was varied (upper horizontal scale): A, laser 1 resonant with moving atoms ($\Delta_1=\Delta_D$); B and D, doppleron resonances in the grating frame, i.e., $\Delta'=+3\Delta'_D$ and $\Delta'=-3\Delta'_D$; C, grating velocity equal to atomic velocity (equivalent to $n=\infty$ or $\Delta'_D=0$). The lower horizontal scale shows the grating velocity ($\alpha\{\Delta_1-\Delta_2\}$). Inset: energy-level scheme for $\Delta'=+3\Delta'_D$, where ω_1^g/ω_1^c are the copropagating and counterpropagating frequencies in the atom frame.

perature of 500 °C and with a nozzle diameter of 0.4 mm. The evanescent laser field was produced at the surface of a fused silica block 25 mm long, 6 mm wide and 375 μm thick with the end faces beveled at 45° [9]. The laser beams were totally internally reflected from the quartz/vacuum interfaces at both front and back surfaces. Contiguous multiple reflections of the laser beam were thus created, forming an almost continuous evanescent light field 400 μm high. In this fashion, the full 25-mm length of the block was used to increase the number of atoms interacting with the grating.

Two ring dye lasers (Coherent 699-21, Spectraphysics 380D) were used to generate the evanescent light grating. Both were linearly polarized parallel to the quartz block surface. The detuning of the copropagating laser beam (Δ_1) could be varied to change the speed of the grating. However, the detuning of the counterpropagating laser beam (Δ_2) was held constant, since this laser was also used to detect the atoms via Doppler-tuned (and hence velocity-resolved) laser-induced fluorescence (LIF). The intensity at the surface of the quartz block for laser 1 was ≈ 500 W/cm^2, while that for laser 2 was approximately half that value.

The detection laser was incident at an angle of 63° to the atomic beam. The detection laser was tuned to the transition between the $3S_{1/2}(F=2)$ hyperfine ground state and an excited state. The LIF produced as the atoms decayed into both the $3S_{1/2}(F=2)$ and $3S_{1/2}(F=1)$ states was imaged onto a photomultiplier, thereby measuring the number of atoms in the $F=2$ state. Strictly speaking, there are three accessible upper hyperfine levels, but the fluorescence signal was dominated by the $F=2\rightarrow 3$ transition. The velocity selectivity of this system was ± 5 m/s, limited by the atomic linewidth of 10 MHz. Laser 1 was crossed perpendicular to the atomic beam to yield a Doppler-free frequency calibration accurate to within the atomic linewidth. The frequency of the detection laser was determined by measuring the beat frequency with laser 1. An étalon of 1.5 GHz free spectral range was used to calibrate the frequency scale.

Figure 2 shows an experimental trace for 910 m/s atoms incident at a grazing angle of 2.5 mrad to the quartz block. The detection signal due to atoms at the peak of the specularly reflected beam is plotted as a function of laser 1 detuning. The detuning of laser 1 is given by the top horizontal scale, which commences at the left-hand side when the two laser frequencies are equal ($\Delta_1=\Delta_2$).

The frequency of laser 2 is held constant at $\Delta_2=+700$ MHz (which is equivalent to $+2.3$ GHz in the atom frame, yielding a repulsive potential). The frequency difference between the two lasers is equivalent to the velocity of the evanescent grating [Eq. (1)], which is shown on the bottom horizontal scale.

The zero point on the top scale (point A) marks the frequency at which laser 1 is resonant with the moving atoms ($\Delta_1=\Delta_D$). When the detuning is negative (to the left of point A) in the moving atom frame, no reflection is expected from laser 1 alone since its evanescent potential is attractive. The small amount of reflected signal for negative detunings is due to reflection by laser 2. Note that the reflected signal depends on the area of the grating that experiences an intensity exceeding the value needed to repel atoms of a selected velocity. For this reason, the reflected signal due to laser 2 alone (i.e., with laser 1 blocked) is smaller (≈ 0.5 on the scale shown in the diagram).

For positive detunings in the atom frame (to the right of point A), the potential for laser 1 is also repulsive. The general behavior of the reflected signal as a function of positive laser detuning is then similar to the evanescent mirror experiments conducted previously [9].

However, in this moving grating experiment, a resonant decrease in the reflected flux is observed near point B in Fig. 2 for a particular value of Δ_1, i.e., for a particular grating velocity. A second (smaller) resonance is located near point D in Fig. 2. The resonances disappear in the absence of either laser, or upon misalignment of the overlap between the two lasers on the surface of the quartz block. Hence the resonances are not the result of a single photon process, such as optical pumping from the $F=2$ state to the $F=1$ state. The data indicate that the resonances are due to the coherent exchange of photons between the two lasers.

The decrease in the reflected flux can be explained in terms of doppleron resonances [11], which have previously been observed in the enhancement of stimulated light forces acting on atoms in standing-wave light fields [12]. Doppleron resonances correspond to exchanges (through successive coherent absorption and stimulated emission processes) of photons between the two counterpropagating fields comprising the standing wave (Fig. 2 inset). The resonances occur at laser detunings (in the grating frame) given by

$$\Delta' = \pm n\Delta'_D + \Delta_L \quad (n \text{ odd}) . \tag{4}$$

The quantity Δ_L is the light shift, and is of the order of the Rabi frequency at the distance from the quartz surface where the photon exchanges are taking place.

The $n=1$ doppleron resonance is trivial, since it corresponds to the case where one laser field is resonant in the atom frame. The laser detuning corresponding to the $n=3$ doppleron resonance is marked (with $\Delta_L=0$) by point B in Fig. 2, and is close to the observed sharp decrease in reflectivity. Another doppleron resonance is expected for $n=-3$, and is marked by point D, which is close to the second (smaller) observed resonance. No features corresponding to higher-order doppleron resonances ($n>3$) could be discerned from the experimental data.

The $n=3$ doppleron resonance corresponds to an exchange of photons between the fields, followed by an absorption that leaves the atom in the excited state. Such atoms experience an attractive potential and are accelerated towards the quartz block where they are lost, thereby causing the reduction in reflectivity.

In order to account exactly for the difference between the observed resonances and the condition $\Delta'=\pm 3\Delta'_D$, a model is required that predicts the distance from the quartz surface (and hence the light shift) at which the photon exchange occurs. A comprehensive model was presented by Deutschmann, Ertmer, and Wallis [10] to predict conditions for atomic diffraction from an evanescent grating. The positions in frequency space of our observed doppleron resonances are entirely consistent with this model, for which we present a brief description.

Under the model presented by Deutschmann, Ertmer, and Wallis, de Broglie waves propagate under the influence of quasipotentials of the dressed atomic states. Figure 3 shows the quasipotentials for experimental parameters at the resonance (near point B in Fig. 2), plotted as a function of distance from the surface of the quartz block. The solid horizontal line is the kinetic energy of the atom perpendicular to the substrate surface.

We will concern ourselves firstly with the behavior of the quasipotentials at large z, i.e., in the low field region. Here, each dressed state corresponds to a particular number of photon exchanges (absorption or stimulated emission) experienced by the incoming ground-state atom with the two fields. Each dressed state therefore represents a particular diffraction order at large z. There are two families of dressed states: (a) the dotted lines in Fig. 3 which are formed by exchanging even numbers of photons with the incident ground-state atom, and (b) the dashed lines which involve an odd number of photon interactions. At large z, the dotted curves correspond to the ground state, while the dashed curves correspond to the excited state. The spacing between members of the same family is equal to twice the Doppler shift ($2\Delta'_D$). In addition, since the dashed states result from the exchange of an odd number of photons at large z, their energy is detuning dependent, which shifts the dashed states relative to the dotted states.

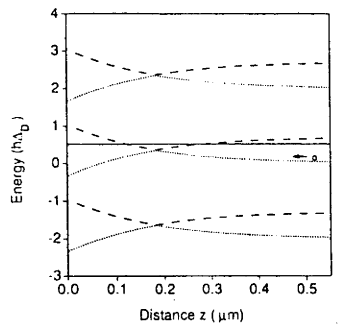

FIG. 3. Quasipotentials for the dressed states of the system for the present experimental conditions as a function of distance from the quartz block. The potentials represented by the dotted and dashed curves correspond, respectively, to the ground and excited states at large z. The bold line gives the kinetic energy of the atom perpendicular to the surface. Note that under these conditions an avoided crossing occurs at only one z position, near which a transition to the neighboring potential is most likely.

As the quartz block is approached, the field intensity increases, the character of the dressed states changes and becomes mixed, and the quasipotentials are ac Stark shifted. For a positive detuning, the energy of the dotted states shifts higher while the energy of the dashed states shifts lower. As the field intensity becomes large, the oppositely shifted potentials may approach and form an avoided crossing where they repel each other. At these points the atom is most likely to move diabatically from one potential to the other. In fact, this is a necessary condition for diffraction to occur [10], since it is by this means that the atoms transfer between the dressed states, each of which represents a particular diffraction order.

For the conditions of the present experiment, only one avoided crossing is accessible to an incoming ground-state atom (Fig. 3). Thus, the incoming de Broglie wave can be coherently split into only two possible output channels: (1) it may emerge at large z in the ground state, i.e., as a specularly reflected atom, or (2) it may be attracted to the quartz surface and lost. In the case shown in Fig. 3, the atom cannot emerge in the excited state at large z (dashed curve) since it does not have the required kinetic energy. However, since channel 2 is accessible, a decrease in the grating reflectivity will be observed.

In the present experiment, since the kinetic energy is much less than the separation of the dressed states of one family ($2\Delta'_D$), channel 2 will be open when the two families of quasipotentials are nearly degenerate at large z. Exact degeneracy of these states occurs when the detuning satisfies $\Delta'=n\Delta'_D$, where n is odd. This condition is again the definition of the doppleron resonance [11].

Figure 4 shows the grating velocity corresponding to the observed reflection resonances for various values of the atomic velocity. If the relationship $\Delta' = 3\Delta'_D$ is transformed into the laboratory frame and expressed in terms of atomic and grating velocities, line *A* in Fig. 4 is obtained. The sharp experimental resonances lie close to but slightly above this line, corresponding to the offset of the resonances from point *B* in Fig. 2.

The straight lines in Fig. 4 give the doppleron condition in the field-free region. However, the small but finite kinetic energy of the atom normal to the surface enables access to the avoided crossings produced by the light shift when the detuning is slightly offset from the degeneracy condition, $\Delta' = \pm 3\Delta'_D$. The offset of the data points from line *A* in Fig. 4 is consistent with the perpendicular kinetic energies obtained in this experiment.

The negative doppleron resonance $\Delta' = -3\Delta'_D$ is shown by line *B* in Fig. 4, along with experimental resonances for several atomic velocities. It is difficult to obtain reliable experimental data for this condition, which corresponds to a very large detuning of the copropagating laser and hence to a small reflection signal. The negative resonances, as expected, lie close to but below line *B*. This is again due to the small but finite kinetic energy of the atom perpendicular to the surface.

Finally, the observed resonances do not correspond to two-photon Raman transitions between the ground-state hyperfine components, which could lead to loss of atoms in the detected $F = 2$ state. In Fig. 4, such transitions would lie on two lines of unity slope intersecting the horizontal axis at velocities of ± 506 m/s.

In conclusion, we have observed doppleron resonances in the reflection of atoms from a moving evanescent grating. This is the first evidence for a coherent exchange of photons between two counterpropagating evanescent light fields. These results also provide the first experimental verification for a model which predicts diffraction from an evanescent atomic reflection grating [10]. Using different experimental parameters to create a favorable sequence of multiple avoided crossings, diffraction may be expected to occur. Such a reflection grating could then be used as a large-angle beam splitter for atomic de Broglie waves.

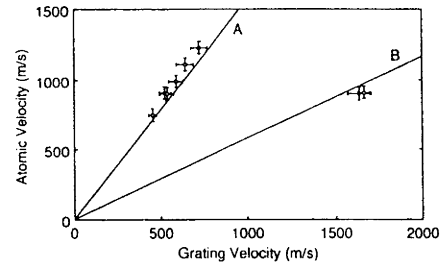

FIG. 4. Grating velocity at which the observed resonances occur for various atomic velocities using a grazing-incidence angle of 2.5 mrad. The lines describe the doppleron resonances: *A*, $\Delta' = 3\Delta'_D$; *B*, $\Delta' = -3\Delta'_D$. The horizontal error bars correspond to the width of the observed resonances.

We gratefully acknowledge the skilled assistance of B. Brown. We thank A. Stevenson, D. E. McClelland, and H. Wallis for helpful and stimulating discussions. This work was supported by the Australian Research Council.

[1] D. W. Keith, C. R. Ekstrom, Q. A. Turchette, and D. E. Pritchard, Phys. Rev. Lett. **66**, 2693 (1991); O. Carnal and J. Mlynek, *ibid.* **66**, 2689 (1991); F. Shimizu, K. Shimizu, and H. Takuma, Phys. Rev. A **46**, R17 (1992).

[2] F. Riehle, Th. Kisters, A. Witte, J. Helmcke, and Ch. J. Bordé, Phys. Rev. Lett. **67**, 177 (1991); M. Kasevich and S. Chu, *ibid.* **67**, 181 (1991).

[3] T. Sleator, T. Pfau, V. Balykin, O. Carnal, and J. Mlynek, Phys. Rev. Lett. **68**, 1996 (1992).

[4] R. Grimm, V. S. Letokhov, Yu. B. Ovchinnikov, and A. I. Sidorov, Pis'ma Zh. Eksp. Teor. Fiz. **54**, 619 (1991) [JETP Lett. **54**, 615 (1991)]; T. Pfau, C. S. Adams, and J. Mlynek, Europhys. Lett. **21**, 439 (1993).

[5] P. J. Martin, B. G. Oldaker, A. H. Miklich, and D. E. Pritchard, Phys. Rev. Lett. **60**, 515 (1988); P. L. Gould, G. A. Ruff, and D. E. Pritchard, *ibid.* **56**, 827 (1986).

[6] J. Mlynek (private communication).

[7] I. V. Hajnal and G. I. Opat, Opt. Commun. **71**, 119 (1989).

[8] R. J. Cook and R. K. Hill, Opt. Commun. **43**, 258 (1982); the atomic mirror was first demonstrated by V. I. Balykin, V. S. Letokhov, Yu. B. Ovchinnikov, and A. I. Sidorov, Phys. Rev. Lett. **60**, 2137 (1988).

[9] J. V. Hajnal, K. G. H. Baldwin, P. T. H. Fisk, H.-A. Bachor, and G. I. Opat, Opt. Commun. **73**, 331 (1989).

[10] R. Deutschmann, W. Ertmer, and H. Wallis, Phys. Rev. A **47**, 2169 (1993).

[11] E. Kyrölä and S. Stenholm, Opt. Commun. **22**, 123 (1977).

[12] N. P. Bigelow and M. G. Prentiss, Phys. Rev. Lett. **65**, 555 (1990); J. J. Tollett, J. Chen, J. G. Story, N. W. M. Ritchie, C. C. Bradley, and R. G. Hulet, Phys. Rev. Lett. **65**, 559 (1990).

Laser Physics, Vol. 4, No. 5, 1994, pp. 983 - 994.

SPECIAL ISSUE
"LASER COOLING AND TRAPPING"

Velocity-Resolved Atomic Beam Reshaping by a Standing-Wave Laser Field

Qiming Li, B. W. Stenlake, I. C. M. Littler, H.-A. Bachor, K. G. H. Baldwin, and D. E. McClelland

Laser Physics Centre, The Australian National University, Canberra, ACT 0200, Australia

Received September 3, 1993

Abstract – The reshaping of the transverse spatial profile of an atomic beam by a perpendicular, near-resonant, standing-wave laser field is investigated for negative frequency detunings using a longitudinal velocity-selective detection system. The experimental dependence of the reshaped profile on the longitudinal and transverse atomic velocities agrees qualitatively with a continued fraction solution for the light force. In particular, a regime is found where channelling of the atoms near the antinodes of the standing wave produces a central peak in the atomic beam profile in the far field. The central peak is predicted when the force generated by the periodic component of the standing-wave potential is calculated using the continued fraction solution but not when approximated by the (zero velocity) gradient force model.

INTRODUCTION

The interaction of a beam of two-level atoms with a standing-wave laser light field has been the subject of extensive investigation in recent times. Standing waves have been used to longitudinally cool [1] and guide [2], transversely collimate [3], channel [4], trap [5], deflect [6], and diffract [7] beams of atoms. Recent attention has been centered on the use of standing waves as a means of guiding atoms for direct-write lithography [8].

The interaction of an atom with a standing-wave field differs fundamentally from the interaction with a traveling wave because of the possibility of photon exchange between the two counterpropagating light fields comprising the standing wave. The importance of such stimulated processes is determined by the atomic saturation parameter $G = 2\Omega^2/\Gamma^2$ for the light field (amplitude E). Here, $\Omega = \mu E/\hbar$ is the Rabi frequency, and μ and Γ^{-1} are the dipole moment and natural lifetime of the atomic transition, respectively.

At very low intensities for which the atomic saturation parameter $G \ll 1$, spontaneous forces dominate. When the laser field is detuned below the atomic resonance, the atom experiences a velocity-dependent viscous damping force responsible for optical molasses, as used for some atom traps [9]. In classical optical molasses, the total force is simply equal to the sum of the radiation pressure (spontaneous) forces for the two traveling waves that comprise the standing wave. Because the magnitude of the spontaneous force is determined by the rate of spontaneous emission events, it is limited by saturation of the atomic transition.

However, at high laser intensities ($G \geq 1$), stimulated processes, which arise from redistribution of photons between the two traveling waves, dominate the light force on the atom [10]. Because the redistribution rate is dependent directly on the Rabi frequency and does not saturate at high field strengths, the stimulated force (unlike the spontaneous force) increases with laser intensity.

It is important to note that the stimulated forces in the standing wave are velocity dependent since the interaction of the atom with the light field is dependent on the Doppler shift with respect to each traveling wave. Indeed, multiple stimulated interactions between the atoms and both traveling waves can give rise to Doppleron resonances [11] when the laser detuning in the rest frame of the atom is equal to an odd multiple of the Doppler shift. Such resonances have been observed in both the longitudinal [12] and transverse [13] motion of atoms in standing waves that were, respectively, parallel and perpendicular to the atomic beam.

When the velocity of the atom in the direction of the standing wave approaches zero, the stimulated force simply reduces to the usual (velocity-independent) dipole or field gradient force. The gradient force is purely conservative and, consequently, has no effect on the magnitude of the atomic momentum (although it can be used to alter the direction of the atoms [8] or even to diffract them [7]).

But for finite velocities, where the Doppler shift plays an important role in the interaction of the moving atom with the standing wave, the force on the atom is no longer conservative and becomes velocity dependent. At relatively low laser intensities ($G \sim 1$), the force averaged over a wavelength can be a damping or a heating force, depending on whether the laser detuning in the atomic rest frame is positive or negative – exactly the opposite of the spontaneous force case. At higher laser intensities ($G \gg 1$), the situation becomes more complicated: the velocity-dependent dipole force can change rapidly in sign and magnitude as Doppleron resonances come into play for particular velocities.

The trajectory of the atom is treated classically, which is valid when the transverse momentum of the atoms is much larger than the single-photon momentum $\hbar k$. The adiabatic approximation is also used, which assumes that the rate of change of velocity is sufficiently small that the atom's internal state adiabatically follows the change in the external field. The force can be separated into components parallel and perpendicular to the standing wave, the perpendicular component being smaller by $1/ka$ due to the difference in the spatial gradients.

The interdependence of the force on the atom's internal state, position, and velocity has the consequence that a general analytical expression for the force on the atom is not possible. However, Minogin and Serimaa [15] have used the techniques of Fourier expansion and continued fractions to derive an approximate expression for the velocity-dependent gradient force for finite velocity. Fourier expanding of the force terms gives

$$F = F_0 + \sum_{n=1} (F_n^C \cos(2nkz) + F_n^S \sin(2nkz)), \quad (3)$$

while the continued fraction method is used to calculate the odd and even Fourier coefficients F_n^C and F_n^S. Here, F_0 is the spatial average of the velocity-dependent force over a standing-wave period.

The F_0 term is particularly important for those atoms whose kinetic energy is much greater than the depth of the periodic potential, thereby allowing them to experience a force averaged over many wavelengths. The sine and cosine components (and their higher harmonics) represent the effect of the periodic nature of the potential. These higher order components ($n \geq 1$) are particularly important for atoms whose kinetic energy is of the same order or less than the potential, as they define the shape of the periodic potential wells in which the atoms may be channelled.

It is possible to obtain a purely analytic solution for the velocity-dependent dipole force in two simplifying regimes without using Fourier decomposition:

(1) The transverse velocity of the atom is identically zero. Here, the force on the atom is simply the usual (velocity-independent) dipole or gradient force, which arises from the periodic potential

$$U(z) = \frac{\hbar\Delta}{2} \ln\left\{1 + \frac{2\Omega^2(z)}{4\Delta^2 + \Gamma^2}\right\} = \frac{\hbar\Delta}{2} \ln\left\{1 + \frac{G_{\text{local}}(z)}{4\Delta^2/\Gamma^2 + 1}\right\}, \quad (4)$$

where Δ is the detuning of the laser frequency from resonance. The usual dipole force varies periodically with the local resonant Rabi frequency $\Omega(z) = 2\Omega_0 \cos(kz)$ due to the presence of the standing-wave light field. Note that the gradient force is purely conservative and averages to zero over one wavelength.

(2) The transverse velocity of the atom is sufficiently small that the transit time over a wavelength is much longer than the atomic relaxation time, i.e.,

$$kv_t \ll \Gamma. \quad (5)$$

In this low transverse velocity regime, the zeroth-order force term reduces to [15]

$$F_0(G, \Delta) = \kappa(G, \Delta) v_t, \quad (6)$$

where $\kappa(G, \Delta)$ is a constant with respect to velocity. The total force under these circumstances can be written as the sum of F_0 and the gradient force (after Dalibard *et al.* [3]), i.e.,

$$F = -\delta U(z)/\delta z + F_0 = -\delta U(z)/\delta z + \kappa(G, \Delta) v_t. \quad (7)$$

Thus, the force is the sum of a purely periodic potential (due to the gradient force) and a damping or heating term depending on the saturation parameter and the laser detuning.

For transverse velocities where $kv_t \ll \Gamma$ does not hold, the force no longer has a simple linear dependence on the transverse velocity due to the increasing importance of Doppleron resonances at high G values. Under these conditions, the full Fourier decomposition and continued fraction technique is required to obtain a numerical solution for the force.

However, for very large transverse velocities for which the atomic kinetic energy is much greater than the depth of the periodic potential, the atom may traverse many standing-wave periods during the course of the interaction. In this situation, the higher order components may be negligible because of the dominance of the spatially averaged F_0 term, and hence the force expression may simplify yet again (although Doppleron effects may still be important for F_0).

Using the continued fraction method, it is difficult to interpret the behavior of the atom in the light field with the same physical insight as is possible using the dressed atom approach. On the other hand, the continued fraction method enables a relatively straightforward numerical calculation of the stimulated light forces and, unlike the dressed atom model, can be applied to higher transverse velocities where Doppleron resonances become important [14]. We have used this method in the present work to calculate the atomic trajectories for a diverging sodium atomic beam traveling perpendicularly to a strong ($G \gg 1$) standing light wave detuned negatively from resonance, for comparison with our experimental measurements of the effect of the standing wave on the far field atomic beam spatial distribution.

NUMERICAL CALCULATIONS

1. Force on the Atom

The first step in determining the interaction of the atomic beam with the standing-wave field was the calculation of the velocity-dependent dipole force [equation (3)] as a function of the variable parameters in the

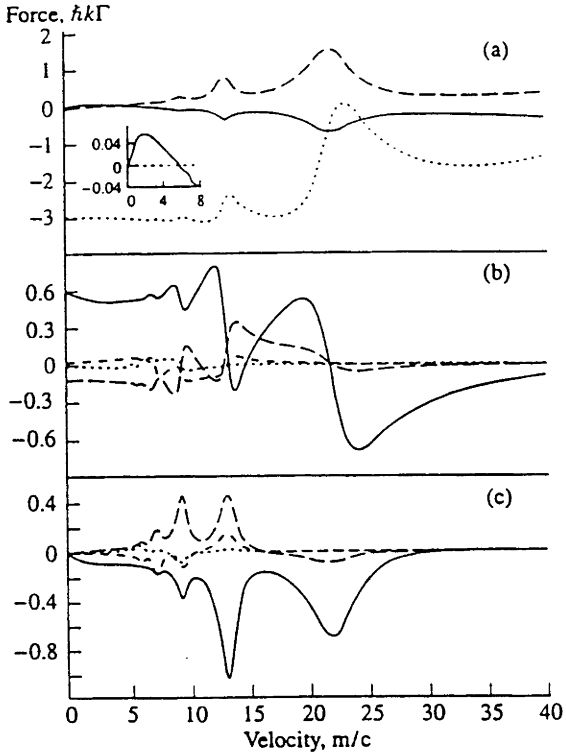

Fig. 1. Fourier coefficients for the velocity-dependent dipole force as a function of transverse velocity for a saturation parameter $G = 70$ and detuning $\Delta/2\pi = -75$ MHz: (a) zeroth-order term F_0 (solid), and first-order coefficients F_1^C (dashed) and F_1^S (dotted). Inset: F_0 with magnified force scale; (b) sine coefficients $n = 2$ (solid), 3 (dashed), 4 (small dashes), and 5 (dotted); (c) cosine coefficients $n = 2$ - 5, as for (b). Note that, in this experiment, $v < 5$ m/s.

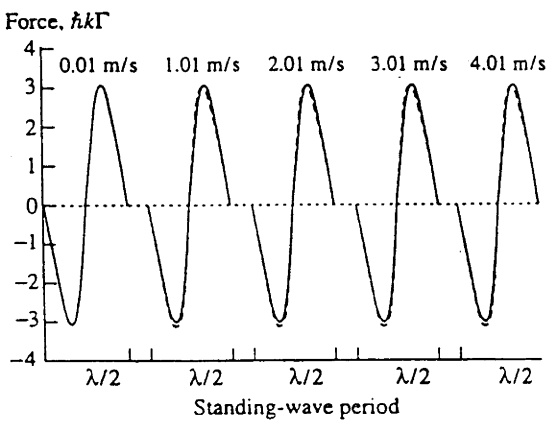

Fig. 2. Comparison of continued fraction solution ($1 \le n \le 20$, solid curve) with gradient force (dotted curve) as a function of z over one standing-wave period for five values of transverse velocity. Conditions as for Fig. 1.

experiment: laser intensity I, detuning Δ (in the rest frame of the atom), and transverse velocity v_t. This required the evaluation of the Fourier coefficients using the continued fraction technique outlined by Minogin and Serimaa [15].

The Fourier coefficients for the zeroth- and first-order ($n = 1$) terms are shown in Fig. 1a as a function of transverse velocity. The intensity is quoted throughout using the peak single traveling wave saturation parameter G (= $[G_{local}(z = 0)]/4$) and in Fig. 1 is chosen to be in the midrange of the intensities present in the standing wave ($G = 70$). The detuning $\Delta/2\pi = -75$ MHz corresponds to the smallest detuning used in the experiments.

The zeroth-order term F_0 represents the spatially averaged force and therefore has no z-dependence, while the first-order ($n = 1$) sine and cosine terms reflect the fundamental periodicity of the standing-wave potential. Figures 1b and 1c show the higher order coefficients ($n = 2$ - 5), which contribute to the specific shape of each periodic potential well: the sine harmonics (Fig. 1b) and the cosine harmonics (Fig. 1c). The obvious undulations in Fig. 1 are the Doppleron resonances [11 - 13], which occur at $\Delta = (2n + 1)\Delta_{Doppler}$ in the low-intensity limit but which, at the intensities used here, are Stark shifted to higher velocities.

As can be seen from Fig. 1a, the F_0 term is positive for low transverse velocities ($v_t < 6$ m/s), i.e., a heating force, but changes sign at higher transverse velocities to become a damping force. Under the present experimental conditions, the peak in the transverse velocity distribution is ~1 m/s, and hence the region of interest is $v_t < \sim 5$ m/s. Thus, in the present experiment, F_0 is primarily responsible for heating.

In Fig. 1, it should be noted that the Doppler shift velocity corresponding to the sodium natural linewidth (10 MHz) is 5.9 m/s (Fig. 1), and hence the inequality $kv_t \ll \Gamma$ holds in the region of interest in the present experiment. As mentioned previously, this is the regime in which the total force may be expected to be approximated by the sum of F_0 and the gradient force, the latter being independent of velocity. Indeed, Fig. indicates that the net contribution of the higher order terms ($n \ge 1$) changes relatively slowly with transverse velocity in this regime. This supports the hypothesis that, for $kv_t \ll \Gamma$, the summation of the higher order forces in equation (4) may be identified with the gradient force in equation (7), i.e.,

$$F - F_0 = \sum_{n=1} (F_n^C \cos 2nkz + F_n^S \sin 2nkz) = -\frac{\delta U(z)}{\delta z}. \quad (8)$$

To illustrate this, the sum of the higher order force terms is compared with the gradient force in Fig. 2 over the regime of our experiments ($kv_t \ll \Gamma$). Shown is the sum of the $n = 1$ - 20 sine and cosine force terms in the Fourier expansion as a function of the spatial position (z) over one standing-wave period for five transverse

velocities. (Note, however, that the transverse velocity is assumed constant, i.e., independent of z, over each period.) Also shown is the gradient force calculated for the same standing-wave period. As can be seen from Fig. 2, the sum of the Fourier components (which determine the potential well shape) closely approximates the result for the gradient force, particularly for the lower transverse velocities. However, we show later that, despite the similarity of these two models for the light force, the effect on the predicted far field spatial atomic beam profile can be significantly different.

To emphasize the importance of the spatially invariant heating term at these detunings, the potential corresponding to the continued fraction solution is shown as a function of z in Fig. 3 with and without the heating component F_0 (assuming a constant 1 m/s transverse velocity). It is clear that the heating contribution becomes significant compared to the spatially varying potential once atoms have traversed a number of wavelengths.

Examination of Fig. 1 indicates that, in the region of interest, the sine force terms dominate the cosine terms, and consequently the spatially varying force component is predominantly a sinusoidal damping force. This is to be expected since under the conditions of the present experiment, the term in equation (4)

$$\frac{G(z)^2}{4\Delta^2/\Gamma^2 + 1} \ll 1 \tag{9}$$

allows expansion of the logarithmic factor for the gradient force

$$U(z) = \frac{\hbar\Delta}{2}\ln\left\{1 + \frac{G_{\text{total}}(z)}{4\Delta^2/\Gamma^2 + 1}\right\} - \frac{\hbar\Delta}{2}\left\{\frac{G_{\text{total}}(z)}{4\Delta^2/\Gamma^2 + 1}\right\} \propto \cos^2 kz. \tag{10}$$

Hence,

$$F_{\text{gradient}}(z) = -\delta U(z)/\delta z \propto \sin 2kz. \tag{11}$$

Similarly, the spatial variation of the force in Fig. 3 is approximately that of a sine wave, resulting in the dominance of the sinusoidal terms.

As the detuning Δ is increased in equation (9), the logarithmic expansion becomes even more sinusoidal. To illustrate this, the force terms F_0, F_1^C, and F_1^S are shown in Fig. 4 as a function of detuning for a fixed transverse velocity of 1.0 m/s. The significant feature here is that the F_1^S term is considerably larger in magnitude than the other force terms. This dominance increases at very large detunings (many GHz), with the zeroth-order and F_1^C terms approaching zero for detunings above 200 MHz. The result is that, at very large detunings (where spontaneous events are negligible), the continued fraction solution to the force becomes purely conservative (i.e., negligible heating) and for small velocities closely approximates the gradient force that exactly follows the sinusoidal periodicity of the standing-wave light field.

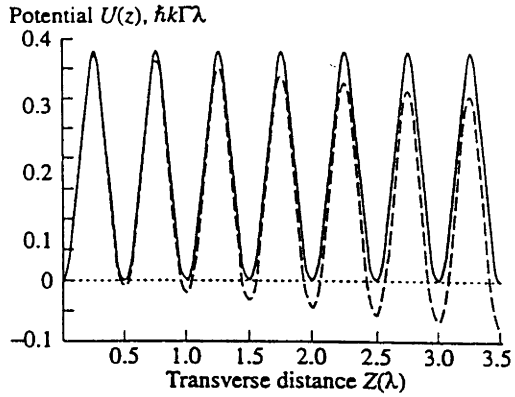

Fig. 3. Continued fraction potential with (dashed curve) and without (solid curve) the heating term F_0, assuming a constant transverse velocity of 1 m/s (same conditions as Fig. 1).

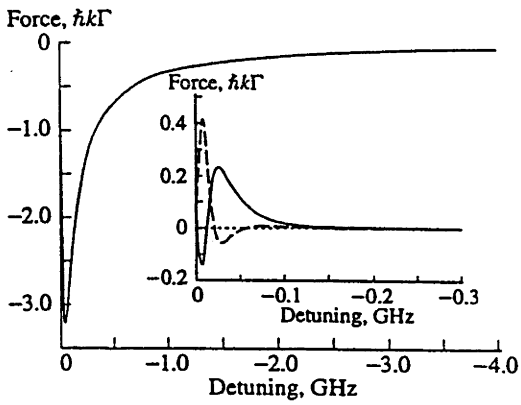

Fig. 4. Variation of first-order sine term F_1^S for large detunings at a fixed intensity (G = 70) and transverse velocity (v_t = 1.0 m/s). Inset: F_0 (solid) and F_1^C (dashed) variation over a smaller range of detunings.

2. *Atomic Trajectories*

The second step in the numerical model was the simulation of the atomic trajectories.

The atomic beam was represented by a one-dimensional ensemble of atoms with identical longitudinal velocity originating from a source with width equal to the oven diameter. This width was in turn divided into a series of sources one-half wavelength in extent to make use of the repetitive structure provided by the standing wave. It was found that 250 source points per $\lambda/2$ were required to give sufficient statistical smoothness

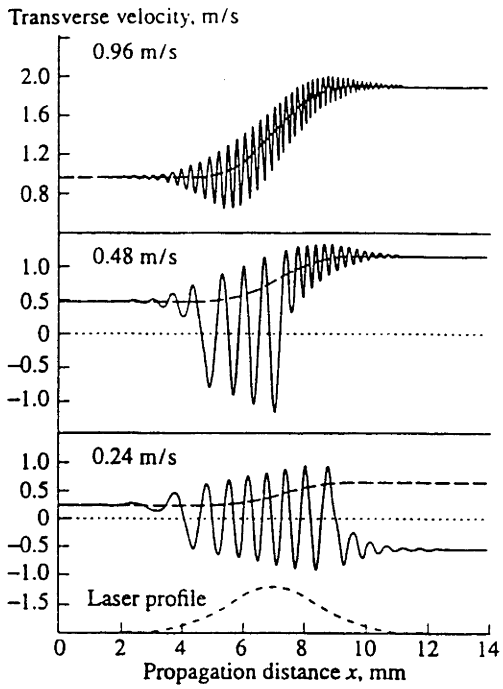

Fig. 5. Instantaneous transverse velocity as a function of propagation distance (x) for three different initial transverse velocities. The longitudinal velocity is 1000 m/s, $\Delta/2\pi = -75$ MHz, and $G = 140$. Solid curves, continued fraction solution; dashed curves, heating term (F_0) only. The dotted curve is the standing-wave intensity profile.

to the results. The results of calculations for the $\lambda/2$ sources could then be summed, allowing for the displacement of each $\lambda/2$ source in the transverse (z) direction. The resulting spatial distribution was then convolved with the 60-μm instrumental resolution of the detection system to allow comparison with the experimental profiles.

A calculation of the atomic trajectory from each source point was performed for a given transverse velocity. The experimental beam divergence was simulated by calculating a range of transverse velocities that were weighted so that the spatial distribution at the detector position exactly matched the experimental spatial profile in the absence of the standing wave.

The trajectory of atoms in a given longitudinal velocity group (v_l) was calculated for each particular initial condition (source point, transverse velocity v_t). In these calculations, it was assumed that the longitudinal velocity was unaffected by changes to the transverse velocity, which, given the disparity between the magnitudes of these two velocities, is a good approximation in the present experiment. Furthermore, it was found that the final longitudinal velocity was altered negligibly by interaction with the weaker (by $1/ka$) longitudinal force components in the standing-wave potential.

The atom was propagated for a small distance $\delta x = 1$ μm through the interaction region, for which the transit time $\delta t = \delta x / v_l \sim 10^{-9}$ s at the most probable longitudinal velocity (1000 m/s). The maximum transverse acceleration possible under all the conditions calculated was $a_t^{\max} < 10^7$ m/s^2, yielding a maximum transverse velocity change $\delta v_t^{\max} < 10^{-2}$ m/s. For such small transverse velocity changes, the force on the atom will not change over the distance δx (Fig. 1), and hence to a good approximation, the final transverse velocity of the atom can be calculated assuming a constant force over that small region. Using the new value for the transverse velocity, the atom is again propagated a distance δx and the procedure repeated until the atom has left the interaction region.

The results of some of these propagation calculations are shown in Fig. 5, where the instantaneous atomic velocity for one source point is plotted as a function of propagation distance (x) for three values of the initial transverse velocity. The influence of the periodic potential is clearly shown by the oscillatory behavior of the atomic velocity. Channelling is indicated when the atomic velocity changes sign. It is clear from this behavior that the final velocity can be in the opposite direction to the initial velocity for those atoms that experience channelling.

The criterion for channelling to occur is that the sum of the instantaneous potential energy and transverse kinetic energy of the atom is less than the local depth of the standing-wave potential. As a result of channelling, the final direction was found to depend sensitively on the initial transverse velocity condition.

For some atoms, the initial transverse velocity is sufficiently large that channelling does not occur at any stage during the interaction with the standing wave. The threshold for this condition is defined here as the escape initial transverse velocity (~0.7 m/s under the conditions shown). For atoms with initial transverse velocity significantly greater than the escape initial transverse velocity, the final transverse velocity invariably converges to the pure heating (spatially averaged) value due to the traversing of many standing-wave periods.

The spatial trajectories executed by atoms with the initial conditions of Fig. 5 are shown in Fig. 6. The oscillatory behavior is clearly the result of channelling in the periodic potential and can result in widely varying final positions, which again depend sensitively on the initial transverse velocity. For large initial transverse velocities (greater than the escape initial transverse velocity), the trajectory closely follows that for the heating term only.

These calculations were carried out for initial transverse velocities (in steps of 5×10^{-4} m/s) over the range 0 - 5 m/s corresponding to the range of transverse velocities in the experiment. For each initial transverse velocity, a unique final transverse velocity was

obtained. Figure 7a shows the results of such a calculation derived from a single source point using the continued fraction solution for a range of initial transverse velocities (in steps of 5×10^{-5} m/s).

Figure 7b shows an averaged plot of the magnitude of the final velocity versus initial velocity for the following force terms: dotted line, heating term F_0 only; dashed line, F_0 + gradient; solid line, continued fraction. The curves represent the average (over all 250 source points in the $\lambda/2$ interval) of the magnitude of the final velocity for each initial transverse velocity.

We examine first the structure evident in these two figures. In Fig. 7a, there is a pattern of modulations that are periodic with the initial velocity. The period of the modulations is found to be proportional to the laser wavelength. Furthermore, the modulations cease for initial transverse velocities greater than the escape initial transverse velocity (~0.7 m/s). It is therefore evident that the modulations are caused by the effect of the periodic potential on the atomic motion.

In Fig. 7b, the modulations are manifested as ripples in the averaged curves for the two potentials that contain a periodic component (F_0 + gradient and continued fraction). The pure heating term produces a smooth increase in the transverse velocity as expected.

We now examine the behavior of the final versus initial velocity curves for various initial velocity regimes. First, for transverse velocities very close to zero (<0.02 m/s), Fig. 7b indicates that both the gradient and continued fraction curves yield larger final transverse velocities than the pure heating term. This is because only atoms with zero transverse velocity that travel through the valleys in the periodic potential remain undeflected. Since most atoms traverse regions of higher potential, they will experience some deflection and hence an increase in velocity. By contrast, the pure F_0 term will not accelerate atoms with zero transverse velocity.

Second, it is apparent from Fig. 7a that, for atoms with an initial transverse velocity <0.1 m/s, the magnitude of the final transverse velocity does not vary appreciably. A similar behavior is found in Fig. 7b for the averaged continued fraction calculation and for a much smaller range of initial velocities for the F_0 + gradient calculation. The result is that atoms that fall within this small initial transverse velocity range form a slowly diverging group that does not experience appreciable heating.

However, Fig. 7a shows that, for initial transverse velocities >0.1 m/s, there is a marked bifurcation of final transverse velocities. This behavior indicates that, following channelling, atoms either continue to move away from the atomic beam axis or have a final velocity directed toward the atomic beam axis. In either case, the atoms are accelerated due to heating. Those atoms that have final velocities that are directed towards the atomic beam axis are in this sense "reflected." (Note that reflection does not occur for atoms with greater

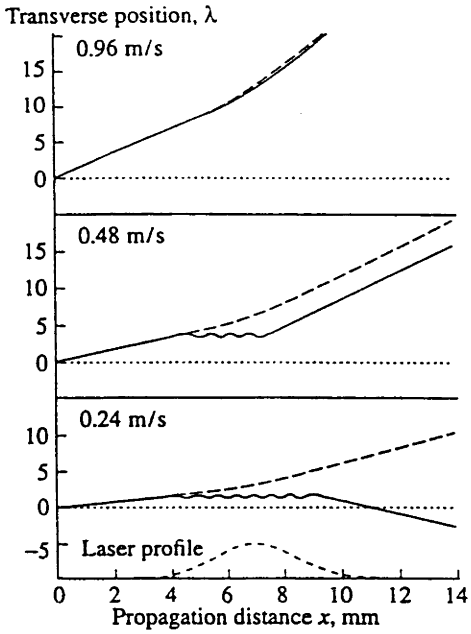

Fig. 6. Spatial trajectory for the cases in Fig. 5. Channelling of the atom between adjacent nodes of the standing wave can be clearly seen for the two lower velocities.

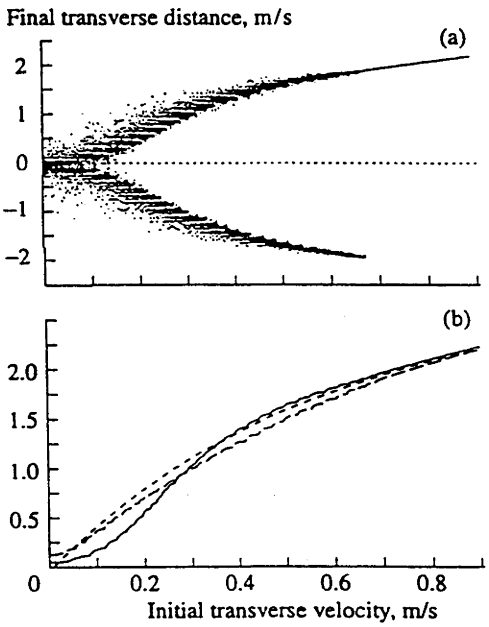

Fig. 7. (a) Plot of the final transverse velocity as a function of initial transverse velocity for a single source point (for $G = 140$, $\Delta/2\pi = -75$ MHz, $v_l = 700$ m/s). (b) Magnitude of the final velocities shown in Fig. 7a averaged over the distribution of 250 source points. Dotted curve, heating (F_0) term only; dashed curve, F_0 + gradient force; solid curve, continued fraction solution.

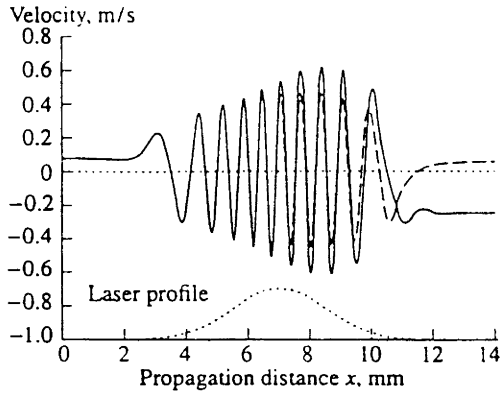

Fig. 8. Instantaneous transverse velocity as a function of propagation distance (x) for initial $v_t = 0.08$ m/s (conditions as for Fig. 5). Solid curve, continued fraction solution; dashed curve, gradient force + F_0. The dotted line is the standing-wave intensity profile.

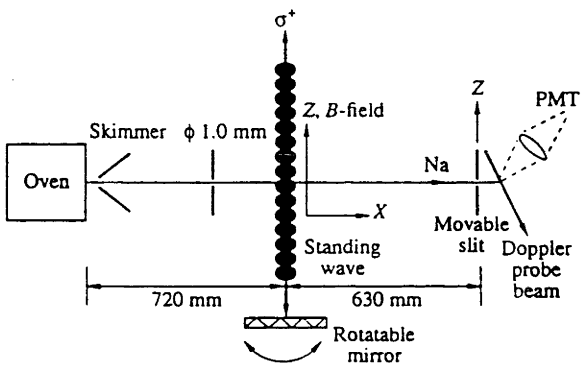

Fig. 9. Experimental arrangement. The atomic beam is apertured to 1.0 mm just before the standing wave. The 60 μm translatable slit defines the LIF detector spatial resolution.

than the escape initial velocity of ~0.7 m/s.) A similar reflection behavior has been reported experimentally by Esslinger *et al.* [16] for large detunings from resonance. These reflections result in the atoms crossing the center of the atomic beam axis at some point further downstream.

Another feature of the calculations shown in Fig. 7b is the noticeable difference between the results for the F_0 + gradient force and the continued fraction solutions. It is clear that the addition of the (periodic) gradient force potential to the heating term F_0 reduces the final transverse velocity from that for the F_0 calculation alone. This reduction is even more marked for the continued fraction calculation, particularly at lower initial transverse velocities.

However, for transverse velocities >0.35 m/s, a slightly higher final transverse velocity results for the continued fraction case than for the pure heating case. At very large transverse velocities, for which the exac nature of the periodic potential is less important, the tw curves converge to the pure heating value. As a resul final transverse velocities greater than 4 m/s were mad equal to the value given by the heating term alone.

Given the similarity of the gradient and continue fraction forces (without F_0) in Fig. 2, the differenc between the two cases in Fig. 7 may seem surprising However, there are two factors that need to be consid ered. First, as the transverse velocity of the aton changes because of channelling in the periodic poten tial, it does not remain on a single continued fractio force curve (e.g., as shown in Fig. 2 for each standing wave period). Instead, the atoms experience a force tha varies continuously from the higher to the lower trans verse velocity force curves. Second, the effects of th very small differences in the two potential models ar cumulative as the atom traverses the standing wave.

These cumulative effects are illustrated in Fig. 8 which shows the instantaneous transverse velocity versu propagation distance for an atom with initial $v_t = 0.08$ m/ (where the difference between the continued fraction an gradient force calculation is most marked in Fig. 7). A can be seen, the subtle differences in these forces resul in a considerable difference in the instantaneous trans verse velocities, with the final transverse velocitie being very different in sign and magnitude.

EXPERIMENTAL

The experimental arrangement is shown in Fig. 9 A sodium atomic beam was produced by a therma oven source operated at a temperature of ~500°C an with a nozzle diameter of 0.4 mm. When operated a this temperature and pumped by a turbo molecula pump, the pressure in the oven chamber was typicall 2×10^{-6} mbar. The oven chamber was connected to th standing-wave interaction chamber by a differentiall pumped region, which was evacuated by a second turb molecular pump. Isolation of the differentially pumpe region was achieved using a ~1-mm-diameter skimme located 10 mm from the oven nozzle. The interactio chamber was maintained at a pressure of $\sim 5 \times 10^{-6}$ mba by a third turbo pump, yielding a mean free path man times the chamber diameter (which was 620 mm). Th atomic beam was apertured to a diameter of ~1.0 mm directly in front of the standing-wave interactio region, thereby defining a maximum half angle beam divergence of ~1 mrad, which corresponds to a mea transverse velocity of ~1 m/s for sodium atoms travel ing with the most common velocity (1000 m/s).

Light from a stabilized ring dye laser (the interactio laser was a Coherent 699-21 operated with R6G) formed the standing wave and intersected the atomic beam in th middle of the interaction chamber 720 mm downstrea from the oven nozzle. The standing wave was formed b retroreflecting the laser from a rotatable mirror locate inside the interaction chamber. The $1/e$ width of the lase

beam intensity profile was approximately 4.2 ± 0.5 mm, and the beam power was $P \sim 100 \pm 10$ mW. This corresponds to a single-beam, on-resonance Rabi frequency of 75 ± 12 MHz and a single-beam saturation parameter of $G = 120 \pm 30$ at the center of the beam.

To enable the atom to be treated as a two-level system, a magnetic field of 10 - 20 G was applied parallel to the interaction laser to separate the Zeeman sublevels. The interaction laser was circularly polarized and tuned to the sodium $3s^2S_{1/2}(m_F = 2)$ and $3p^2P_{3/2}(m_F = 3)$ transitions. Optical prepumping of the atoms was not required as the detection method was state selective, detecting only those atoms that interacted with the standing wave.

The detection region was housed in a separate chamber, which was evacuated by a fourth turbo pump that maintained the pressure below 2×10^{-6} mbar. The velocity-selective detection system consisted of a second, independently tunable laser (the detection laser was a Spectraphysics 380D with R6G), which was tuned to the transition between the $3s^2S_{1/2}(F = 2)$ hyperfine ground state and an excited state. The laser-induced fluorescene (LIF) produced as the atoms decayed into both the $3s^2S_{1/2}(F = 2)$ and $3s^2S_{1/2}(F = 1)$ states yielded a signal proportional to the number of atoms in the $F = 2$ state. Strictly speaking, there are three accessible upper hyperfine levels, but the fluorescence signal was dominated by the $F = 3 \longrightarrow 2$ transition.

The detection laser crossed the atomic beam at 63° to the propagation axis of the atomic beam at a point 640 mm downstream from the standing wave. The LIF was detected by a photomultiplier via a microscope imaging system whose optical axis was perpendicular to the plane formed by the atomic beam and the detection laser. For sufficiently low detection laser powers, the longitudinal velocity resolution was determined by the atomic linewidth (10 MHz), which was much greater than the laser bandwidth (~1 MHz). The combination of intersection angle and detection bandwidth yielded a longitudinal velocity resolution of ±5 m/s.

The detection chamber was separated from the interaction chamber by a movable slit, which determined the spatial resolution of the apparatus. The slit had a width of ~60 μm and was located 630 mm downstream from the standing wave. This defined the angular resolution of the detection system (assuming a point source at the standing wave) to be 90 μrad, corresponding to a transverse velocity resolution of 0.09 m/s ($\sim 3\hbar k$) for a longitudinal beam velocity of 1000 m/s. The slit was mounted on a translation stage with a digital displacement encoder, which allowed the atomic beam profile to be measured with a positional reproducibility <1 μm, which was much smaller than the spatial resolution.

The atomic beam was chopped and the signal from the photomultiplier was recorded using a lock-in amplifier system. The standing wave was aligned perpendicular to the atomic beam axis by ensuring that the center of the collimated velocity distribution using blue detuning coincided with the center of the atomic beam profile without the standing-wave laser. The stability of the standing-wave pattern was monitored by a Michelson interferometer to ensure that there was no movement of the standing-wave pattern during the time required for an atom at the peak of the longitudinal velocity distribution to traverse the interaction region (~4 ms for 1000 m/s).

RESULTS AND DISCUSSION

Figure 10 shows the experimental atomic beam transverse spatial distributions for three different longitudinal velocity groups in the presence of a standing wave with a fixed detuning. Also shown is the experimental far field spatial distribution for the initial atomic beam in the absence of the standing wave, which was approximately the same for all longitudinal velocity groups. Except where stated otherwise, all spatial profiles (both experimental and theoretical) are normalized by area to allow direct comparison of the shape of the final distributions, obviating the need to correct for changes in the beam density as a function of longitudinal velocity.

The main feature of the experimental profiles is the peak in the center of the spatial distribution. This is due to the effect of the standing wave on the low initial transverse velocity atoms (<0.1 m/s), which reduces the heating of these atoms, as mentioned earlier. An additional concentration of higher transverse velocity atoms near the atomic beam axis arises due to the reflection processes noted previously. The net result is the peak in the spatial distribution, which is centered about the atomic beam axis in the middle of a distribution of heated atoms. These central peaks are much more pronounced in the longitudinal velocity-resolved profiles

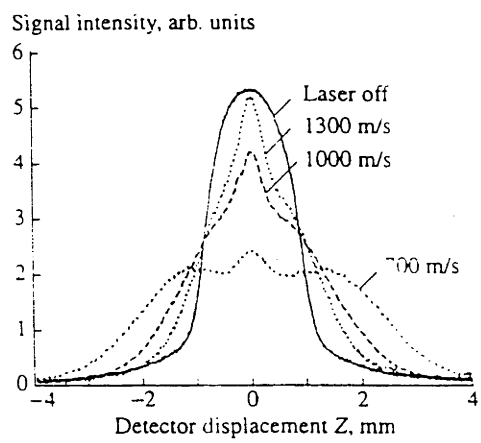

Fig. 10. Variation of the experimental transverse atomic beam spatial distribution with longitudinal velocity for $\Delta/2\pi = -75$ MHz and $P = 100$ mW. Also shown is the atomic beam distribution with the laser off. All spatial profiles are normalized by area.

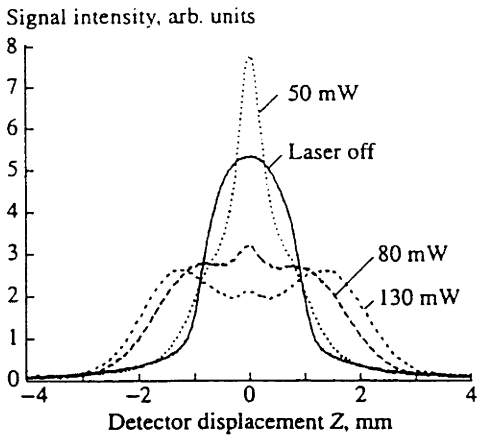

Fig. 11. Variation of the experimental transverse spatial distribution with interaction laser power for one longitudinal velocity (1000 m/s). Conditions as for Fig. 10.

presented here than were the peaks observed in the longitudinal velocity-integrated profiles of Aspect *et al.* and Tanner *et al.* [3].

The central peak lies between two broad, symmetric peaks produced by higher initial transverse velocity

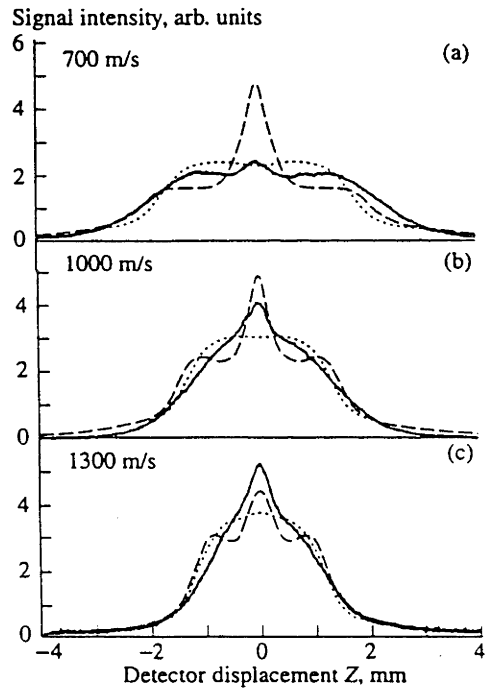

Fig. 12. Comparison of the experimental spatial profiles (solid lines) for the three velocity groups and conditions in Fig. 10, with the continued fraction model (dashed lines) and the F_0 + gradient force model (dotted lines). The value of G used in the calculations was 140 (c.f. 120 ± 30 in the experiment) to give the best fit to the experimental profiles.

atoms. These atoms either traverse a number of wave lengths and are heated by the spatially averaged zeroth order force or are channelled and emerge directed awa from the atomic beam axis. Figure 10 indicates that th heating of the atomic beam increases as the longitudi nal velocity decreases. This behavior is consistent, wit the integrated heating effect being greatest for the lon gitudinal velocity group that experiences the longes interaction time in the standing wave.

In Fig. 11, the spatial distribution for one longitudi nal velocity (1000 m/s) and three different intensities i shown for the same conditions as Fig. 10. The variatio of the atomic beam profile with the interaction lase intensity is very similar to the variation with longitudi nal velocity. To a first approximation, at the transvers velocities employed in these experiments, the relativ magnitudes of the Fourier components are similar ove this variation in intensity, while the total forc increases uniformly with intensity. Thus, a simila degree of heating of the atomic beam results either b altering the interaction strength (intensity) or the inter action time (longitudinal beam velocity).

It should be noted that the transverse crossover veloc ity from heating to cooling for the zeroth-order force F in Fig. 1a (at which point atoms accumulate given a suf ficiently long interaction time [14, 17]) is ~6 m/s The maximum transverse velocity for which there wa a measurable change in signal due to heating in th experiment was ~5 m/s, and hence the great majority o atoms were not accelerated to the crossover velocity This indicates that the interaction times in this experi ment were too short for the accelerated atoms to hav reached an equilibrium transverse velocity distributior consistent with the strong dependence of the spati beam profiles on the interaction time and intensity.

The experimental results are compared in detail i Fig. 12 with the theoretical models, with separate cal culations being presented for each of the velocit groups shown in Fig. 10. Both the continued fractio model and the F_0 + gradient force model are used t simulate the spatial profiles. These calculations use th final versus initial velocity tables (e.g., Fig. 7a) for th determination of the spatial distributions.

In these calculations, the value of G used is that whic best fits the qualitative appearance of the experiment spatial profiles (full width and shoulder height). Under th circumstances, the experimental (G = 120 ± 30) an model (G = 140) values are not significantly differen Note that, at the intensities used, the Rabi frequency i large compared to the hyperfine level separations.

It is clear from Fig. 12 that the F_0 + gradient forc model is able to reproduce the effects of heating but nc the central peak caused by channelling (except for a sma effect at 1300 m/s). On the other hand, the continued frac tion calculations predict both the heating and the form tion of a central peak. Although the central peak in th experimental curves is not as large as the continued frac tion simulation suggests, it is clear that the F_0 + gradie

force model alone is insufficient to explain the form of the observed results. The different results from the two models may be expected from the velocity calculations presented in Fig. 7, which indicates the significantly lower average final velocities for small initial velocities predicted by the continued fraction model.

However, it is clear that the size of the central peak in the experiments is not as great as would be expected from the continued fraction model. This discrepancy is particularly evident for the low-velocity case in Fig. 12a, while the continued fraction model simulates the experimentally observed peak much better at higher velocities. This effect cannot be explained by smoothing of the spatial distribution by the finite spatial resolution, source size, or velocity resolution, which yield an instrumental resolution that is negligible on the transverse distance scale shown on the experimental spatial profiles. Neither can it be explained by rapid motion of the standing-wave position, whose vibration frequency was monitored using the Michelson interferometer and a spectrum analyzer.

On the other hand, the effects of diffusion [10, 14, 18] have been omitted in these simulations due to limitations in computation time. Diffusion is important for atoms with small transverse velocities [14] that would normally be channelled. Furthermore, the spread in velocity space due to diffusion will be accelerated by the heating process. Diffusion would also be expected to play a more important role over longer interaction times [14], which is consistent with the greater discrepancy between the experimental and continued fraction results at lower longitudinal velocities. Hence, the diminished magnitude of the central peak in the experiments compared to the continued fraction model is most likely the result of stimulated diffusion processes.

Diffusion would be expected to play a less significant role at larger detunings [10, 14]. In addition, transverse heating would also be expected to be negligible as illustrated by Fig. 4, where the spatially averaged heating term F_0 is extremely small compared to the first-order term F_1^S. To investigate this, a series of spatial profiles for large detunings ranging from -0.5 GHz to -5.5 GHz in steps of -1.0 GHz is shown in Fig. 13 for a fixed longitudinal velocity (1000 m/s) and intensity ($I = 100$ mW). Note that the experimental profiles in Fig. 13 have not been normalized by area, having been measured during one experimental run under the same conditions.

Central peaks in the spatial distribution were again observed but were much more pronounced than the peaks shown for smaller detunings in Figs. 10 and 11. In particular, for a detuning of -0.5 GHz, the central peak is nearly twice the size of the peak of the distribution at -5.5 GHz (which at such a large detuning approximates the spatial distribution with the laser off).

A model calculation using the continued fraction solution yields the theoretical curve shown in Fig. 13 and produces close agreement with the experimental data. At these large detunings, the continued fraction

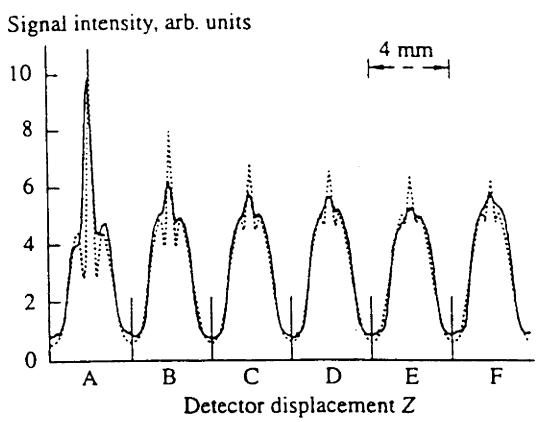

Fig. 13. Experimental transverse spatial profiles (solid lines) for detunings from $A = -0.5$ GHz to $F = -5.5$ GHz in -1.0 GHz increments, compared with the continued fraction model (dashed line: the same simulated result was produced using the gradient force model). Here, $v_l = 1000$ m/s, $P = 100$ mW, and $G = 140$ in the model calculations. Note that the model profiles have all been scaled vertically by the same amount to yield the best fit with the experimental profiles.

model is dominated by the first-order sine term, with negligible contribution from the heating term F_0 (since the spontaneous emission rate would be expected to be extremely low, and consequently Sisyphus heating would be expected to be negligible). Consequently, a calculation using the gradient force alone (without F_0) yields an identical result to the continued fraction model since, at these large detunings and small transverse velocities, both models can be approximated by a purely sinusoidal potential.

Finally, the improved agreement between the experimental and simulated profiles at the large detunings in Fig. 13 (when compared with the small detuning used in Fig. 12) suggests that the discrepancy at small detunings is the result of diffusion. The lower spontaneous emission rate at large detunings reduces the effect of spontaneous diffusion, which, in any case, is negligible (due to saturation) when compared to fluctuation of the dipole forces at large G. The stimulated diffusion coefficient for $\Delta \gg \Omega$ is proportional to Δ^{-6} [10] and consequently diminishes in importance at the large detunings used in Fig. 13, yielding much better agreement between the simulations and experiment. It is this systematic qualitative improvement in the agreement between the simulations and experiment under conditions where diffusion would be expected to be less important (both for small and large detunings) that suggests any discrepancy is due to diffusion processes.

CONCLUSION

An experiment has been performed to study the effect of a strong, near-resonant, standing-wave laser light field on the transverse velocity distribution of a sodium atomic beam. The laser field was detuned

negatively with respect to the atomic transition in order to distinguish the effects of light forces that lead to transverse heating and channelling of the atoms. In order to separate the contributions of the longitudinal and transverse velocity contributions to the far field spatial beam profile, a velocity-sensitive detection system was used to select particular longitudinal velocity groups with high resolution.

The velocity-dependent dipole force was modeled by a continued fraction solution to the Fourier expansion of the light force [15]. In the low transverse velocity regime $kv_t \ll \Gamma$ in which the experiments were conducted, the velocity-dependent dipole force is often approximated by an analytical solution equal to the sum of a (zero velocity) gradient force term and a force term proportional to the atomic velocity.

It has been shown that the F_0 term of the Fourier expansion (representing the spatially averaged velocity-dependent force) could be identified with the latter term, which in the present experiment was responsible for heating of the atomic beam. The gradient force can be identified with the sum of the higher order Fourier terms ($n \geq 1$) in the continued fraction model that yield the shape of the periodically varying potential. In the present experiment, it was this higher order potential that was found to be responsible for the channelling of atoms whose total instantaneous energy was less than the local potential well depth in the standing wave.

However, it was shown that, at low detunings, the experimental spatial distributions caused by the interaction of the atomic beam with the standing wave could best be explained using the full continued fraction model. Although both models reproduced the heating of the beam for atoms with higher transverse velocities, the observed central peak of atoms with lower transverse velocities is not reproduced by the (zero velocity) gradient force model. The central peak was shown to arise from subtle differences in the potential produced by the continued fraction model, which yielded a strong cumulative channelling effect when integrated over the trajectory of the atom through the standing wave. The systematic improvement in agreement between the continued fraction model and the experimental spatial profiles under conditions where the effects of diffusion would be expected to be less important suggests that diffusion was responsible for the differences between simulation and experiment that were more noticeable at small detunings.

For higher velocities ($kv_t \gg \Gamma$), the force on the atom no longer has a simple velocity dependence, and Doppleron resonances [11 - 13] become important. Investigations of the interaction between atoms with high transverse velocities and a strong, near-resonant, standing-wave light field will be the subject of future work.

ACKNOWLEDGMENTS

The skilled technical assistance of B. Brown is gratefully acknowledged. This work was undertaken using equipment funded by the Australian Resea Council. We are grateful for many helpful discussi with Dr. Peter Fisk, CSIRO Division of Applied Physi

REFERENCES

1. Prentiss, M. and Cable, A., 1989, *Phys. Rev. Lett.*, 1354; Gottesman, D., Mervis, J., Prentiss, M., *et* 1992, *Phys. Rev. A*, **46**, 356.
2. Prentiss, M., Cable, A., and Bigelow, N.P., 1989, *J. C Soc. Am. B*, **6**, 2155.
3. Aspect, A., Dalibard, J., Heidmann, A., *et al.*, 19 *Phys. Rev. Lett.*, **57**, 1688; Dalibard, J., Heidmann, Salomon, C., *et al.*, 1987, *Fundamentals of Quant Optics II*, Ehlotzky, F., Ed. (Berlin: Springer), p. 1 Tanner, C.E., Masterson, B.P., and Wieman, C.E., 19 *Opt. Lett.*, **13**, 357; Jian Chen, Story, J.G., Tollett, J.J., *et* 1992, *Phys. Rev. Lett.*, **69**, 1344.
4. Prentiss, M.G. and Ezekiel, S., 1986, *Phys. Rev. Lett.*, 46; Salomon, C., Dalibard, J., Aspect, A., *et al.*, 19 *Phys. Rev. Lett.*, **59**, 1659; Balykin, V.I., Letokhov, V. Ovchinnikov, Yu.B., *et al.*, 1988, *Opt. Lett.*, **13**, 9 Balykin, V.I., Lozovik, Yu.E., Ovchinnikov, Yu.B., *et* 1989, *J. Opt. Soc. Am. B*, 6, 2178; Ovchinnikov, Yu. and Letokhov, V.S., 1992, *Comments At. Mol. Phys.*, 185.
5. Westbrook, C.I., Watts, R.N., Tanner, C.E., *et al.*, 19 *Phys. Rev. Lett.*, **65**, 33; Verkerk, P., Lounis, I Salomon, C., *et al.*, 1992, *Phys. Rev. Lett.*, **68**, 3861; Je sen, P.S., Gerz, C., Lett, P.D., *et al.*, 1992, *Phys. R Lett.*, **69**, 49.
6. Hemmer, P.R., Shahriar, M.S., Prentiss, M.G., *et a* 1992, *Phys. Rev. Lett.*, **68**, 3148.
7. Gould, P.L., Ruff, G.A., and Pritchard, D.E., 198 *Phys. Rev. Lett.*, **56**, 827; Martin, P.J., Oldaker, B.C Miklich, A.H., *et al.*, 1988, *Phys. Rev. Lett.*, **60**, 515.
8. Timp, G., Behringer, R.E., Tennant, D.M., *et al.*, 199 *Phys. Rev. Lett.*, **69**, 1636; Berggren, K.K., Prentiss, M Timp, G.L., *et al.*, submitted for publication in *J. Op Soc. Am. B*.
9. Lett, P.D., Phillips, W.D., Rolston, S.R., *et al.*, 198 *J. Opt. Soc. Am. B*, **6**, 2084, and references therein.
10. Dalibard, J. and Cohen-Tannoudji, C., 1985, *J. Opt. So Am. B*, **2**, 1707.
11. Kyrola, E. and Stenholm, S., 1977, *Opt. Commun.*, 2 123.
12. Bigelow, N.P. and Prentiss, M.G., 1990, *Phys. Rev. Lett* **65**, 555.
13. Tollett, J.J., Chen, J., Ritchie, N.W.M., *et al.*, 1990, *Phys Rev. Lett.*, **65**, 559.
14. Tollett, J.J., Story, J.G., and Hulet, R.G., 1993, *Phys Rev. A*, **47**, 2128.
15. Minogin, V.G. and Serimaa, O.T., 1979, *Opt. Commun.* **30**, 373.
16. Esslinger, T., Hemmerich, A., and Hänsch, T.W., 1992 *Opt. Commun.*, **93**, 49.
17. Kazantsev, A.P., Smirnov, V.S., Surdutovich, G.I., *et al.* 1985, *J. Opt. Soc. Am. B*, **2**, 1731.
18. Gordon, J.P. and Ashkin, A., 1980, *Phys. Rev. Lett.*, **21** 1606.

Appendix B

Derivation of the Expected Number of Spontaneous Emissions in the Reflection Process

This appendix contains a derivation of equation 2.27. The calculation assumes an adiabatic following of the field of the atomic population in a classical trajectory.

The rate of spontaneous emission is equal to the spontaneous emission rate, γ, multiplied by the excited state fraction, P_e. The number of spontaneous emissions, N, is given by this rate multiplied by the time, τ, in the field.

$$N = \gamma P_e \tau \qquad \text{(B.1)}$$

Now, the maximum potential, U_{max}, reached in the light field is equal to the excited state fraction times the detuning energy, $\hbar\Delta$ (Savage, 1996). For reflection, the kinetic energy of the atom in the y direction, $0.5\ m\ v_y^2$, is also equal to the maximum potential of the light field reached, i.e.

$$U_{max} = 0.5\ m\ v_y^2$$

$$= P_e \hbar \Delta \qquad \text{(B.2)}$$

Rearranging B.2 gives:

$$P_e = m\ v_y^2 / (2\ \hbar\ \Delta) \qquad \text{(B.3)}$$

The transit time in the evanescent field is given by (approximately) twice the decay length divided by the initial perpendicular atomic velocity.

$$\tau = 2/qv_y \qquad \text{(B.4)}$$

where 1/q is the evanescent decay length. Substituting B.3 and B.4 into B.1 gives

$$N = \gamma m v_y / \Delta\hbar q \qquad \text{giving (2.27)}$$